

©2015

NILAN UDAYANGA GALABADA KANKANAMGE

ALL RIGHTS RESERVED

DIGITAL 2-D/3-D BEAM FILTERS FOR ADAPTIVE APPLEBAUM RECEIVE  
AND TRANSMIT ARRAYS

A Thesis

Presented to

The Graduate Faculty of The University of Akron

In Partial Fulfillment

of the Requirements for the Degree

Master of Science

Nilan Udayanga Galabada Kankanamge

December, 2015

DIGITAL 2-D/3-D BEAM FILTERS FOR ADAPTIVE APPLEBAUM RECEIVE  
AND TRANSMIT ARRAYS

Nilan Udayanga Galabada Kankanamge

Thesis

Approved:

Accepted:

---

Advisor  
Dr. Arjuna Madanayake

---

Dean of the College  
Dr. Mario Ricardo Garzia

---

Faculty Reader  
Dr. Kye-Shin Lee

---

Dean of the Graduate School  
Dr. Chand K Midha

---

Faculty Reader  
Dr. Igor Tsukerman

---

Date

---

Department Chair  
Dr. Joan Carletta

## ABSTRACT

Linear and rectangular aperture arrays combined with multidimensional (MD) signal processing techniques enable directional enhancement of plane waves by creating highly directional radio frequency (RF) beams. Applications of such space-time filtering (beamforming) techniques can be found in areas such as radar, mobile communication, cognitive radio and radio astronomy. Main challenges in existing beamforming systems include high computational and hardware complexity, low operational bandwidth, and limited spatial selectivity. In this thesis, we employ the network resonant infinite impulse response (IIR) digital beam filter towards the performance enhancement of the existing beamforming systems and its related applications in terms of hardware complexity, spatial selectivity and operational bandwidth. Inherent properties of IIR beam filters, such as *low complexity, higher operational bandwidth, multiple input multiple output (MIMO) nature, recursive structure and electronically steerability* lead to improve directivity properties of the conventional beamformers and enable less complex directional enhancement for wideband applications. Low complexity directional spectrum sensing and feature extraction approach is proposed by combining network resonant beam filters with cyclostationary feature detectors. Spatial selectivity of the conventional beamformer is significantly enhanced by employing

a MD MIMO beam filter as a pre-filter to the existing system. Furthermore, an electronically steerable transmit-beamformer based on space-time network resonant IIR discrete systems is proposed for wideband directed energy applications.

## ACKNOWLEDGMENTS

Firstly, I would like to extend my heartfelt gratitude to my adviser, Dr. Arjuna Madanayake, for his continuous guidance and advice throughout my masters program. His support and patience empowered me to face hardships throughout this journey which would not have been possible if not for him. Also, I would like to thank the rest of my thesis committee: Dr. S.T. Hariharan and Dr. Igor Tsukerman for their reinforcement and constructive comments. I am forever grateful to my parents Sumanawathie and Amarapala and my brothers Nuwan Janaranga and Asiri Sandaruwan and all my relatives for their endless affection. I dedicate this thesis to them for all they have done for me.

I would like to thank Dr. Chamith Wijenayake (former member of ASPC group and student of The University of Akron) of University New South Wales for his contributions related to my research work. I would also like to thank my colleagues at the University of Akron and fellow members of the ASPC group, especially Nilanka, Sewwandi, Arindam, Tharindu, Sunera, Prasad, Viduneth, Vishwa, Suranga, Gihan and Sravan for all their support. It was a complete pleasure working with you. My sincere appreciation goes out to all the faculty members at University of Akron and University of Moratuwa for uplifting my knowledge and skills via graduate and

undergraduate courses and other workshops. I would be failing in my duties if I don't mention all my teachers at Matugama C.W.W. Kannangara College, Udawela Sri Priyarathana College and Debarawewa President College for the solid foundation laid at school level. Last but not least, I sincerely acknowledge the financial support from the National Science Foundation (NSF) and Office of Naval Research (ONR) that funded my masters studies via research assistantships. Thank you for all your effort to make my research a success.

## TABLE OF CONTENTS

	Page
LIST OF TABLES . . . . .	x
LIST OF FIGURES . . . . .	xi
CHAPTER	
I. INTRODUCTION TO HIGHLY DIRECTIONAL TRANSMISSION AND RECEPTION . . . . .	1
1.1 Contributions in this Thesis . . . . .	4
1.2 Publications . . . . .	6
1.3 Thesis Outline . . . . .	8
II. LINEAR/RECTANGULAR APERTURE BASED MULTIDIMEN- SIONAL SIGNAL PROCESSING . . . . .	12
2.1 2-D Discrete ST Plane Wave Signals and Their Spectra . . . . .	15
2.2 Conventional 2-D ST Filtering Techniques - Receive Beamformers . . . . .	18
2.3 Network-Resonant-Based 2-D IIR Beam Filters for Wideband ST Filtering . . . . .	23
2.4 Practical Bounded-Input-Bounded-Output (p-BIBO) Stability of 2-D IIR Beam Filters . . . . .	25
2.5 MD Signal Processing With Rectangular Apertures . . . . .	27
III. DIRECTIONAL SPECTRUM SENSING AND CYCLOSTATION- ARY FEATURE EXTRACTION USING 2D IIR BEAM FILTERS . . . . .	34

3.1 Overview of Proposed Spectrum Sensing and Feature Extraction Architecture . . . . .	37
3.2 Simulated Directional Feature Extraction . . . . .	49
3.3 Conclusions . . . . .	54
IV. DIRECTION/LOCATION ESTIMATION AND MODULATION DETECTION FOR RF SOURCES USING STEERABLE 3-D IIR DIGITAL BEAM FILTERS . . . . .	55
4.1 Overview of the Proposed Architecture . . . . .	56
4.2 Simulated Localization and Directional Sensing Algorithm . . . . .	67
4.3 Conclusions and Future Directions . . . . .	69
V. NETWORK-RESONANT PHASED-ARRAY (NRPA)-ENHANCED APPLEBAUM ADAPTIVE BEAMFORMER . . . . .	70
5.1 NRPA Beamforming Model . . . . .	74
5.2 NRPA-Enhanced Applebaum Adaptive Beamformer System Architecture . . . . .	81
5.3 Enhanced Selectivity and SINR Improvement . . . . .	94
5.4 Conclusions . . . . .	99
VI. NETWORK-RESONANCE APPLEBAUM ADAPTIVE ARRAYS FOR DIRECTIONAL SPECTRUM SENSING . . . . .	101
6.1 Signal Processing Model . . . . .	103
6.2 Proposed Directional Cyclostationary Feature Detector . . . . .	107
6.3 Spectrum Sensing Simulations and Results . . . . .	112
6.4 Conclusions . . . . .	115
VII. BEAM-ENHANCEMENT OF RECTANGULAR APERTURE DIGITAL STAP BEAMFORMERS USING PARTIALLY-SEPARABLE 3-D IIR BEAM FILTERS . . . . .	116

7.1	System Overview . . . . .	117
7.2	Proposed Beam-Enhancement Architecture - Block B . . . . .	126
7.3	Simulated Directivity Improvement Results . . . . .	136
7.4	Conclusion . . . . .	138
VIII.	ELECTRONICALLY STEERABLE DIRECTED ENERGY USING SPACE-TIME NETWORK RESONANT DIGITAL SYSTEMS . . . . .	139
8.1	Proposed Transmit Beamformer Model . . . . .	140
8.2	Simulation Example . . . . .	146
8.3	Conclusion . . . . .	146
IX.	ADDITIONAL RESEARCH: TUNABLE MULTIBAND RF CMOS ACTIVE FILTER ARRAYS . . . . .	147
9.1	Tunable Analog RF Bandpass Filter Synthesis . . . . .	150
9.2	Closed-Form Filter Response . . . . .	154
9.3	Response with CMOS All-Pass Simulation . . . . .	156
9.4	Conclusions . . . . .	159
X.	CONCLUSION AND FUTURE WORK . . . . .	160
10.1	Conclusion . . . . .	160
10.2	Future Work . . . . .	164
	BIBLIOGRAPHY . . . . .	166

## LIST OF TABLES

Table		Page
3.1	Source direction estimation . . . . .	51
5.1	Selection of appropriate simulation model for each region of beam direction with the corresponding control bit selection. . . . .	96
6.1	Hardware resource consumption using Xilinx Virtex-6 XC6VSX475T 1FF1156 device. . . . .	109

## LIST OF FIGURES

Figure	Page
1.1	Application of highly directional, electronically steerable transmit- and receive-mode beamformers. . . . . 2
2.1	Plane wave propagating from a faraway source $S$ . . . . . 13
2.2	Overview of the multidimensional signal processing, (a) one-dimensional, (b) two-dimensional, (c) three-dimensional systems. . . . . 14
2.3	Multidimensional signal processing for transmit beamforming (a) single antenna with no signal processing (b) antenna array with no signal processing (c) antenna array with 2-D signal processing. . . . . 15
2.4	Plane wave representation in (a) $x - y$ and (b) $x - ct$ domains. . . . . 16
2.5	(a) ROS of the signals from DOA $\psi$ . 2-D $(\omega_x, \omega_{ct})$ frequency spectrum of the (b) narrowband signals and (c) wideband signals from three different angles, $60^\circ$ , $40^\circ$ , and $10^\circ$ . . . . . 18
2.6	System overview of the (a) true-time-delay-sum beamformer, (b) phased array, and (c) 2-D Frequency response of the narrowband beamformer. . . . . 20
2.7	System overview of the (a) filter and sum architecture, (b) FFT-based wideband beamformer, and (c) 2-D frequency response of wideband beamformers. . . . . 21
2.8	(a) 2-D first order Ramamoorthy-Bruton network (RBN). Frequency response of (b) $H(s_{ct}, s_x)$ and (c) $T(z_x, z_{ct})$ for $R = 0.01$ and $\psi = 30^\circ$ . . . . . 23
2.9	(a) A plane wave signal in $(x, y, z)$ with the DOA $(\psi, \phi)$ . (b) The line-shaped spectral ROS of the plane wave signal. (c) 3-D frequency spectrum for incoming signals from $(30^\circ, 90^\circ)$ , $(50^\circ, 180^\circ)$ , and $(20^\circ, 270^\circ)$ . . . . . 28
2.10	System architecture of the FFT-based wideband STAP . . . . . 30

2.11	(a) Frequency response of the frequency planar filter. (b) Cascading two frequency planar filters. (c) Line-shaped passband in the $(\omega_x, \omega_y, \omega_{ct})$ domain. . . . .	32
2.12	(a) Frequency response of the discrete domain frequency planar filter (b) Cascading two digital frequency planar filters (c) Obtained line/beam shaped passband in the $(\omega_x, \omega_y, \omega_{ct})$ domain. . . . .	33
3.1	Directional spectrum sensing methods. . . . .	36
3.2	Overview of the proposed 2-D IIR digital beam filter based directional feature extraction system employing a ULA of Archimedean spiral antennas. . . . .	38
3.3	(a) Structure, (b) scattering parameter $S_{11}$ and (c) far-field radiation pattern of the proposed Archimedean spiral antenna. Full-wave simulations are from Ansoft HFSS computational electromagnetic software. . . . .	39
3.4	(a)Signal flow graph of the 2-D IIR beamfilter. . . . .	40
3.5	Array factor of the beam filter for beam direction $\psi = 30^\circ$ (a) cartesian domain (b) polar domain. . . . .	42
3.6	(a)2-D Frequency spectrum of the input signal consisting with three signals from DOAs $10^\circ, 30^\circ$ and $60^\circ$ .(b) Frequency response of the beam filter which is tuned to filter signals from DOA $30^\circ$ . (c) Frequency spectrum at the output of the beam filter. . . . .	43
3.7	(a)Time domain representation of the three signals from DOAs $10^\circ, 30^\circ$ and $60^\circ$ .(b) Output at the beam filter which enhance the signal from $30^\circ$ . . . . .	45
3.8	Spectral correlation function for (a) BPSK modulated and (b) QPSK modulated signals for zero noise environment. . . . .	47
3.9	$\alpha = 0$ line of the SCF function which is equalent to the PSD of the input signal. . . . .	48
3.10	(a) Source distribution, (b) spatial energy distribution $E(\psi)$ and (c)-(h) various feature detection outputs corresponding to the simulation scenario 1. . . . .	50
3.11	(a) Source distribution, (b) spatial energy distribution $E(\psi)$ and (c)-(f) SCF at $\alpha = 0$ corresponding to simulation scenario 2. . . . .	52

3.12	(a) Source distribution, (b) spatial energy distribution $E(\psi)$ and (c)-(f) SCF for different DOAs corresponding to simulation scenario 3. . . . .	53
4.1	(a) Overview of the proposed 3-D IIR beam filter based feature detection scheme with multiple DMS stations. (b) Overview of a DME station which is realized using a planar antenna array and 3-D IIR digital filter. . . . .	56
4.2	Signal Flow graph of the frequency planar filter correspond to $\mathbf{z}$ domain transfer function $H_m(z_x, z_y, z_{ct})$ . . . . .	58
4.3	(a) Beam shaped passband, (b) array factor, of the 3-D filter for beam direction $\psi = 30^\circ$ and $\phi = 290^\circ$ . . . . .	60
4.4	3-D frequency spectrum of the input signal, (b) frequency response of the filter, (c) output frequency spectrum. . . . .	62
4.5	(a) Time domain representation of the three signals from DOAs $(30^\circ, 50^\circ)$ , $(40^\circ, 120^\circ)$ , and $(10^\circ, 270^\circ)$ . (b) Output at the beam filter which enhance the signal from $30^\circ$ . . . . .	63
4.6	(a) Source distribution (b) SCF at $\alpha = 0$ . (d-g) Spatial power distribution $E(\theta, \phi)$ corresponding for the simulation 1 . . . . .	66
4.7	(a) Source distribution (b) Spectral correlation function (d-g) Spatial energy distribution $E(\theta, \phi)$ corresponding for the simulation 2 . . . . .	68
5.1	System architectures for (a) conventional Applebaum adaptive beamformers and (b) the proposed NRPA - enhanced Applebaum adaptive beamformers having increased spatial selectivity. . . . .	71
5.2	Signal flow graph of the proposed NRPA- enhanced Applebaum adaptive array architecture. . . . .	73
5.3	Digital implementation and 2-D frequency domain behavior of the (a-b) spatial re-orientation block (c-d) linear transformation block. . . . .	78
5.4	Behavior of the desired frequency spectrum at the input of each subsystem for each operational mode (a) Mode 1 ( $\psi_d \leq \psi_c$ ) (b) Mode 2 ( $\psi_c < \psi_d \leq 0$ ) (c) Mode 3 ( $0 \geq \psi_d > -\psi_c$ ) (d) Mode 4 ( $-\psi_c \geq \psi_d$ ). . . . .	87
5.5	Expected directivity improvement of the proposed method in terms of the array factor of the beamformer. . . . .	92

5.6	Comparison of the SNR improvement of the propose NRPA enhanced Applebaum array for SM1 and SM2 with (a) varying fractional bandwidth ( $B_f$ ) of the input signal and (b) varying 2-D IIR beam filter parameter $R$ . . . . .	95
5.7	SINR improvement of SM1 and SM2 for different simulation scenarios. Variation with respect to the desired beam direction $\psi_d$ , (a) with two interference in the directions $\psi_d \pm 10$ (b) with two interference in the directions $\psi_d \pm 20$ (c) four interference in $\psi_d \pm 10$ and $\psi_d \pm 20$ . . . . .	98
6.1	Directional spectrum sensing architectures using antenna array processing and Cyclostationary featute detection: (a) conventional approach with Applebaum adaptive beamformers and (b) proposed apparoach based on 2-D IIR filter based array processing with enhanced noise suppression capability. . . . .	104
6.2	Deviation of the beam direction due to the variation of the center frequency (Applebaum coefficients are calculated for 2.4 GHz). . . . .	110
6.3	Obtained results for DOA $20^\circ$ with -30 dB SINR (a) SCF (b) PSD ( $\alpha = 0$ in the SCF) of the conventional method, (c) SCF (d) PSD of the proposed method. Results for DOA $40^\circ$ with -30 dB SINR (e) SCF (f) PSD of the conventional method, (g) SCF (h) PSD of the proposed method. Results for DOA $60^\circ$ with -30 dB SINR (i) SCF (j) PSD of the conventional method, (k) SCF (l) PSD of the proposed method. . . . .	112
6.4	(a) Resulted $M_A$ and $M_P$ metric values for different SNR situations with respect to the desired beam direction. (b) Variation of the performance metric $M$ with the input SNR. . . . .	114
7.1	Overview of the proposed architecture to enhance the directivity of the rectangular aperture digital STAP beamformer. . . . .	118
7.2	System architecture of the partially-separable 3-D IIR beam filter. . . . .	120
7.3	Frequency response of the array of 2-D IIR beam filters orented in (a) $x$ direction (b) $y$ direction (c) Frequency response of the 3-D IIR beam filter [cascade two systems in (a) and (b)]. Here desired DOA is set to be $(40^\circ, 45^\circ)$ . . . . .	122

7.4	Array factor variation of the 3-D IIR beam filter with the normalized temporal frequencies (a) $\omega_{ct0} = 0.6\pi$ , (b) $\omega_{ct0} = 0.5\pi$ and (c) $\omega_{ct0} = 0.4\pi$ (d-f) Array factor variation with respect to $\psi$ while keeping the $\phi$ unchanged. (g-i) Array factor variation with respect to $\phi$ while keeping the $\psi$ unchanged. . . . .	124
7.5	Modification of the beam filter to further enhance the directivity. . . . .	126
7.6	SIR improvement of the proposed architecture compared to the digital STAP beamformer. . . . .	136
7.7	SIR improvement of the proposed architecture compared to the digital STAP beamformer. . . . .	137
8.1	(a) Proposed 2-D IIR digital filter based transmit array. Spatio-temporal 2-D (b) impulse response and (c) frequency response of transmit array digital filter showing the directional response in the 2-D space-time domain. (d) Example 1-D sinusoidal input signal and output 2-D wave-field . . . . .	141
8.2	(a) 2-D output and (b) frequency response for a Gaussian modulated cosine input for $20^\circ$ . (c) and (d) for $40^\circ$ . (e) 2-D output and (f) frequency response for a square pulse input for $20^\circ$ . (g) and (h) for $40^\circ$ . . . . .	143
8.3	(a) Architecture for the dual-beam transmit beamformer (b) 2-D impulse response and (c) frequency response of the 2-beam transmit beamformer. . . . .	144
8.4	(a) 2-D output and (b) frequency response for a Gaussian modulated cosine input (c) 2-D output and (d) frequency response for a square pulse input for the dual-beam architecture. . . . .	145
9.1	Overview of the proposed frequency-tunable bandwidth-adjustable RF analog bandpass filter, including a multi-band filter realization, to support multiple bands with different center frequencies and bandwidths. . . . .	149
9.2	Magnitude frequency response $ H_k^{ideal}(j\omega) $ for (a) different center frequencies and (b) different bandwidths showing the frequency and bandwidth tunability. (c) Multi-band filter response from ideal all-pass model $H_k^{ideal}(s)$ for $N = 6$ bands. (d) frequency tunability, (e) bandwidth tunability, and (f) multi-band response, including the effect of low-pass parasitic pole at 27 GHz (solid) and 45 GHz (dashed). . . . .	152

9.3	Magnitude frequency responses $ H_{bp}(e^{j\omega}) $ and $ H_k^{ideal}(j\omega) $ with (a) original coefficients, $k_{1,2}$ , in the digital prototype and (b) modified coefficients, $k_{c1,c2}$ , which compensate the inverse bi-linear warping effect. . . . .	153
9.4	First order sensitivity function $S_\rho^{ H_k(j\omega) }(\omega)$ for a center frequency of 2 GHz. (b) Bandpass filter response with non-ideal all-pass gain $\rho$ . . . . .	155
9.5	(a) Schematic and layout of the current-mode CMOS all-pass filter. (b) center frequency and (c) bandwidth tunability of the bandpass filter computed using CMOS all-pass response. (d)-(f) N=6 multi-band filter response computed using CMOS response, which shows the independent tunability of each sub-band. . . . .	157

CHAPTER I  
INTRODUCTION TO HIGHLY DIRECTIONAL TRANSMISSION AND  
RECEPTION

Highly directional transmission and reception of electromagnetic waves employing an electronically scanned, directionally agile radio frequency (RF) beams can be found in many application areas, ranging from wireless communication [1, 2], mobile communication [3, 4, 5, 6], radar [7, 8, 9], cognitive radio [10, 11], space communication [12, 13], tracking and detection systems [14, 15], and radio astronomy [16, 17]. Fig. 1.1 shows an overview of such systems in a military setting, a wireless/mobile environment, and an unmanned aerial vehicle (UAV) system, respectively. Directional reception enhances the desired signals from a particular direction of arrival (DOA) while suppressing interfering signals from other directions and additive white Gaussian noise (AWGN). Similarly, directing the energy of a signal source towards a desired direction can establish a secure communication in a military setting and may increase the spectral utilization in a cognitive radio (CR) environment. Single antenna with fixed far field characteristics can be designed such a way that the antenna itself can make a directional transmission and reception. However, the antenna is unable to change its transmission or reception direction without mechanically steering the antenna. Thus, linear or rectangular antenna apertures can be combined with space-time (ST) signal

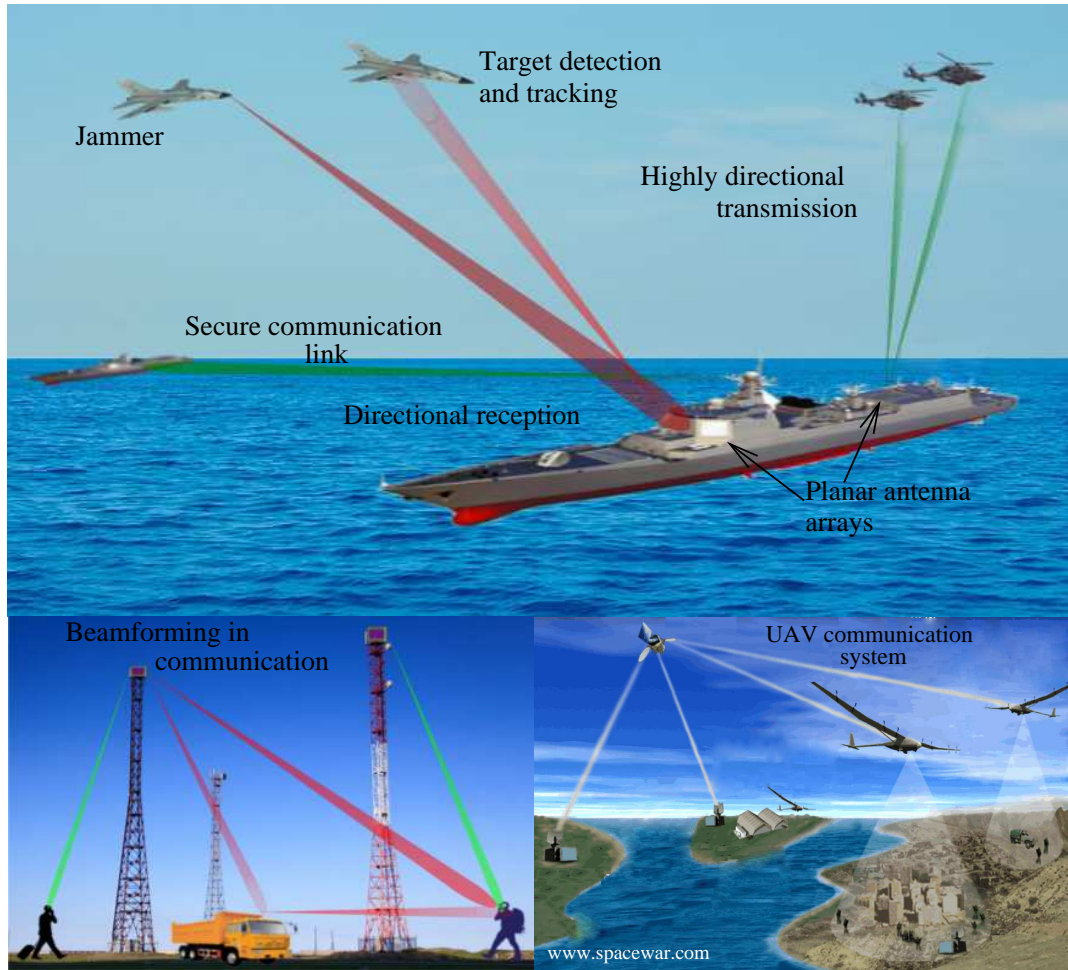


Figure 1.1: Application of highly directional, electronically steerable transmit- and receive-mode beamformers.

processing techniques to form highly directional, electronically steerable transmit- and receive-mode RF beams. Note, even with an antenna array, signal processing techniques must be applied to obtain the desired directivity.

The hardware and computational complexity towards achieving the highly directional communication is mainly determined by the operational conditions of the signal of interest. As an example, beamforming systems, which support wideband

signals (wider operational bandwidth) are highly complex compared to the narrow-band realization. Furthermore, the spatial selectivity (directivity) of the beamformer enhances with the number of antenna elements in the array, in turn, increasing the hardware complexity (for additional RF front-end equipment and signal processing hardware). Low complexity, electronically steerable, highly directional wideband beamforming systems are an open research area in the antenna array multidimensional (MD) signal processing community. In this thesis, we exploit the recently discovered network resonant-based digital infinite impulse response (IIR) beam filter [18, 19, 20, 21] towards the performance enhancement of the existing beamforming systems and its related applications in terms of hardware complexity, spatial selectivity and operational bandwidth. The following characteristics of the two- and three-dimensional (2-D/3-D) IIR digital beam filters were studied during the work.

1. Low complexity: MD IIR digital filters are less complex compared to existing ST filtering techniques, which are basically finite impulse response (FIR) in nature, in terms of the hardware utilization (in the digital signal processor). Similar directivity properties can be obtained from the proposed digital beam filters for a small number of digital hardware.
2. Large operational bandwidth: Signals that are wideband in nature can be directionally enhanced for the same computational complexity.
3. Multiple input multiple output (MIMO) nature: Following the ST input output relationship of the beam filters, the system accepts multiple inputs and produces

multiple outputs whereas the conventional beamformers have multiple inputs and a single output.

4. Inherent IIR recursive structure: The spatial FIR nature of the conventional beamformers lead to a zero manifolds-only transfer function whereas IIR beam filters contain both zero and complex pole-manifolds in their array manifold transfer function.
5. Electronic steerability: The closed form relationship of the filter coefficients and the desired DOA create an opportunity to realize real-time, electronically steerable beam filters.

## 1.1 Contributions in this Thesis

Contributions of this thesis to enhance the performance of the existing beamforming techniques and their applications, by utilizing the unique characteristics of the MD beam filters, can be summarized as follows;

1. A combined approach using low complexity array processing based on 2-D IIR digital beam filters with cyclostationary feature extraction for sensing the DOA, frequency and modulation of radio sources in a CR environment is proposed. The ultimate objective of this work is to sense the primary and secondary users' DOAs, locations, carrier frequencies, modulation/features (waveforms), polarizations, and eventually other physical parameters, such as higher order

(non-planar) propagation modes, which lead to increased flexibility at medium access (MAC) and network layers.

2. We proposed an application of rectangular antenna array-based 3-D IIR beam filter and cyclostationary feature detection algorithms to estimate the direction, carrier frequency, and modulation information pertaining to radio sources in a CR environment. A number of receiver stations equipped with planar antenna arrays and 3-D IIR digital beam filters are employed to obtain direction estimations pertaining to radio sources. The proposed architecture exhibits low complexity, and wider operational bandwidth compared to the conventional localization/ directional spectrum sensing method.
3. We formulated an IIR network resonance-enhanced Applebaum Adaptive Array for optimal beamforming. The MIMO nature of the 2-D IIR beamformer allows the placement of the filter prior to the Applebaum beamformer. The spatial selectivity of the Applebaum beamformer is enhanced by introducing complex-manifolds from the 2-D IIR beamfilter to the zero manifold-only transfer function of the adaptive beamformer. New network-resonant-phased-array (NRPA) Applebaum beamformers outperform traditional adaptive beamformers in terms of signal-to-interference and noise ratio (SINR) performance.
4. Directivity enhancement of rectangular aperture digital space-time array processor (STAP) beamformer is proposed by employing a 3-D IIR beam filter as a pre-filter to the conventional beamformer. The proposed 3-D IIR beam filter

is realized as a partially separable architecture where a 2-D IIR beamfilter is utilized as the elementary unit. Insertion of the beam filter introduces complex-pole manifolds to the zero manifold-only array transfer function of the STAP beamformer, which leads to a significant side lobe level reduction.

5. An electronically steerable, low complexity transmit beamformer based on space-time network-resonant infinite impulse response discrete systems is proposed for wideband directed energy applications. The proposed method leads to an order-of-magnitude lower digital multiplier count compared to the FIR filter based transmit arrays. Both single-beam and dual-beam architectures are introduced.
6. A radio frequency-integrated circuit (RF-IC) approach to design microwave filterbanks having multiple bands, each having independently tunable center frequency and quality factors, is proposed. The proposed technique is based on transfer function synthesis using first-order all-pass filters as a building block.

## 1.2 Publications

The research contributions are reported in one journal publication (under review) and six conference publications as listed below.

### 1.2.1 Journal Publications

1. N. Udayanga, Ar. Madanayake and C. Wijenayake, “Network Resonant Applebaum Array”, under review at IEEE Transactions on Aerospace and Electronic Systems.

### 1.2.2 Conference Publications

1. A. Madanayake, N. Udayanga, C. Wijenayake, M. Almalkawi, and V. Devabhaktuni, Directional cyclostationary feature detectors using 2-D IIR RF spiral-antenna beam digital filters, in 2014 IEEE International Symposium on Circuits and Systems (ISCAS), June 2014, pp. 2499-2502.
2. N. Udayanga, A. Madanayake, and C. Wijenayake, Direction/location estimation and modulation detection for RF sources using steerable 3D IIR digital beam filters, in Proceedings of SPIE 9103, Wireless Sensing, Localization, and Processing IX, vol. 9103, May 2014.
3. N. Udayanga, A. Madanayake, C. Wijenayake, and R. Acosta, Applebaum adaptive array apertures with 2-D IIR space-time circuit-network resonant pre-filters, in 2015 IEEE Radar Conference (RadarCon), May 2015, pp. 0611-0615.
4. A. Madanayake, N. Udayanga, C. Wijenayake, and L. Bruton, Electronically steerable directed energy using space-time network resonant digital systems, in 2015 IEEE International Symposium on Antennas and Propagation and North American Radio Science Meeting, Jul 2015.
5. N. Udayanga, A. Madanayake, and C. Wijenayake, FPGA-based network-resonance Applebaum adaptive arrays for directional spectrum sensing, in 2015 IEEE 58th Intl Midwest Symposium on Circuits & Systems (MWSCAS), Aug 2015 - Accepted.

6. N. Udayanga, A. Madanayake, C. Wijenayake, P. Ahmadi, and L. Belostotski, Tunable multiband RF CMOS active filter arrays, in 2015 IEEE International Symposium on Circuits and Systems (ISCAS), May 2015, pp. 1682-1685.

### 1.3 Thesis Outline

The rest of the chapters in this thesis unfold as follows.

Chapter 2 introduces the concepts of the linear/rectangular antenna array-based MD signal processing for directional enhancement of the plane waves from a desired DOA while suppressing any interference from other directions and AWGN noise. The spectral properties of the plane waves are described for the 2-D case followed by reviewing existing space-time filtering techniques. The theory of the network-resonant 2-D IIR beam filters for uniformly linear arrays is introduced with their design equations. Finally, the spectral properties and rectangular antenna array-based signal processing techniques are reviewed for both existing methods and the 3-D IIR beam filters.

Chapter 3 describes the application of low complexity, wideband 2-D IIR beam filters for directional spectrum sensing in a CR environment. Cyclostationary feature extraction algorithms are employed at the directionally enhanced output to estimate the modulation scheme and carrier frequency of the detected signal sources. Digital 2-D IIR filter design equations and cyclostationary feature estimation metrics are reviewed prior to the introduction of the proposed architecture. Simulation exam-

ples are provided for demonstrating the directional feature detector with applications towards enhancing access to the radio spectrum.

Chapter 4 proposes the 3-D IIR beam filter as an alternative to the conventional beamformer for direction and location estimation of primary users (PUs) in a CR environment. A cyclostationary feature detector is combined with the beam filter to estimate the modulation type and the frequency of the PU, leading to increased flexibility at MAC and network layers. Two simulation examples are provided to verify the feasibility of the proposed approach.

In Chapter 5, an architectural modification to conventional Applebaum adaptive array beamformers is proposed to achieve significant improvements in SINR. A conventional Applebaum array transfer function is modified by introducing pre-processing digital filters based on 2-D planar-resonant beam filters. The proposed architectural modification introduces complex pole-manifolds into the Applebaum array transfer function at guaranteed stability, which in turn, leads to better selectivity (i.e., reduced side lobe levels) reflected by SINR improvement. The proposed beamforming architecture shows a significant improvement in SINR when the DOA of the desired signal is off-axis from the broad side direction. A linear transformation block is proposed to further improve the performance of the proposed method in terms of SINR improvement around the broadside direction of the antenna array. The combination of the 2-D IIR beamfilter and transformation provides improvement along every beam direction.

Chapter 6 combines the network-resonant beam filter-enhanced Applebaum beamformer that is discussed in Chapter 5 and cyclostationary feature detection towards addressing the false detections of PUs due to high levels of noise in a CR environment. Simulation results shows the noise suppression capability of the cyclostationary estimator with respect to the desired beam direction.

Beam enhancement to the conventional fast Fourier transform (FFT)- based STAP beamformer is proposed in Chapter 7 by employing a 3-D IIR beam digital filtering architecture as a pre-filter to the existing system. 3-D IIR beam filter is realized using 2-D IIR beam filters to reduce the hardware complexity of the direct form implementation of the 3-D filter. Spatial selectivity enhancement of the proposed architecture is quantified using the relative signal-to-interference ratio (SIR) improvement compared to the conventional system.

A novel digital wideband transmit beamforming method is proposed in Chapter 8 based on space-time network-resonant infinite impulse response digital architectures to obtain reduced hardware complexity compared to the conventional finite impulse response-based transmit beamformers. Obtaining multiple beams without duplicating the hardware for a single beam is an added advantage of the proposed architecture. Both single- and dual-beam architectures are introduced in the chapter.

In Chapter 9, a frequency and bandwidth agile, multi-passband analog filter array is introduced towards potential applications in emerging radio frequency field programmable gate array (RF-FPGA) type reconfigurable radio front-ends. The proposed analog filter is based on a novel transfer function synthesis technique employing

first-order all-pass filters. Finally, Chapter 10, provides a summary of the work carried out in this thesis, and potential future work.

CHAPTER II

LINEAR/RECTANGULAR APERTURE BASED MULTIDIMENSIONAL  
SIGNAL PROCESSING

One dimensional (1-D) signal processing techniques are employed to process signals, which are described using a single independent variable whereas MD signal processing techniques are able to process signal data that are represented using more than one dimension. Consider a signal source  $S$ , which is transmitting a time varying signal  $w_s(t)$  from a far away location as shown in Fig. 2.1. A propagating wave in the  $(x, y, z) \in \mathbb{R}^3$  3-D space, at a sufficiently large distance  $d$ , where  $d \gg \lambda$  (here  $\lambda$  is the wave length of the signal), can be expressed as a four-dimensional (4-D) ST plane wave signal  $w_{pw}$  [18, 19]

$$w_{pw}(x, y, z, ct) = w_s(\alpha_x x + \alpha_y y + \alpha_z z + ct) \quad (2.1)$$

where  $(\alpha_x, \alpha_y, \alpha_z)$  is the unit vector normal to the plane wave front (parallel to the direction of propagation) and  $ct$  is the time normalized by the propagation speed of the wave  $c$  in the propagation medium. Consider a situation where a 4-D ST plane wave  $w_{pw}$  is sampled by a single antenna in the space as shown in Fig. 2.2(a). Since the spatial location of the receiving antenna is fixed at  $(x_0, y_0, z_0)$ , corresponding sampled signals can be described by a single independent variable  $ct$  as  $w(ct) =$

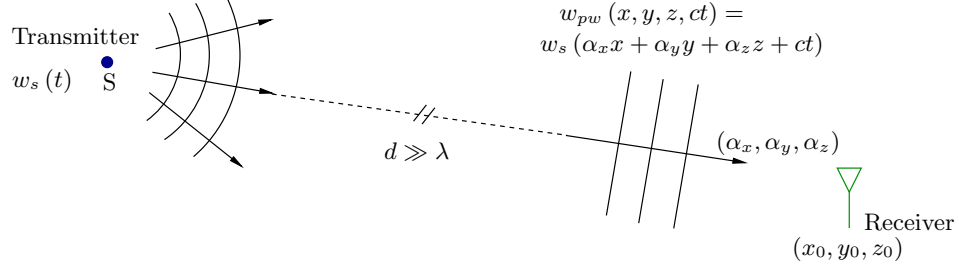


Figure 2.1: Plane wave propagating from a faraway source  $S$ .

$w_s(\alpha_x x_0 + \alpha_y y_0 + \alpha_z z_0 + ct) = w(ct)$ . Thus, the system becomes 1-D, and 1-D signal processing techniques can be employed to process sampled data. When the 4-D ST plane wave is spatially sampled by a uniformly spaced linear antenna array with  $N$  antenna elements and the inter-antenna spacing  $\Delta x$  as shown in Fig.2.2(b), the corresponding system can be expressed using two independent variables  $x$  and  $ct$

$$w(x, ct) = w_s(\alpha_x x + ct) \quad (2.2)$$

where  $x = n_x \Delta x$  and  $n_x = 1, 2, \dots, N$  is the antenna index. Since the system can be described using two variables, 2-D signal processing techniques are able to process signal data to obtain a desired output. Similarly, if the signal is spatially sampled using a rectangular antenna array as shown in Fig. 2.2(c), 3-D signal processing techniques need to be employed to process the entire captured signal.

Consider the example shown in Fig. 2.3, which describes the transmit beamforming concept for a 2-D case using 4-element antenna array consisting of omnidirectional antenna elements. In transmit beamforming, the signal energy of the signal source needs to be directed into a particular direction  $\psi$  where it has the desired

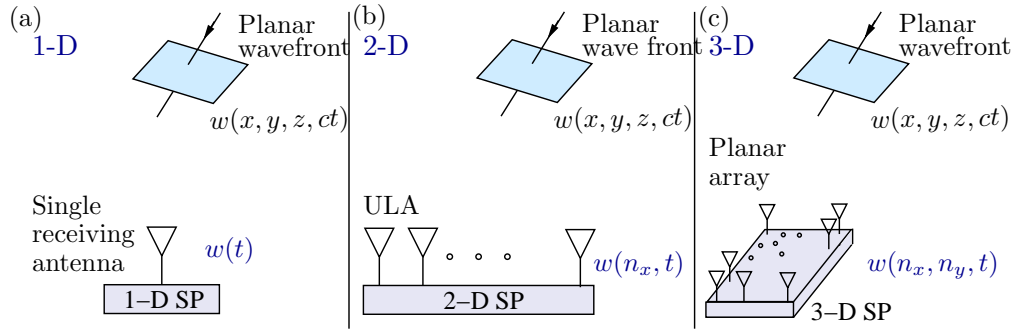


Figure 2.2: Overview of the multidimensional signal processing, (a) one-dimensional, (b) two-dimensional, (c) three-dimensional systems.

receiver. The radiation pattern of a single antenna is shown in Fig. 2.3(a), where it transmits the same signal power in every direction. One antenna element does not have a degree of freedom to control the direction of energy transmission electronically since it has a fixed radiation pattern for itself. Mechanical steering of the antenna is the only option to change the transmission direction for single antenna with an angle-dependent radiation pattern. Consider the antenna array oriented at  $x$  direction as shown in Fig. 2.3(b), and transmit the same signal from each antenna (without employing any signal processing), the resulted wave patterns generate a beam toward the broadside direction of the antenna array. Fig. 2.3(c) shows a situation where a signal processor applies a gradually decreasing delay along the antenna array, prior to the transmission. Introduction of the delay architecture (signal processing) changes the radiation wave pattern by producing a beam into the direction of the desired receiver. By changing the delay values appropriately, the beam can be steered towards any direction in the  $(x, y)$  plane. Thus, antenna arrays combined with signal processing techniques can be used to implement an electronically steerable transmit

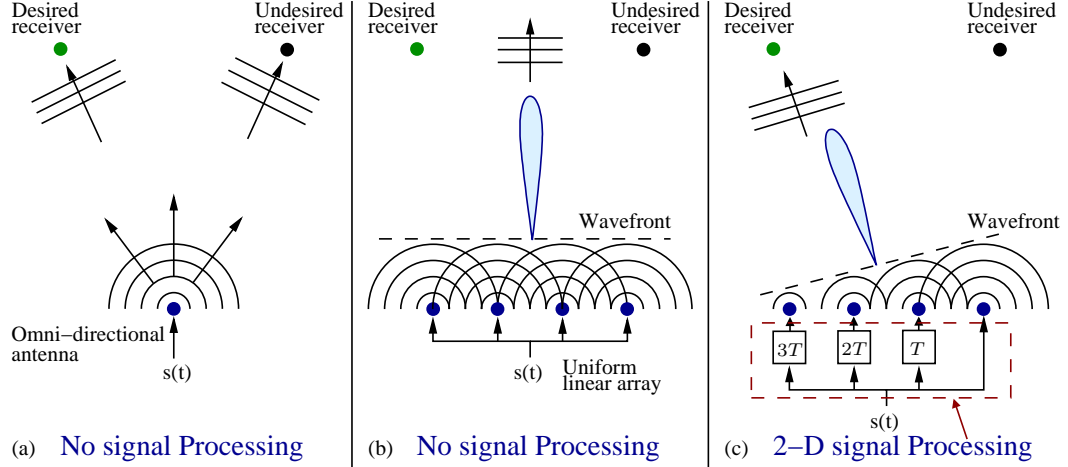


Figure 2.3: Multidimensional signal processing for transmit beamforming (a) single antenna with no signal processing (b) antenna array with no signal processing (c) antenna array with 2-D signal processing.

beamformer. It is clear that even with an antenna array, we require a signal processing step before the transmission to obtain the desired behavior, which can never be achieved using a single omnidirectional antenna.

## 2.1 2-D Discrete ST Plane Wave Signals and Their Spectra

Consider a plane wave arriving from a DOA  $\psi$ , ( $-90^\circ \leq \psi \leq 90^\circ$ ) as shown in Fig. 2.4(a). The direction is measured with respect to the broadside direction of the antenna array in the counter clockwise direction. The plane wave is sampled using an antenna array oriented in  $x$  direction with inter-antenna spacing  $\Delta x$ . The time taken to travel a plane wave from an antenna to its neighboring antenna  $\Delta T_x$  can be calculated as [19, 20]

$$\Delta T_x = \frac{\Delta x}{c} \sin \psi \quad (2.3)$$

The same plane wave shown in Fig. 2.4(a) can be represented in the  $(x, ct)$  space-time domain as shown in Fig. 2.4(b). Here, the spatial DOA  $\psi$  is mapped into an ST DOA  $\theta$ , where the relationship between  $\psi$  and  $\theta$  can be expressed as  $\tan \theta = \sin \psi$ . It is clear that plane waves from spatial DOAs ( $-90^\circ \leq \psi \leq 90^\circ$ ) are confined into a  $45^\circ$  light cone ( $-45^\circ \leq \theta \leq 45^\circ$ ) in the space-time domain.

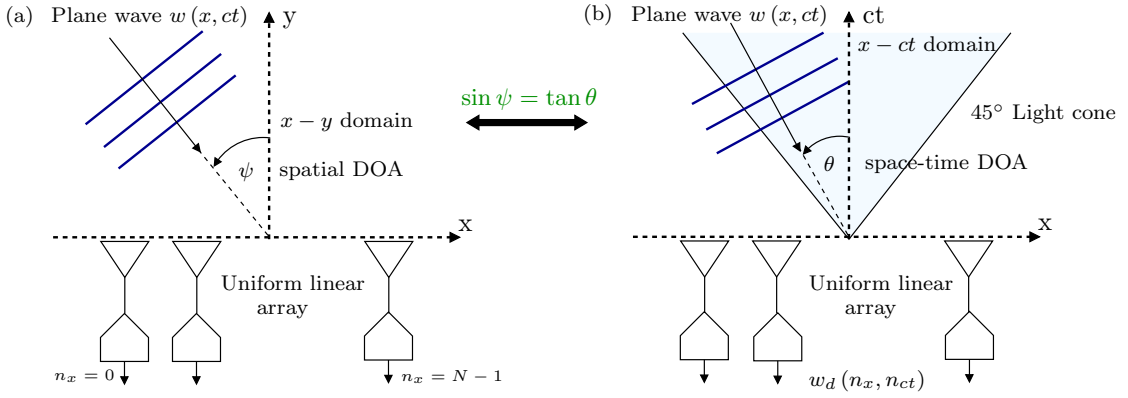


Figure 2.4: Plane wave representation in (a)  $x - y$  and (b)  $x - ct$  domains.

In order to discretize the received signals, analog to digital converters (ADCs) are employed after each antenna where sampling frequency of the ADC is denoted as  $F_s = 1/\Delta T$ . Thus, the discrete domain 2-D space-time signal is given by [19, 20, 21]

$$w_d(n_x, n_{ct}) = w(\Delta x n_x, c \Delta T n_{ct}) = w_s(-\sin \psi \Delta x n_x + c \Delta T n_{ct}) \quad (2.4)$$

where  $\alpha_x = -\sin \psi$ . In order to analyze the  $(\omega_x, \omega_{ct}) \in \mathbb{R}^2$  2-D frequency spectrum of the 2-D discretized signal, consider the 2-D Fourier transform of the signal

$w_d(n_x, n_{ct})$  [18, 19, 20]

$$W_d(\omega_x, \omega_{ct}) = \sum_{n_x=0}^{N-1} \sum_{n_{ct}=-\infty}^{\infty} w_d(n_x, n_{ct}) e^{-j\omega_x n_x} e^{-j\omega_{ct} n_{ct}} \quad (2.5)$$

where  $j = \sqrt{-1}$ . MD signal processing theory shows that the region of support (ROS) of a plane wave from a DOA  $\psi$  is confined into a straight line in the  $(\omega_x, \omega_{ct})$  2-D frequency domain, which is passing through the origin and has an angle  $\theta$  to the  $\omega_{ct}$  axis as shown in Fig. 2.5(a) [18]. The equation of the ROS line is given by

$$\omega_{ct} + \omega_x \sin \psi = 0. \quad (2.6)$$

Here, ROS is the region where the magnitude of the frequency spectrum is defined to be nonzero. Fig. 2.5(b) and Fig. 2.5(c) show the frequency spectra for a signal consisting of three narrowband cosine signals and three wideband Gaussian-modulated cosine signals, respectively. Since the signals are receiving from three different angles,  $60^\circ$ ,  $40^\circ$ , and  $10^\circ$ , the frequency spectrum of each signal lies on different lines inclined to the  $\omega_{ct}$  axis. Thus, a ST filtering system, which has a line-shaped passband oriented at  $\theta$  ( $\tan \theta = \sin \psi$ ), is required to selectively enhance signals from a DOA  $\psi$ .

In the next section, the conventional 2-D ST filtering techniques, which are designed to directionally enhance plane waves from a particular DOA, will be reviewed. Generally, such systems are called as receive beamformers, since they form a beam towards the desired direction to selectively filter out signals from a particular DOA. This thesis covers on the receive beamforming technique, which is developed based on the concept “MD network-resonant passive prototype networks”. Addition-

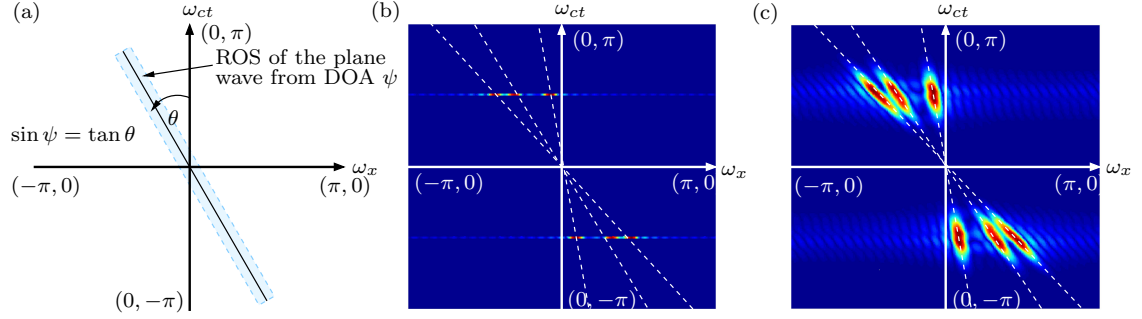


Figure 2.5: (a) ROS of the signals from DOA  $\psi$ . 2-D  $(\omega_x, \omega_{ct})$  frequency spectrum of the (b) narrowband signals and (c) wideband signals from three different angles,  $60^\circ$ ,  $40^\circ$ , and  $10^\circ$ .

ally, Chapter 8 describes a novel transmit beamforming technique based on space-time network-resonant digital systems.

## 2.2 Conventional 2-D ST Filtering Techniques - Receive Beamformers

Receive mode beamformers (ST filtering techniques) employ MD signal processing techniques (with antenna arrays) to selectively enhance signals from a particular DOA  $\psi$  while suppressing signals from other directions and random noise. ST filtering techniques can mainly be classified into two categories based on the frequency content of the signal of interest, narrowband and wideband. Narrowband beamformers operate only in a particular frequency band whereas wideband beamformers operate within a large range of frequencies. Moreover, filtering techniques can be classified into time and frequency domains based on the implementation strategy. Time domain implementation processes data at the ADC outputs directly, whereas frequency domain systems obtain the frequency spectrum of the input signals prior to the signal pro-

cessing. Here, conventional approaches to achieve receive beamforming are discussed briefly.

Narrowband beamformers accept input signals, which have a signal spectrum as shown in Fig. 2.5(b), and the out-of-band interferences are suppressed employing a bandpass filter prior to the digital signal processor. Thus, the passband of the narrowband beamformer needs to be aligned with the input signal frequency spectrum only at the desired frequency  $\omega_{ct0}$  [1]. A true-time-delay-sum beamformer shown in Fig. 2.6(a) can be implemented in the analog domain where corresponding delays are implemented using optical and electronic delay lines. Optical methods modulate the RF signal onto an optical carrier and use long fibers to delay the signal. Electronic methods use traditional microstrip lines or coax cables to delay the signal. Delay line length can be changed accordingly to obtain the desired delay  $\Delta_x T$ . In order to have a beam direction in  $\psi$ , delay line lengths can be selected to have delays as shown in Fig. 2.6(a), where  $\Delta_x T = \frac{\Delta x}{c} \sin \psi$ . Then, the outputs of each antenna are summed together to reinforce the effective radiation pattern of the array in the desired direction while suppressing the waves coming from other directions. Directionally enhanced output  $y(ct)$  can be expressed as [22, 23]

$$y(ct) = \sum_{n_x=0}^{N-1} w(n_x, c(t - (N - n_x) \Delta_x T)) \quad (2.7)$$

Fig. 2.6(b) shows the system architecture of the phased array beamformer, which can be considered as the most common type of narrowband beamformer [24]. Following

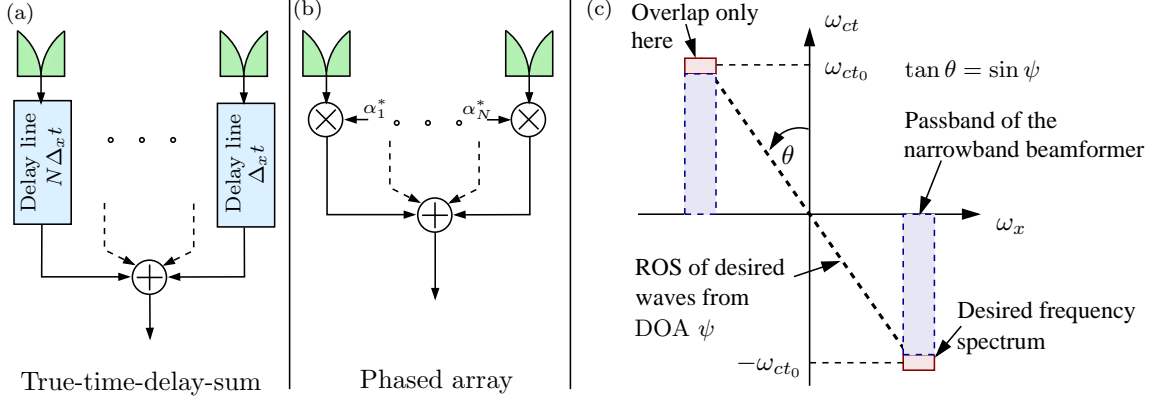


Figure 2.6: System overview of the (a) true-time-delay-sum beamformer, (b) phased array, and (c) 2-D Frequency response of the narrowband beamformer.

the relationship of the delay between time domain and frequency domain,

$$w(t - t_0) \leftrightarrow W(\omega) e^{-j\omega t_0}, \quad (2.8)$$

time domain delay  $t_0$  can be obtained in the frequency domain by multiplying the signal by  $e^{-j\omega t_0}$  (phase rotation). Since the system is narrowband and operates at frequency  $\omega_{ct_0}$ , each antenna output is directly multiplied by the appropriate complex phasor to obtain the required delay. Phase-rotated signals are then summed to obtain the directionally enhanced output  $y(ct)$  as expressed in the following;

$$y(n_{ct}) = \sum_{n_x=0}^{N-1} w(n_x, n_{ct}) * e^{-j(N-n_x-1)\omega_{ct_0}\Delta T}. \quad (2.9)$$

The ST filtering techniques discussed above have a passband as shown in Fig. 2.6(c) where the signal spectrum correspond to DOA  $\psi$  and passbands are overlapped only at the frequency  $\omega_{ct_0}$ . For different frequency values, the filtering angle is different from the desired DOA. Narrowband beamformer with coefficients  $\alpha_{n_x} = e^{-j(N-n_x-1)\omega_{ct_0}\Delta T}$ ,

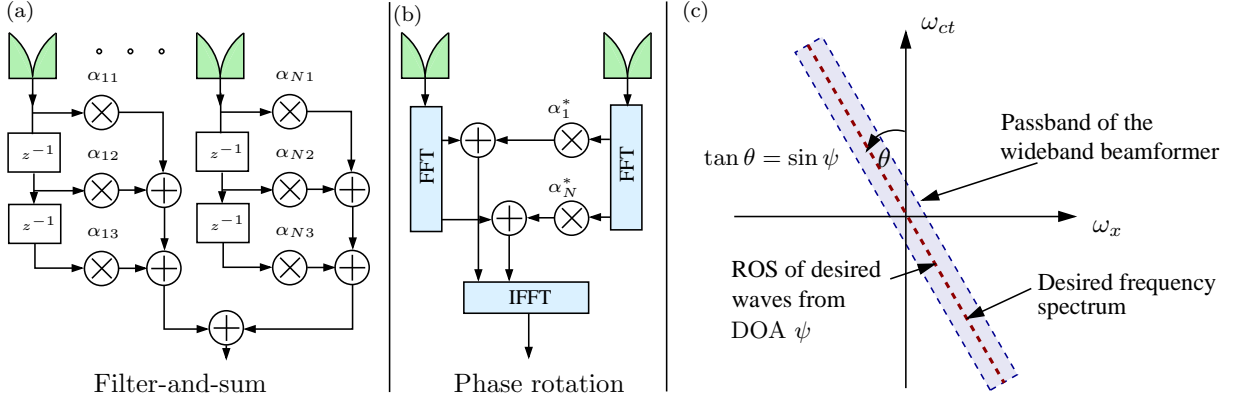


Figure 2.7: System overview of the (a) filter and sum architecture, (b) FFT-based wideband beamformer, and (c) 2-D frequency response of wideband beamformers.

can be modeled as a spatial FIR system having the  $\mathbf{z}$  domain transfer function [25]

$$T_{PA2D}(z_x) = \frac{1}{N} \sum_{n_x=0}^{N-1} \alpha_{N-n_x-1} z_x^{-n_x}. \quad (2.10)$$

Note that (2.10) contains only zero-manifolds in the array transfer function. The selectivity of the transfer function can be enhanced by increasing the number of antenna elements  $N$  in the array, which corresponds to the order of the spatial FIR filter.

Wideband beamformers can be implemented in both time and frequency domains [26, 27]. The time domain implementation, filter and sum architecture shown in Fig. 2.6(c) can be considered as a array of digital FIR filters where each filter output is then combined to obtain the beamformed output  $y(n_{ct})$ . Thus, the discrete time output of the beamformer can be expressed as,

$$y(n_{ct}) = \sum_{n_x=0}^{N-1} \sum_{i=1}^3 \alpha_{n_x i} w(n_x, n_{ct} - i) \quad (2.11)$$

where  $\alpha_{n_x i}$  are the coefficients correspond to antenna index  $n_x$  and  $i^{th}$  tapped point of the delay line. Frequency domain implementation of the wideband beamformer is an extension of the phased array architecture that we discussed earlier. As shown in Fig. 2.6(d), P-point FFT is employed at each of the inputs to obtain signals corresponding to each frequency bin  $W(n_x, \omega_{ct_i})$ , where  $\omega_{ct_i} = \frac{2\pi}{P}i$ ,  $P/2 \leq i \leq P/2 - 1$ . Outputs corresponding to the same frequency bin result a system similar to the narrowband phased array. Thus, each frequency bin corresponding to  $\omega_{ct_i}$  is multiplied using the complex phasor  $e^{-j\omega_{ct_i}(N-n_x-1)\Delta_x T}$ . Phase-rotated signals corresponding to the same frequency bin  $\omega_{ct_i}$  are then summed and fed into the inverse fast Fourier transform (IFFT) block. The following equation represents the combined output  $Y_{FFT}(\omega_{ct_i})$  at the input of the IFFT block:

$$Y_{FFT}(\omega_{ct_i}) = \sum_{n_x=0}^{N-1} W(\omega_{ct_i}) e^{-j\omega_{ct_i}(N-n_x-1)\Delta_x T}. \quad (2.12)$$

Directionally enhanced output can be found at the output of the IFFT block. It is clear that all of the beamforming systems that we described above can be considered as FIR filtering-based architectures, which have only zero manifolds in the  $\mathbf{z}$  domain transfer function. In the next section, we will introduce a recently proposed time domain wideband beamformer [20, 19], which is realized based on network resonance of the MD IIR filters which have both zero and complex pole-manifolds in the transfer function.

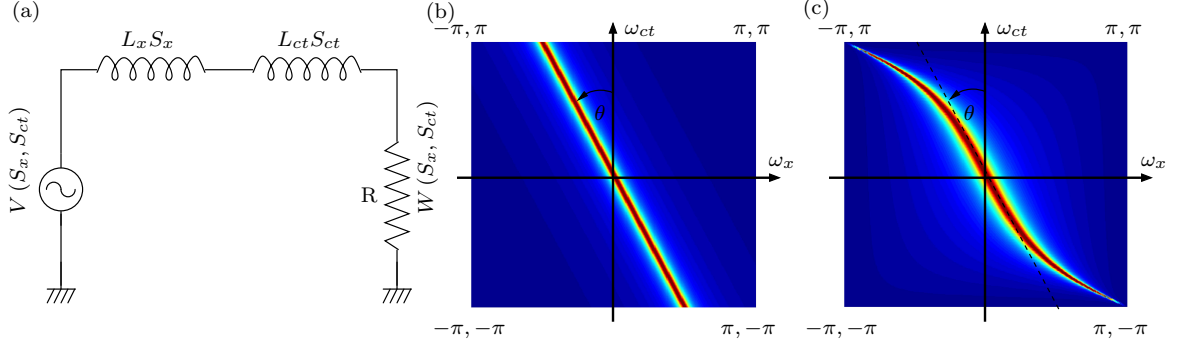


Figure 2.8: (a) 2-D first order Ramamoorthy-Bruton network (RBN). Frequency response of (b)  $H(s_{ct}, s_x)$  and (c)  $T(z_x, z_{ct})$  for  $R = 0.01$  and  $\psi = 30^\circ$ .

### 2.3 Network-Resonant-Based 2-D IIR Beam Filters for Wideband ST Filtering

Recall from Section 2.1 that the signal receiving from a particular DOA  $\psi$  has a line shaped ROS in the  $(\omega_x, \omega_{ct})$  plane which passes through the origin and has an angle  $\theta$  to the  $\omega_{ct}$  axis. Thus, a system, which has a line/beam shaped passband and satisfies (2.6), is required to implement a wideband beamformer. Resistively terminated passive prototype networks, also known as Ramamoorthy-Bruton networks (RBN) [18] based on the concept of network resonance, allow synthesis of such filters, which are IIR in nature [19, 20, 21]. Consider the 2-D ST passive network shown in Fig. 2.8(a), where two inductors  $L_{ct}$  and  $L_x$  are correspond to the normalized time  $ct$  and spatial  $x$  dimensions, respectively. The  $\mathbf{S}$  domain transfer function of the circuit  $H(s_{ct}, s_x)$  can be expressed as,

$$H_{2D}(s_{ct}, s_x) = \frac{R}{R + L_{ct}s_{ct} + L_x s_x} \quad (2.13)$$

where  $s_x$  and  $s_{ct}$  Laplace variables corresponding to two dimensions  $ct$  and  $x$ . 2-D frequency response  $H_{2D}(e^{j\omega_x}, e^{j\omega_{ct}})$  of the ST filter can be obtained by substituting

the values  $s_{ct} = j\omega_{ct}$  and  $s_x = j\omega_x$

$$H_{2D}(e^{j\omega_x}, e^{j\omega_{ct}}) = \frac{R}{R + jL_x\omega_x + jL_{ct}\omega_{ct}}. \quad (2.14)$$

The 2-D system resonates when the condition

$$L_{ct}\omega_{ct} + L_x\omega_x = 0. \quad (2.15)$$

is met [18, 19, 20]. This will lead to a line/beam shaped passband in the  $(\omega_x, \omega_{ct})$  2-D frequency domain, as expected. By analyzing (2.6) and (2.15), we can select  $L_x = \cos \theta$  and  $L_{ct} = \sin \theta$  to obtain a line shape passband, which exactly lies on the ROS of the signal receiving from DOA  $\psi$ . Fig. 2.8(b) shows the frequency response for a beam orientation  $\psi = 30^\circ$  and  $R = 0.01$ , where the magnitude  $|H(e^{j\omega_x}, e^{j\omega_{ct}}) = 1|$  when  $\sin \theta \omega_{ct} + \cos \theta \omega_x = 0$ .

Following the bilinear transformation, by substituting  $s_x = \frac{1-z_x^{-1}}{1+z_x^{-1}}$  and  $s_{ct} = \frac{1-z_{ct}^{-1}}{1+z_{ct}^{-1}}$ , a 2-D  $\mathbf{z}$  domain transfer function corresponding to (2.25) can be obtained as [19, 20]

$$T_{2D}(z_x, z_{ct}) = \frac{(1 + z_x^{-1})(1 + z_{ct}^{-1})}{1 + b_{01}z_x^{-1} + b_{01}z_{ct}^{-1} + b_{11}z_x^{-1}z_{ct}^{-1}} \quad (2.16)$$

where its coefficients are  $b_{ij} = \frac{R+(-1)^i \cos \theta + (-1)^j \sin \theta}{R + \cos \theta + \sin \theta}$ . Here,  $\theta$  and  $R$  set the angular orientation and sharpness of the passband, respectively. Note that, unlike conventional beamformers, which have only zero manifolds in the transfer function, 2-D IIR beam filters have both zeros and complex-pole manifolds in the transfer function. Since (2.16) does not depend on the antenna array size (number of antenna elements), the transfer function is applicable only if the array size is large enough to stabilize the

impulse response of the beam filter or the array size is infinite. An array transfer function, which accounts the number of antenna elements in the array, is obtained in Chapter 3. Fig. 2.8(c) shows an example 2-D magnitude frequency response computed by evaluating (2.16) on the unit bi-circle  $z_k = e^{j\omega_k}$ ,  $k \in \{x, ct\}$ , for beam orientation  $\psi = 30^\circ$  and  $R = 0.01$ . The discrete domain 2-D frequency response exhibits frequency warping due to the application of bilinear transform [28]. Due to warping, when the beam filter is designed for DOA  $\psi$ , the actual beam direction in the array factor is not exactly  $\psi$  and is given by [29, 30]

$$\psi' = \sin^{-1} \left[ \frac{2}{\omega_{ct0}} \tan^{-1} \left[ \sin \psi \tan \left( \frac{\omega_{ct0}}{2} \right) \right] \right], \quad (2.17)$$

where  $\omega_{ct0}$  is the temporal frequency at which the array factor is computed. Thus, the filter coefficient calculation needs to follow  $\psi''$  given in

$$\psi'' = \sin^{-1} \left[ \frac{\tan \left( \frac{\omega_{ct0}}{2} \sin \psi_0 \right)}{\tan \left( \frac{\omega_{ct0}}{2} \right)} \right], \quad (2.18)$$

when implementing a 2-D IIR beam filter to enhance signals from  $\psi_0$ .

## 2.4 Practical Bounded-Input-Bounded-Output (p-BIBO) Stability of 2-D IIR Beam Filters

Since the underlining transfer function is IIR in nature, maintaining the stability of the system is more critical during the actual implementation. For a 2-D discrete system defined by its 2-D impulse response  $h(n_x, n_{ct})$ , conventional BIBO stability implies that all bounded 2-D input sequences  $|w(n_x, n_{ct})| < \infty$  should result in a

bounded 2-D output sequence  $|y(n_x, n_{ct})| < \infty$  when computed recursively in a spatially and temporally unbounded grid given by  $G \equiv (n_x, n_{ct})$  [31]. Thus, conventional BIBO stability requires the 2-D impulse response of the system to be absolutely summable in  $G$ , leading to the stability requirement given by [31]

$$\sum_{n_x=0}^{\infty} \sum_{n_{ct}=0}^{\infty} |h(n_x, n_{ct})| < \infty. \quad (2.19)$$

However, in a practical scenario where the spatial index  $n_x$  of the ULA is always bounded by the number of elements in the array, summation in (2.19) never goes up to infinity. Thus, the definition of conventional BIBO stability fails to provide sufficient insight in the presence of 2-D recursive systems comprising of finite elements. Alternatively, Practical BIBO provides a lenient, yet practically relevant stability requirement where one of the multiple dimensions is allowed to be unbounded while preserving p-BIBO stability [32]. Under p-BIBO, the stability criterion in (2.19) is reduced to

$$\sum_{n_x=0}^{N-1} \sum_{n_{ct}=0}^{\infty} |h(n_x, n_{ct})| < \infty \quad (2.20)$$

where the spatial index of the computational grid is allowed to be bounded. It has been proven that discrete domain transfer functions  $T(z_x, z_{ct})$  derived based on a RBN are guaranteed to be p-BIBO-stable [32]. Selection of the filter coefficients  $L_x \geq 0, L_{ct} \geq 0$  and  $R \geq 0$  make the filter stable for  $0^\circ \leq \psi < 90^\circ$ .

## 2.5 MD Signal Processing With Rectangular Apertures

In this section, we describe the MD properties of 3-D ST plane waves signals followed by introducing rectangular antenna array-based MD processing techniques to directionally enhance plane waves. Application of planar array beamformers includes radar, 3-D volume scanning systems, threat tracking and detection systems, which can mainly be found in mission critical military applications.

### 2.5.1 3-D Discrete ST Plane Wave Spectra

Consider a 3-D plane wave  $w(x, y, ct) = w_s(\sin \psi \cos \phi x + \sin \psi \sin \phi y + ct)$  arriving from a DOA  $(\psi, \phi)$ , where  $\psi$  is the elevation angle,  $\phi$  is the azimuth angle and  $w_s(t)$  is the transmitted signal from the transmitter as shown in Fig. 2.9(a). The plane wave is spatially sampled using an uniform rectangular antenna array oriented in  $x - y$  plane with  $N_x \times N_y$  antenna elements (with same omnidirectional characteristics), where inter-antenna spacing for each direction is selected as  $\Delta d$ .  $N_x$  and  $N_y$  are the number of antenna elements in  $x$  and  $y$  directions respectively. The output of each antenna element is sent through a low noise amplifier, bandpass filter prior to the ADC, which take samples in every  $\Delta T$  seconds, where sampling frequency  $F_s = \frac{1}{\Delta T}$ . 3-D discrete signal  $w(n_x, n_y, n_{ct})$  [18, 30]

$$w(n_x, n_y, n_{ct}) = w_s(\sin \psi \cos \phi \Delta d n_x + \sin \psi \sin \phi \Delta d n_y + c\Delta T n_{ct}) \quad (2.21)$$

can be obtained at the output of the ADCs. The ROS and frequency domain properties of the 3-D plane wave can be determined by obtaining the Fourier transform

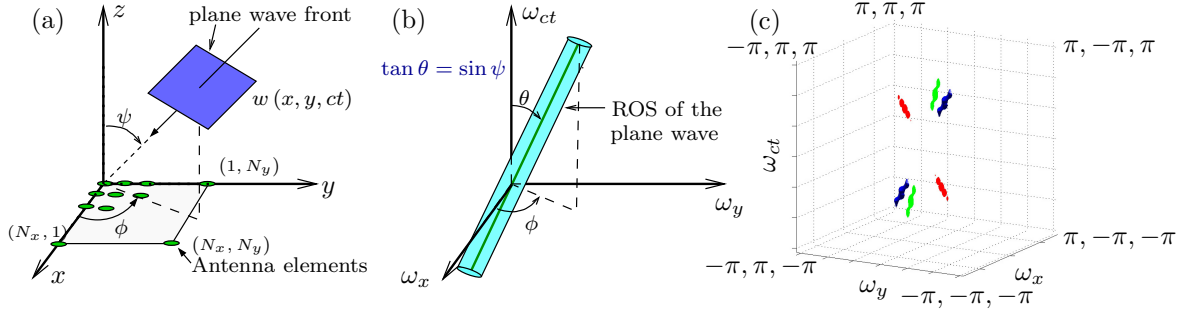


Figure 2.9: (a) A plane wave signal in  $(x, y, z)$  with the DOA  $(\psi, \phi)$ . (b) The line-shaped spectral ROS of the plane wave signal. (c) 3-D frequency spectrum for incoming signals from  $(30^\circ, 90^\circ)$ ,  $(50^\circ, 180^\circ)$ , and  $(20^\circ, 270^\circ)$ .

of the 3-D discrete signal  $w(n_x, n_y, n_{ct})$ . *MD signal processing theory shows that the ROS of the plane wave coming from a DOA  $(\psi, \phi)$  is confined to a straight line in the  $(\omega_x, \omega_y, \omega_{ct}) \in \mathbb{R}^3$  3-D frequency domain, which is passing through the origin, has an angle  $\theta$  to the  $\omega_{ct}$  axis and an angle  $\phi$  to  $\omega_x$  axis (See Fig. 2.9(b)). Here  $\tan \theta = \sin \psi$ ,  $\omega_x$ ,  $\omega_y$  are the normalized spatial frequency variables, and  $\omega_{ct}$  is the temporal frequency variable [18]. The equation of the ROS line is given by*

$$\frac{\omega_x}{\sin \theta \cos \phi} + \frac{\omega_y}{\sin \theta \sin \phi} + \frac{\omega_{ct}}{\cos \theta} = 0. \quad (2.22)$$

Fig. 2.9(c) shows the 3-D frequency spectrum of the signal consisting with 3 wide-band signals from DOAs  $(30^\circ, 90^\circ)$ ,  $(50^\circ, 180^\circ)$ , and  $(20^\circ, 270^\circ)$ , which satisfy (2.22). Thus, 3-D wideband beamformers necessitate to having a line/beam-shaped passband described by Eq. 2.22 to selectively enhance the signal from the DOA  $(\psi, \phi)$ . The next section will briefly describe the theory of the FFT-based conventional 3-D beamformers followed by introducing the network-resonant-based 3-D IIR beam filters.

### 2.5.2 FFT-based Wideband Space-Time Array Processor

A 3-D narrowband phased array beamformer (can be derived based on the 2-D phased array described in Section 2.2) delays the signals at each antenna with a proper time and coherently add them to obtain the directionally enhanced output. Thus, the  $\mathbf{z}$  domain transfer function  $T_{PA_{3D}}(z_x, z_y, z_{ct})$  of the ST phased array operating at frequency  $\omega_{ct}$  can be expressed as

$$T_{PA_{3D}}(z_x, z_y, z_{ct}) = \sum_{n_x=0}^{N_x-1} \sum_{n_y=0}^{N_y-1} \alpha_{N_x-n_x-1, N_y-n_y-1} z_x^{-n_x} z_y^{-n_y} \quad (2.23)$$

where  $\alpha_{n_x n_y} = e^{-j\omega_{ct_0} \Delta_{xy} T}$  and  $\Delta_{xy} T = \frac{1}{c} (\sin \psi \cos \phi \Delta d n_x + \sin \psi \sin \phi \Delta d n_y)$  is the time taken for plane wave to travel from the origin of the  $x - y$  plane to any antenna position  $(n_x, n_y)$ . Note that the  $T_{PA_{3D}}(z_x, z_y, z_{ct})$  has only zero manifolds in the transfer function. The wideband version of the phased array, a FFT-based STAP beamformer, is a frequency domain beamforming technique [27, 26]. As shown in Fig. 2.10, P-point FFT is employed at each of the antenna outputs to obtain signals corresponding to each frequency bin  $W(n_x, n_y, \omega_{ct_i})$ , where  $\omega_{ct_i} = \frac{2\pi}{P} i$ ,  $P/2 \leq i \leq P/2 - 1$ . Collectively, outputs corresponding to the same frequency bin result a system similar to the narrowband phased array. Thus, each frequency bin corresponding to  $\omega_{ct_i}$  is multiplied using the complex phasor  $e^{-j\omega_{ct_i} \Delta_{xy} T}$  to delay the signal for a proper time. Phased-rotated signals corresponding to same frequency bin  $\omega_{ct_i}$  are then summed and fed into the IFFT block. The following equation represents the combined output  $Y_{FFT}(\omega_{ct_i})$  at the input of the IFFT block:

$$Y_{FFT}(\omega_{ct_i}) = \sum_{n_x=0}^{N-1} \sum_{n_y=0}^{N-1} W(n_x, n_y, \omega_{ct_i}) e^{-j\omega_{ct_i} \Delta_{n_x n_y} T}. \quad (2.24)$$

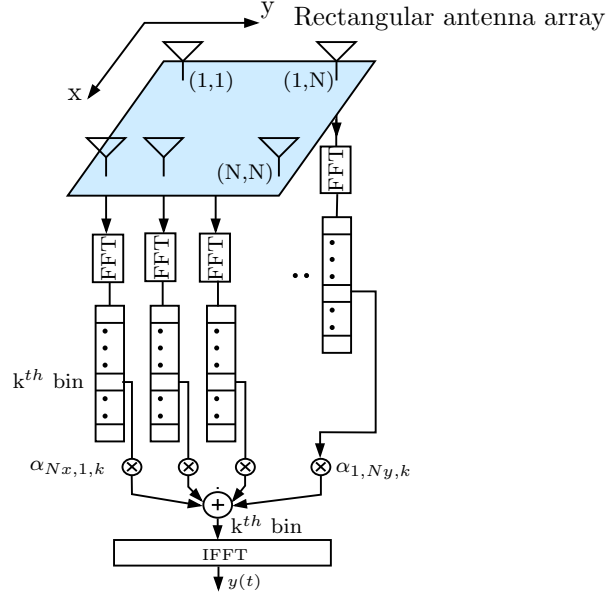


Figure 2.10: System architecture of the FFT-based wideband STAP

The directionally enhanced output  $y(n_{ct})$  can be found at the output of the IFFT block. Since the wideband FFT-based STAP beamformer is an extension of the narrowband phased array beamformers described by Eq. 2.23, the complete system can be considered as a FIR filter-based beamformer, which contains only zero manifolds in the  $\mathbf{z}$  domain transfer function  $T_{STAP}(z_x, z_y, z_{ct})$ .

### 2.5.3 Network-Resonant 3-D IIR Beam Filters

Three dimensional (3-D) IIR filters having beam-shaped passbands in  $\boldsymbol{\omega} \equiv (\omega_x, \omega_y, \omega_{ct})$  can be designed using the concept of multidimensional passive network resonance [18] (similar to the 2-D case with an additional inductor  $L_y$  for spatial direction  $y$ ). Consider the 3-D Laplace transform domain transfer function  $H(s_x, s_y, s_{ct})$  of a resistively

terminated inductor-resister prototype network given by [18, 33]

$$H(s_x, s_y, s_{ct}) = \frac{R}{R + s_{ct}L_{ct} + s_xL_x + s_yL_y}, \quad (2.25)$$

where  $R > 0$  is the resistive termination and  $L_x, L_y, L_{ct}$  are passive inductor values. Laplace variables  $s_x, s_y$  and  $s_{ct}$  correspond to spatial variable  $x, y$  and time variable,  $ct$ , respectively. The frequency response of this transfer function can be obtained by setting  $s_x = j\omega_x, s_y = j\omega_y$  and  $s_{ct} = j\omega_{ct}$ , leading to

$$H(e^{j\omega_x}, e^{j\omega_y}, e^{j\omega_{ct}}) = \frac{R}{R + j\omega_xL_x + j\omega_yL_y + j\omega_{ct}L_{ct}}. \quad (2.26)$$

Note that (2.26) exhibits resonance when  $L_x\omega_x + L_y\omega_y + L_{ct}\omega_{ct} = 0$  condition is met, which leads to the passband shape of a plane in the 3-D frequency domain, normal to the vector  $(L_x, L_y, L_{ct})$ , as shown in Fig. 2.11(a-b) [18]. By cascading two such frequency planar filters, a beam-shaped passband in  $\boldsymbol{\omega}$  can be formed, due to the intersection of frequency planar passbands. For each elemental frequency planar filter, the parameter  $R > 0$  sets the selectivity of the planar passband, and  $L_x, L_y, L_{ct}$  set the orientation of the frequency plane [18]. Fig. 2.11(c) shows the beam-shaped filter passband that encompasses the plane wave spectra that need to be enhanced.

The digital counterpart of the 3-D IIR frequency planar filter of the transfer function in (2.25) can be determined by following the 3-D bi-linear transform given by  $s_k = \frac{1-z_k^{-1}}{1+z_k^{-1}}$ ,  $k \in \{x, y, ct\}$ . Following algebraic manipulations, the 3-D  $\mathbf{z}$ -transform domain transfer function of the two frequency planar filters are given by [18, 33]

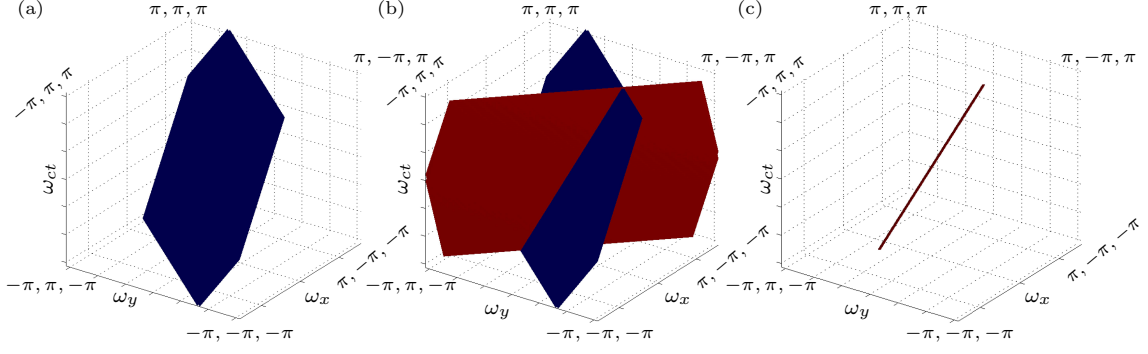


Figure 2.11: (a) Frequency response of the frequency planar filter. (b) Cascading two frequency planar filters. (c) Line-shaped passband in the  $(\omega_x, \omega_y, \omega_{ct})$  domain.

$$T_m(z_x, z_y, z_{ct}) = \frac{\sum_{i=0}^1 \sum_{j=0}^1 \sum_{k=0}^1 z_x^{-i} z_y^{-j} z_{ct}^{-k}}{\underbrace{\sum_{i=0}^1 \sum_{j=0}^1 \sum_{k=0}^1}_{i+j+k \neq 0} b_{ijk} z_x^{-i} z_y^{-j} z_{ct}^{-k}}, \quad (2.27)$$

where the subscript  $m = 1, 2$  denotes the index of the frequency planar filters (i.e. two filters in cascade), and the filter coefficients  $b_{ijk}$  are recalled here as  $b_{ijk} = \frac{R + (-1)^i L_x + (-1)^j L_y + L_{ct} (-1)^k}{R + L_x + L_y + L_{ct}}$  [33]. Each frequency planar filter given by (2.27) corresponds to an input-output recurrence relationship described by the 3-D spatio-temporal difference equation given by

$$y(n_x, n_y, n_{ct}) = \sum_{i=0}^1 \sum_{j=0}^1 \sum_{k=0}^1 w(n_x - i, n_y - j, n_{ct} - k) - \underbrace{\sum_{i=0}^1 \sum_{j=0}^1 \sum_{k=0}^1}_{i+j+k \neq 0} b_{ijk} y(n_x - i, n_y - j, n_{ct} - k). \quad (2.28)$$

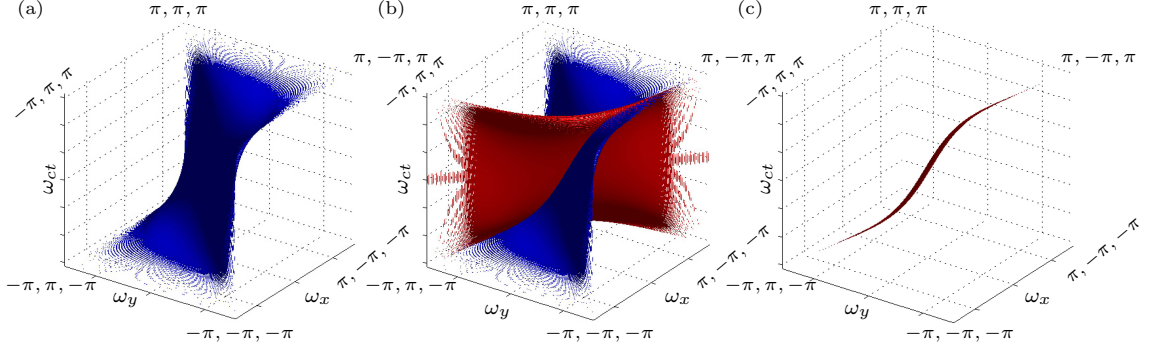


Figure 2.12: (a) Frequency response of the discrete domain frequency planar filter (b) Cascading two digital frequency planar filters (c) Obtained line/beam shaped passband in the  $(\omega_x, \omega_y, \omega_{ct})$  domain.

The complete transfer function of the 3-D IIR digital beam filter is therefore given by

$$T_{3D}(z_x, z_y, z_{ct}) = T_1(z_x, z_y, z_{ct})T_2(z_x, z_y, z_{ct}). \quad (2.29)$$

Since this transfer function does not account for the number of elements in the antenna array, it is applicable only if the array size is large enough to stabilize the impulse response of the beam filter or the array size is infinite. The frequency response function is computed by setting  $z_k = e^{j\omega_k}$ ,  $k \in \{x, y, ct\}$  in (2.29) and has a beam-shaped passband in  $\omega$  as shown in Fig. 2.12. Selection of the passband orientation parameters  $L_x, L_y, L_{ct}$  for each frequency planar filter in (2.29) depends on the DOA  $(\psi, \phi)$  of the plane wave signal to be enhanced, and can be obtained by following the algorithm presented in [34]. Because the filter coefficients  $b_{ijk}$  for each frequency planar filter can be evaluated in closed-form as functions of the beam direction (DOA)  $(\psi, \phi)$ , electronic beam steering can be achieved in real-time.

CHAPTER III  
DIRECTIONAL SPECTRUM SENSING AND CYCLOSTATIONARY FEATURE  
EXTRACTION USING 2D IIR BEAM FILTERS

Due to explosive growth in wireless communications, the electromagnetic spectrum has become increasingly congested [35]. CR solutions for increasing spectral utilization require “spectrum sensing”. Conventional sense algorithms are based on techniques such as cyclostationary feature detection, energy detection, waveform sensing, and matched filtering [36]. However, these algorithms are generally non-directional and therefore *do not* provide information about the direction of primary and secondary users (PU/SUs) [36, 37, 38]. Beamforming allows the selective enhancement of RF planar waves based on their DOA, leading to increased flexibility at MAC and network layers. However, beamforming methods such as digital phased-arrays are computationally expensive and are typically narrowband in nature. This problem is addressed by proposing low complexity spatio-temporal aperture algorithms based on MD digital recursive filters [28]. The ultimate objective of this work is to sense the primary and secondary users’ DOAs, locations, carrier frequencies, modulation/features (waveforms), polarizations, and eventually other physical parameters such as higher order (non-planar) propagation modes.

Conventional spectrum sensing methods search for white spaces mainly in three dimensions, time, frequency and geographical area of the PU. However, directional spectrum sensing methods explore a new dimension which is the DOA of the PUs, to introduce another degree of freedom to the CR systems. The dimension, DOA of the PU, is different from the geographical area. Consider a situation where both PU and SU (with highly directional communication) are located in the same geographical area with a minimum interference to each other. Spectrum sensing with only geographical area information may not allow to initiate SU communication, since they are in the same physical location. However, with the directional sensing approach, SU can communicate in directions where they have insignificant interference to the PU. This will allow multiple users to use the same frequency band to transmit their signal at the same time in the same geographical area. To gain the advantages of such methods, transmit and receive beamforming techniques need to be employed with both PU and SU for directional communication. Directional spectrum sensing methods may increase the hardware and computational implementation complexity of the complete CR system while enhancing the spectral utilization.

Depending on the direction estimation method, directional spectrum sensing can be classified into two main categories, DOA estimation algorithm based methods which employ algorithms such as multiple signal classification (MUSIC)[39], Capon and estimation of signal parameters via rotational invariance technique (ESPRIT) to estimate the PU direction and ST filtering based methods which use beamforming techniques to estimate the direction of the PU. Both methods utilize an antenna

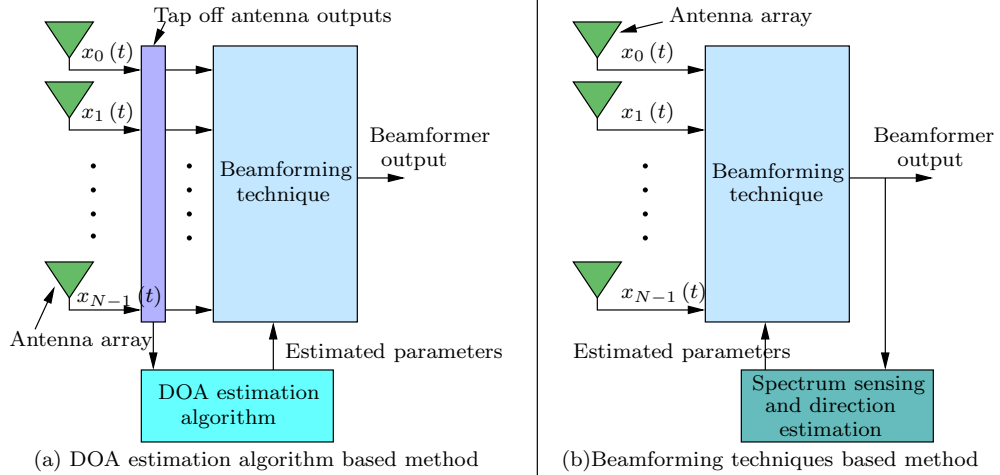


Figure 3.1: Directional spectrum sensing methods.

array based beamforming technique for directional communication. DOA estimation algorithm based methods decide the PU direction by analyzing the information at the antenna array (prior to the beamforming techniques)[40] while the beamforming based approaches estimate the DOA utilizing signals at the beamformer output as shown in 3.1 (eg: energy detection at the directionally enhanced output).

The MUSIC algorithm along with the maximum to minimum eigenvalue (MME) detector has been proposed to estimate the DOA of the PUs and the presence of the PU's [41]. Initially the algorithm checks the existence of the PU by applying MME detection to the outputs of each antenna  $w_i(n)$  where  $i \in \{0, 1, \dots, N - 1\}$  and  $N$  is the number of antennas in the array. Then if no PU is detected, SU changes its radio parameters to transmit signals in any direction. If it detects any PUs in the environment, SU continues to estimate the DOA of the PU using MUSIC al-

gorithm and forces the CR to avoid the detected directions from SU transmissions. MUSIC algorithm calculates its power spectral function which is called MUSIC spectral ( $P_{MUSIC}(\theta)$ ) using the sample covariance matrix of antenna outputs. Peaks in the  $P_{MUSIC}(\theta)$ , corresponds to the PU's DOAs. As an improvement, [42] proposed a wideband directional spectrum sensing method which uses fourth-order cumulants matrix of the received signal to sense the spectrum and to estimate DOAs of PUs. In [40, 43], existing DOA estimation methods such as MUSIC, Capon and ESPRIT are analyzed in order to show the possibility of using these methods in CR systems to increase the spectral opportunities.

In the beamforming based DOA estimation method, beamformer scans the environment and use an energy detection with the directionally enhanced output to obtain the power distribution along the environment. Peak detection algorithm can then be applied on the power distribution to estimate the DOAs of each PUs. This will result a map of the existing PUs and their DOAs. At a particular detected DOA, conventional spectrum sensing methods such as cyclostationary detection can be used to detect the occupied frequencies and modulation schemes. In the next section, a low complex, 2-D network resonant beam filter based directional spectrum sensing architecture along with their basic theory and implementation is introduced.

### 3.1 Overview of Proposed Spectrum Sensing and Feature Extraction Architecture

A combined approach using low complexity array processing based on 2-D IIR digital beam filters with cyclostationary feature extraction for sensing the DOA, frequency

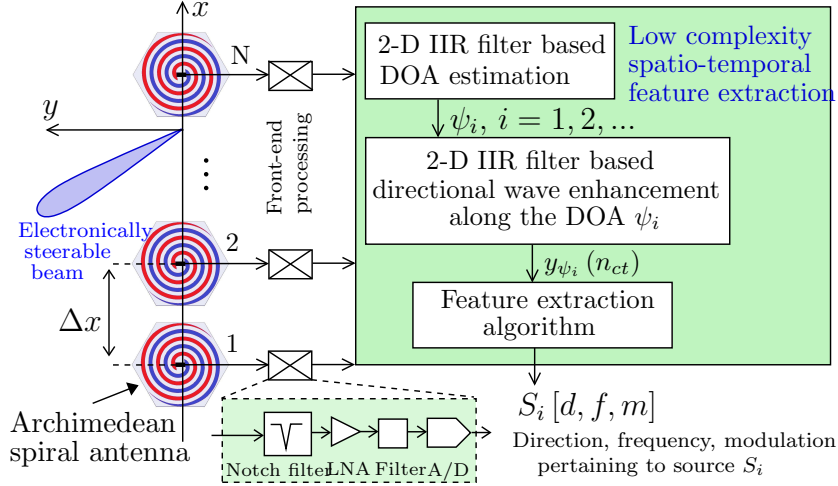


Figure 3.2: Overview of the proposed 2-D IIR digital beam filter based directional feature extraction system employing a ULA of Archimedean spiral antennas.

and modulation of radio sources in a CR environment is proposed. Towards this goal, an unobtrusive low-cost wideband Archimedean spiral antenna is also proposed for the antenna array. Let  $S_i$  denote a radio source within the CR environment, where  $i = 1, 2, \dots$ . The proposed directional feature extraction scheme can potentially be employed at the physical layer of a sensing station. The directional feature detection output for source  $S_i$  is denoted by  $S_i[d, f, m]$ , where  $d$  is the DOA,  $f$  is the RF carrier frequency and  $m$  is the modulation scheme. Fig. 3.2 shows an overview of the proposed directional feature extraction system. A ULA of  $N$  Archimedean spiral antennas are employed to spatially sample the propagating radio waves. The inter-antenna spacing is  $\Delta x = \lambda_{min}/2 = c/2F_{max}$ , where  $\lambda_{min}$ ,  $c$  and  $F_{max}$  are the shortest wave length, propagation speed and the maximum frequency of the RF signal of interest. Output of each antenna is connected to a front-end RF processing block, which typically contains a tunable notch filter to attenuate known out-of-band interference, a low

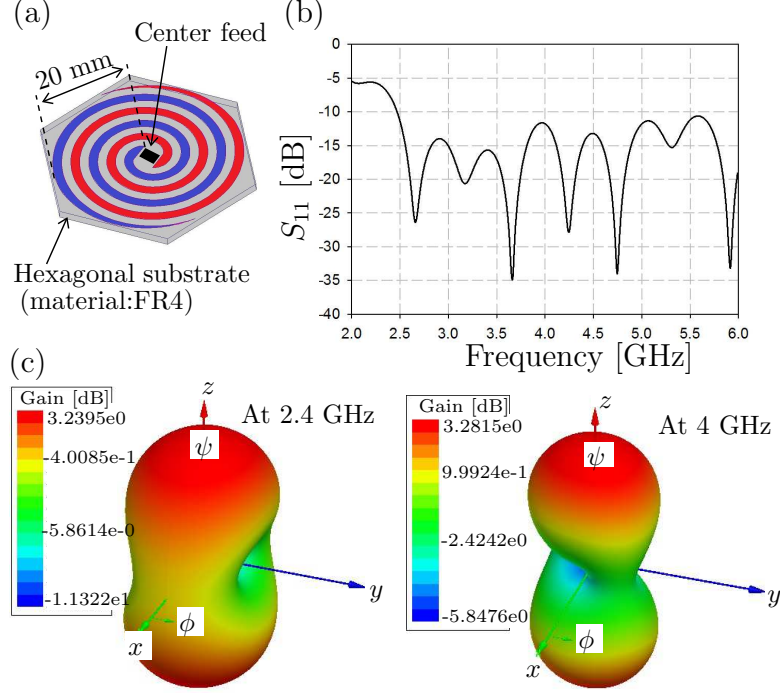


Figure 3.3: (a) Structure, (b) scattering parameter  $S_{11}$  and (c) far-field radiation pattern of the proposed Archimedean spiral antenna. Full-wave simulations are from Ansoft HFSS computational electromagnetic software.

noise amplifier (LNA), a low pass filter and an ADC. This results in a 2-D discrete domain spatio-temporal input sequence  $w(n_x, n_{ct})$ , where  $n_x = 0, 1, 2, \dots, N - 1$  is the antenna index and  $n_{ct} = 0, 1, \dots$  is the temporal sample index. The signal  $w(n_x, n_{ct})$  is processed by the proposed system to extract features pertaining to a given source  $S_i$  such as the direction, frequency and modulation scheme.

### 3.1.1 Center-Fed Archimedean Spiral Antenna

Spiral antennas are frequency independent with radiation mechanism occurring at regions where the circumference of the spiral equals an integer multiple of a wavelength [44]. Thus, for a circular spiral, the radiation bands occur when the antenna diameter

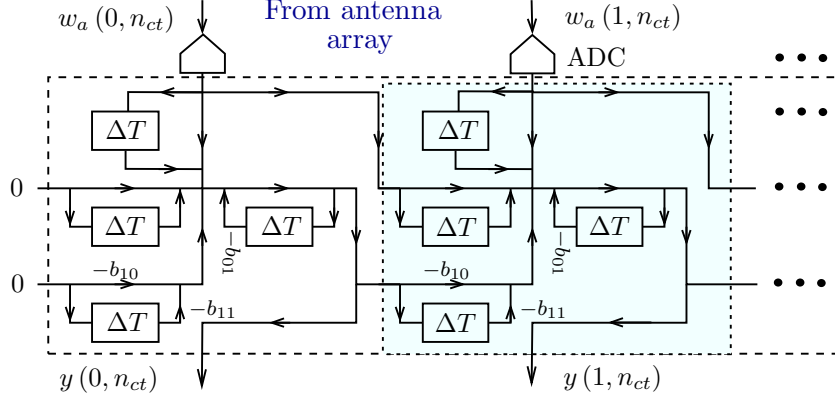


Figure 3.4: (a) Signal flow graph of the 2-D IIR beamfilter.

$D = n\lambda/\pi$ . The lowest operating frequency of the antenna is determined by the spiral outer circumference while, the highest operating frequency can be varied by adjusting the number of turns [45]. The proposed spiral antenna is shown in Fig. 3.3(a), which consists of 2.7 turns and an expansion coefficient of 1.1. This antenna was simulated using Ansoft HFSS computational electromagnetic tool for FR4 substrate with a dielectric constant of 4.4, a dielectric loss tangent of 0.02, and a thickness of 1.6 mm. The antenna has a center-feed that was simulated as a lumped port with a  $50 \Omega$  impedance. The diameter is 40 mm. Fig. 3.3(b) shows the full-wave simulated reflection coefficient ( $S_{11}$ ). The frequency performance demonstrates a broad impedance bandwidth from 2.4 GHz to 6 GHz. Fig. 3.3(c) shows the 3-D far-field radiation pattern simulated at 2.4 GHz and 4 GHz, respectively. The patterns are nearly symmetrical in the azimuthal plane as required.

### 3.1.2 DOA Estimation Employing 2-D IIR Digital Beam Filters

Recall from Chapter 2 that the network resonant 2-D IIR beam filter has the  $\mathbf{z}$  domain transfer function  $T(z_x, z_{ct})$

$$\frac{Y(z_x, z_{ct})}{W(z_x, z_{ct})} = T(z_x, z_{ct}) = \frac{(1 + z_x^{-1})(1 + z_{ct}^{-1})}{1 + b_{10}z_x^{-1} + b_{01}z_{ct}^{-1} + b_{11}z_x^{-1}z_{ct}^{-1}} \quad (3.1)$$

where its coefficients are  $b_{ij} = \frac{R+(-1)^i L_x + (-1)^j L_{ct}}{R+L_x+L_{ct}}$ ,  $L_x = \cos \theta$  and  $L_{ct} = \sin \theta$ . Here  $\theta$  and  $R$  set the angular orientation and sharpness of the passband, respectively. The  $\mathbf{z}$  domain transfer function given in (3.1) is applicable only if the array size is large enough to stabilize the impulse response of the beam filter or the array size is infinite. The 2-D difference equation corresponding to (3.1) can be expressed as

$$y(n_x, n_{ct}) = w(n_x, n_{ct}) + w(n_x - 1, n_{ct}) + w(n_x, n_{ct} - 1) - b_{01}y(n_x, n_{ct} - 1) - b_{10}y(n_x - 1, n_{ct}) - b_{11}y(n_x - 1, n_{ct} - 1) \quad (3.2)$$

where directionally enhanced output is obtained as  $y(N - 1, n_{ct})$  for a ULA with  $N$  number of antenna elements ( $0 \leq n_x \leq N - 1$ ). 2-D IIR beam filter can be implemented as a high-speed low complexity systolic array architecture and Fig. 3.4 shows the signal flow graph of the 2-D beam filter for digital realization. Zero initial conditions are defined as  $w(-1, 0) = 0$ ,  $w(0, -1) = 0$ ,  $y(0, -1) = 0$ ,  $y(-1, 0) = 0$ , and  $y(-1, -1) = 0$  to satisfy stability conditions [19]. In order to obtain an aperture size dependent  $\mathbf{z}$  domain transfer function, we rearrange (3.1) as

$$Y(z_x, z_{ct}) = P(z_{ct})W(z_x, z_{ct}) + P(z_{ct})z_x^{-1}W(z_x, z_{ct}) + Q(z_{ct})z_x^{-1}Y(z_x, z_{ct}) \quad (3.3)$$

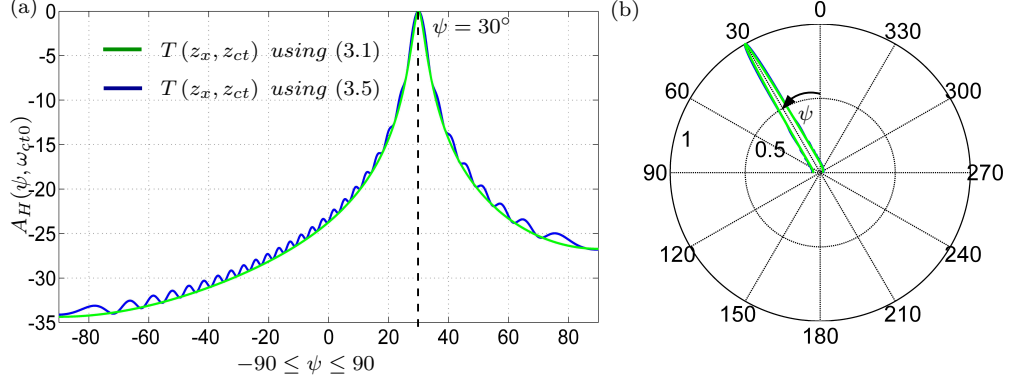


Figure 3.5: Array factor of the beam filter for beam direction  $\psi = 30^\circ$  (a) cartesian domain (b) polar domain.

where  $P(z_{ct}) = \frac{1+z_{ct}^{-1}}{1+b_{01}z_{ct}^{-1}}$  and  $Q(z_{ct}) = \frac{-(b_{10}+b_{11}z_{ct}^{-1})}{1+b_{01}z_{ct}^{-1}}$ . Application of inverse  $\mathbf{z}$  domain transform with respect to the spatial variable leads to a mixed domain input output relationship

$$Y_m(n_x, z_{ct}) = P(z_{ct})W_m(n_x, z_{ct}) + P(z_{ct})W_m(n_x - 1, z_{ct}) + Q(z_{ct})Y_m(n_x - 1, z_{ct}). \quad (3.4)$$

With the initial conditions  $W_m(-1, z_{ct}) = 0$  and  $Y_m(-1, z_{ct}) = 0$ , we can obtain following mixed domain relationships.

$$\begin{aligned} Y_m(0, z_{ct}) &= P(z_{ct})W_m(0, z_{ct}) \\ Y_m(1, z_{ct}) &= P(z_{ct})[W_m(1, z_{ct}) + W_m(0, z_{ct})R(z_{ct})] \\ Y_m(2, z_{ct}) &= P(z_{ct})[W_m(2, z_{ct}) + W_m(1, z_{ct})R(z_{ct}) + W_m(0, z_{ct})Q(z_{ct})R(z_{ct})] \\ Y_m(3, z_{ct}) &= P(z_{ct}) \left[ W_m(3, z_{ct}) + W_m(2, z_{ct})R(z_{ct}) \right. \\ &\quad \left. + W_m(1, z_{ct})Q(z_{ct})R(z_{ct}) + W_m(0, z_{ct})Q(z_{ct})^2R(z_{ct}) \right] \end{aligned}$$

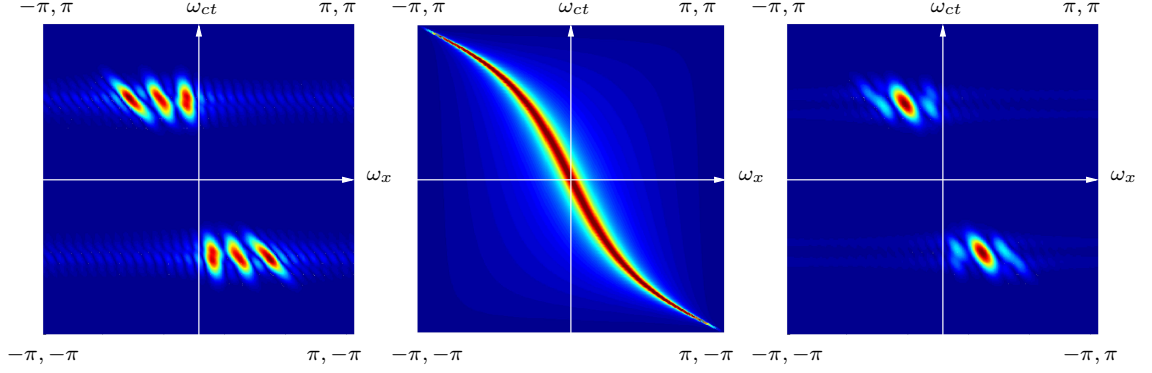


Figure 3.6: (a) 2-D Frequency spectrum of the input signal consisting with three signals from DOAs  $10^\circ$ ,  $30^\circ$  and  $60^\circ$ . (b) Frequency response of the beam filter which is tuned to filter signals from DOA  $30^\circ$ . (c) Frequency spectrum at the output of the beam filter.

$\vdots$

$$Y_m(N-1, z_{ct}) = P(z_{ct}) \left[ W_m(N-1, z_{ct}) + W_m(N-2, z_{ct}) R(z_{ct}) + W_m(N-2, z_{ct}) Q(z_{ct}) R(z_{ct}) + \dots + W_m(0, z_{ct}) Q(z_{ct})^{N-2} R(z_{ct}) \right]$$

Here  $R(z_{ct}) = 1 + Q(z_{ct})$ . Following the inverse  $\mathbf{z}$  transform, the 2-D  $\mathbf{z}$  transform domain transfer function of the  $N$  element 2-D IIR beam filter can be obtained as

$$T(z_x, z_{ct}) = \frac{Y(z_x, z_{ct})}{W(z_x, z_{ct})} = P(z_{ct}) \left[ R(z_{ct}) \sum_{k=0}^{N-2} Q(z_{ct})^k z_x^{-(k+1)} + 1 \right]. \quad (3.5)$$

The array factor produced by  $T(z_x, z_{ct})$  is obtained by evaluating the 2-D frequency response  $T(e^{j\omega_x}, e^{j\omega_{ct}})$  at a given temporal frequency  $\omega_{ct0}$  as function of the spatial angle  $\psi$  by setting  $\omega_x = -\omega_{ct0} \sin \psi$  [46]. The array factor is given by  $A_T(\psi, \omega_{ct0}) = |T(e^{-j\omega_{ct0} \sin \psi}, e^{j\omega_{ct0}})|$ . Fig. 3.5(a) shows the array factor comparison between (3.1) (does not take into the account array size) and (3.5) (accounts array size). Fig. 3.6(b) depicts the corresponding array factor in polar domain. Let the

radiation pattern of a single spiral antenna is  $A_E(\psi, \phi, \omega_{ct})$ , where  $\psi$  and  $\phi$  are the elevation and azimuth angles, respectively. The total array response at temporal frequency  $\omega_{ct0}$  is given by  $A_E(\psi, \phi_0, \omega_{ct0}) A_H(\psi, \omega_{ct0})$ , where we fix the azimuth angle at  $\phi_0$  in the 3-D antenna pattern.

Two dimensional IIR digital beam filters have been proposed for the directional wave enhancement using ULA of antennas [28]. Recall from Chapter 2 that such filters have beam shaped passbands in the 2-D spatio-temporal frequency domain  $\boldsymbol{\omega} \equiv (\omega_x, \omega_{ct}) \in \mathbb{R}^2$ , where  $\omega_k$  is the frequency variable corresponding to  $k \in \{n_x, n_{ct}\}$  [18]. Performance of the 2-D IIR beam filter in terms of the directional enhancement of wideband signals is shown in Fig. 3.6. Fig. 3.6 (a) shows the 2-D frequency spectrum of the input signal with three wideband signals from DOAs  $10^\circ, 30^\circ$  and  $60^\circ$ . 2-D IIR beam filter coefficients are calculated such that it enhances signals from DOA  $30^\circ$ . Fig. 3.6(b) and Fig. 3.6(c) show the beam shaped frequency response of the filter and the output frequency spectrum, respectively. It is clear that the beam filter is able to filter frequency content of the desired DOA. Fig. 3.7 shows the time domain results for the same simulation where interferences from  $10^\circ$  and  $60^\circ$  have been suppressed more than 14 dB and 13.5 dB at the output of the 2-D IIR beam filter, respectively.

Similar results can also be obtained using conventional wideband beamformers such as FFT based phase rotation that we discussed in Chapter 2. The motivation behind the use of recently proposed 2-D IIR beam filter instead of the conventional methods to directionally enhance the signals is the the low hardware complexity of

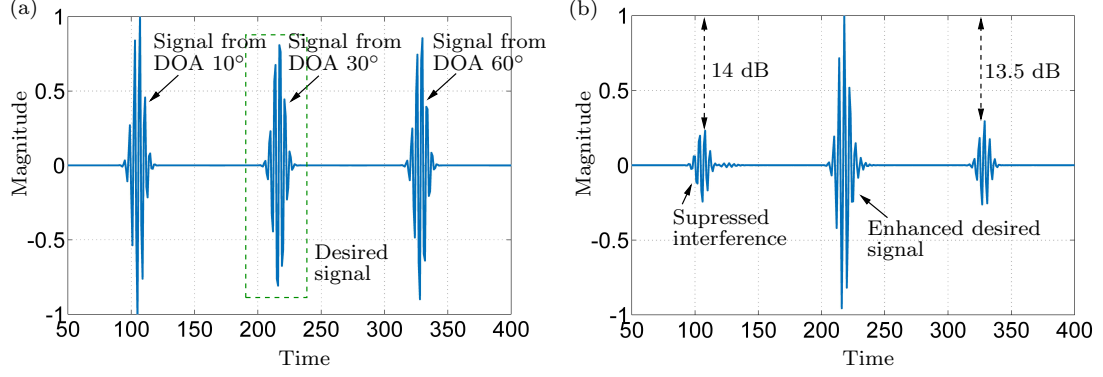


Figure 3.7: (a)Time domain representation of the three signals from DOAs  $10^\circ$ ,  $30^\circ$  and  $60^\circ$ .(b) Output at the beam filter which enhance the signal from  $30^\circ$ .

the beam filter. Consider the hardware complexity for single antenna. 512-point FFT based phase rotation requires  $\frac{3}{2}512 \log_2 512 = 6912$  real multipliers for the FFT calculations and  $512 \times 3$  real multipliers for the phase rotation where as 2-D IIR beam filter requires only 3 real multipliers per antenna. Thus the proposed beam enhanced spate-time beam filter realization only utilize  $< 0.5\%$  of the hardware that the conventional method is using to gain the same performance.

The DOA estimation block shown in Fig. 3.2, scans the CR environment by producing an electronically steered beam using a 2-D IIR digital beam filter. For each beam direction  $\psi \in [0, \pi/2]$ , the energy of the directionally enhanced output  $y_\psi(n_{ct})$  is computed, leading to a spatial energy distribution function  $E(\psi)$ . For each RF source (and reflection thereof),  $E(\psi)$  contains a local maxima, which is found by employing a peak detection on  $E(\psi)$ . The output of the DOA estimation block is therefore a set of directions  $\psi_i, i = 1, 2, \dots$

### 3.1.3 Cyclostationary Feature Extraction Algorithm

Cyclostationary feature extraction has been proposed for spectrum sensing in CR systems [36]. Processes with periodic first order statistics (such as mean and autocorrelation) are called cyclostationary where the resulting periodicity is termed as second order periodicity. Typically, modulated signals and vibration noise produced by rotating machines can be considered as examples for the practical cyclostationary processes. Consider a cyclostationary process  $x(t)$  with the statistics:

$$M_x(t + T_0) = M_x(t)$$

$$R_x(t + T_0, \tau) = R_x(t, \tau)$$

where  $R_x(t, \tau) = E\{x(t + \tau/2)x^*(t - \tau/2)\}$  is the autocorrelation of process  $x(t)$  with time difference  $\tau$ ,  $M_x(t)$  is the mean of the process  $x(t)$  at time  $t$ ,  $T_0$  is the period of the periodicity. Features embedded in cyclostationary signals such as modulation scheme, carrier frequency can be exploited by analyzing the spectral correlation function (SCF) which can be obtained using the cyclic autocorrelation function (CAF). CAF can be considered as the fundamental parameter of the second-order periodicity. If the autocorrelation of the process is periodic with  $T_0$ , it has its own fundamental frequency, called as the cycle frequency ( $\alpha$ ), which is obtained by  $\alpha = \frac{m}{T_0}$ , where  $m$  is an integer. Autocorrelation,  $R_x(t, \tau)$ , of the process  $x(t)$  can be expressed using the Fourier series as follows[47],

$$R_x(t, \tau) = \sum_{\alpha} R_x^{\alpha} e^{j2\pi\alpha t} \tag{3.6}$$

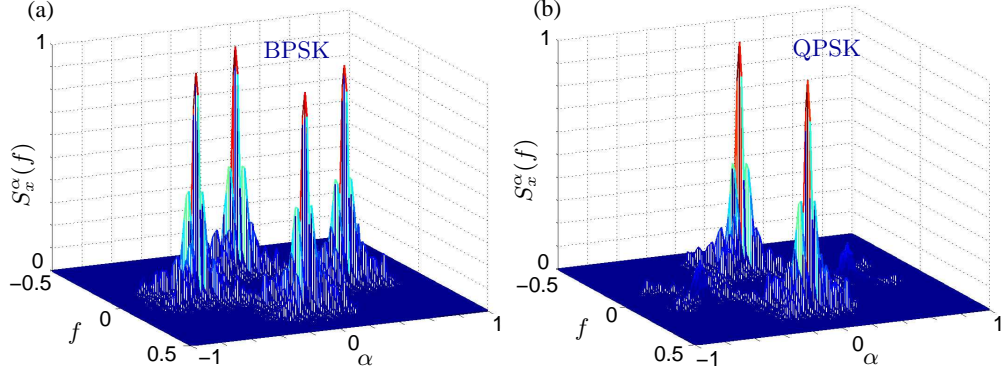


Figure 3.8: Spectral correlation function for (a) BPSK modulated and (b) QPSK modulated signals for zero noise environment.

where  $R_x^\alpha(\tau)$  is the CAF with cycle frequency  $\alpha$ , which can be expressed as

$$R_x^\alpha(\tau) = \lim_{T \rightarrow \infty} \frac{1}{T} \int_{-T/2}^{T/2} R_x(t, \tau) e^{-j2\pi\alpha t} dt. \quad (3.7)$$

CAF provides the basic autocorrelation function of the signal, if the cycle frequency is equal to 0 (i. e.  $\alpha = 0$ ). According to the cycle Wiener relation, the SCF can be obtained by taking the Fourier transform of the CAF,

$$S_x(f, \alpha) = \int_{-\infty}^{+\infty} R_x^\alpha(\tau) e^{-j2\pi f t} dt \quad (3.8)$$

SCF shows unique signatures for different modulation techniques and even for different orders of the same modulation technique as well. Fig. 3.8(a-b) shows the SCF for binary phase-shift keying (BPSK), quadrature phase shift keying (QPSK), which provides different peak profiles for each modulation scheme and will lead to automatic classification of the modulation scheme. Due to the symmetric nature of the higher-order quadrature amplitude modulation (QAM), SCF provides the same signature as QPSK. Thus, a different classifier is required to differentiate higher-order QAM.

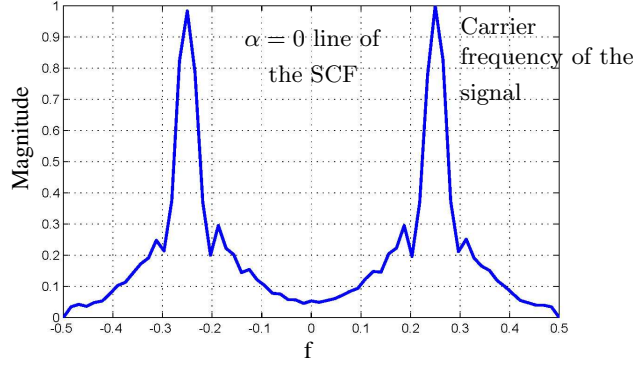


Figure 3.9:  $\alpha = 0$  line of the SCF function which is equivalent to the PSD of the input signal.

Furthermore, it can be shown that the  $\alpha = 0$  line of the SCF, corresponds to the power spectral density (PSD) function of the received signal as shown in Fig. 3.9. This can be used to locate the carrier frequency of the received signal.

Characteristics of the SCF under a noisy environment provide more advantages when the method applies in a very low SNR environment. Since additive AWGN is a stationary process, there is no spectral correlation between the cyclostationary signal and the AWGN. This will lead to obtain better detection capability for modulation detection, in low SNR environments. Since  $\alpha = 0$  corresponds to the PSD of the received signal, effect of noise can only be seen along the  $\alpha = 0$  line and preserve required information outside the  $\alpha = 0$  line to detect the modulation. This emphasizes the selection of cyclostationary based feature detection method for our proposed architecture.

---

**Algorithm 1** Spatio-temporal directional feature extraction

---

**Require:** 2-D spatio-temporal ULA input signal  $w(n_x, n_{ct})$ .

**Ensure:** Direction (d), frequency (f), modulation (m)

**Step 1:** Estimate the DOAs using steerable 2-D IIR beam filter to obtain direction estimates  $\psi_i, i = 1, 2, \dots$

**Step 2:** For each estimated DOA  $\psi_i$ , compute the directionally enhanced output  $y_{\psi_i}(n_{ct})$ .

**Step 3:** Compute the SCF  $S_{\psi_i}(\alpha, f)$  using (3.8).

**Step 4:** Estimate the frequency  $f_i$  in each direction using  $S_{\psi_i}(0, f)$ .

**Step 5:** For each  $\psi_i$ , compute the corrected source direction  $\psi'_i$  using (2.17), where  $\omega_{ct0} = 2\pi f_i/c$ .

**Step 6:** Examine unique signatures of  $S_{\psi_i}(\alpha, f)$  to decide the modulation scheme in each direction  $\psi_i$

---

By using the unique signatures in the SCF  $S_{\psi_i}(\alpha, f)$ , the frequency and modulation pertaining to each direction  $\psi_i$  is estimated. The complete directional feature extraction process corresponding to Fig. 3.2 can be summarized by Algorithm 2.

### 3.2 Simulated Directional Feature Extraction

Three simulation scenarios are considered to illustrate the directional feature extraction scheme described by Algorithm 2. Three carrier frequencies 2.4, 3 and 4 GHz that correspond to normalized temporal frequencies  $f_1 = 0.22$ ,  $f_2 = 0.27$  and  $f_3 = 0.36$ , where  $0 \leq f_i \leq 0.5$ , are considered assuming the maximum frequency

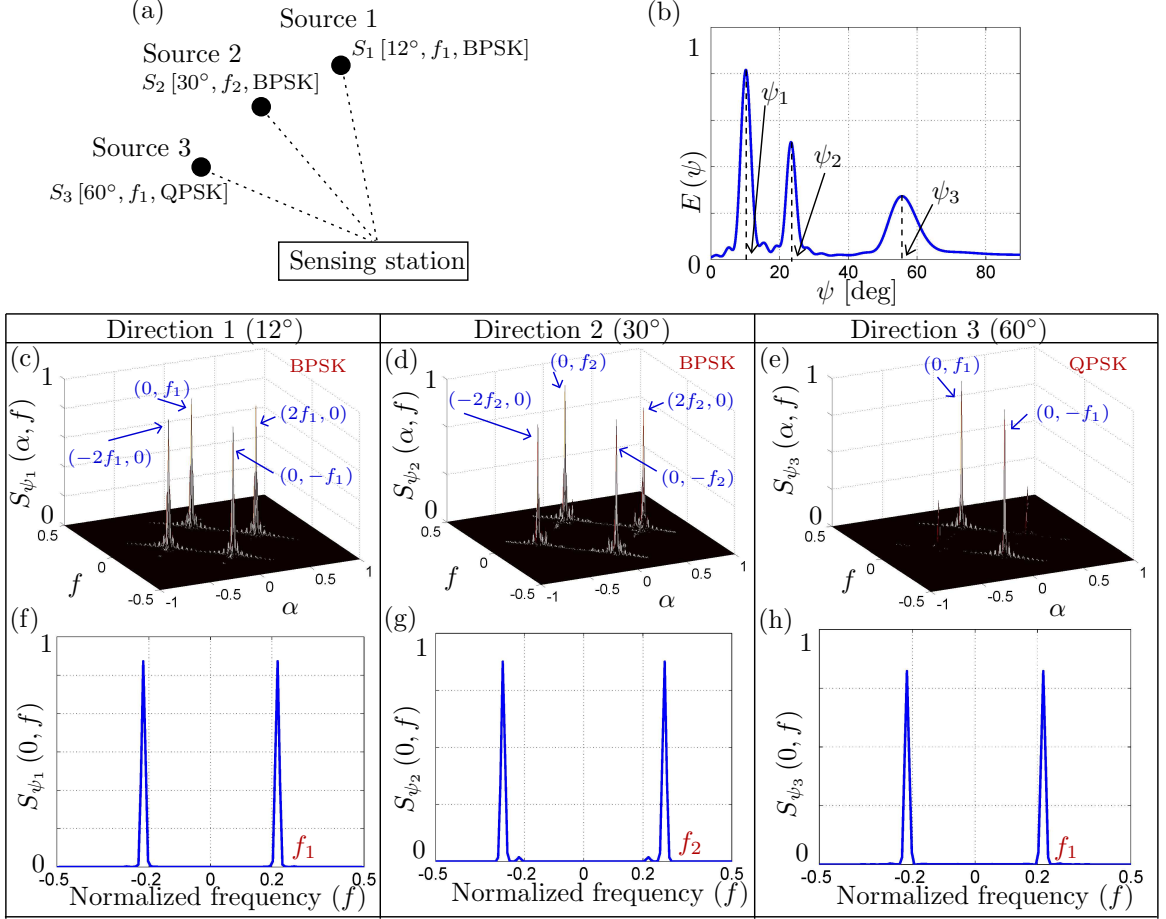


Figure 3.10: (a) Source distribution, (b) spatial energy distribution  $E(\psi)$  and (c)-(h) various feature detection outputs corresponding to the simulation scenario 1.

of  $F_{max} = 5.5$  GHz. Two modulation schemes, binary phase shift keying (BPSK) and quadrature phase shift keying (QPSK) are utilized for simulations with signal to noise ratio (SNR) of 6 dB and a ULA of 64 spiral antennas.

**Scenario 1:** Consider three RF sources  $S_i$ ,  $i = 1, 2, 3$  as in Fig. 3.10(a), where sources  $S_1$  and  $S_2$  have the same modulation type, BPSK, and occupy two different carrier frequencies 2.4 GHz and 3 GHz. Sources  $S_1$  and  $S_3$  have the same channel

Table 3.1: Source direction estimation

Source	$S_1$	$S_2$	$S_3$
Actual angle ( $\psi_i$ ) [Deg]	12	30	60
Estimated angle [Deg]	12.11	30.10	60.17

frequency 2.4 GHz, and different modulation types. Fig. 3.10(b) shows the spatial energy distribution  $E(\psi)$  obtained from step 1 in Algorithm 2, leading to three DOAs  $\psi_i$ ,  $i = 1, 2, 3$ . As given by (2.17), the actual source directions  $\psi'_i$  have to be obtained from  $\psi_i$ , after the carrier frequencies are estimated using the SCF. Then the SCF  $S_{\psi_i}(\alpha, f)$  for each DOA  $\psi_i$ ,  $i = 1, 2, 3$  is computed as shown in Fig. 3.10(c)-(e). Fig. 3.10(f)-(h) show the corresponding  $S_{\psi_i}(0, f)$  for each DOA, from which the carrier frequency pertaining to each DOA can be found (step 4), since  $\alpha = 0$  line represent the PSD of the signal. As step 5, the source directions  $\psi'_i$  are computed using (2.17) and table 3.1 lists the actual and estimated source directions for each source  $S_i$ ,  $i = 1, 2, 3$ . As shown in Fig. 3.10(c) and (e) the modulation schemes BPSK (of  $S_1$ ) and QPSK (of  $S_3$ ) can be resolved based on their different peak profiles in the SCF. For  $S_1$  and  $S_2$ , we have the same SCF peak profiles as shown in Fig. 3.10(c) and (d). However, these peaks occur at distinct points in the  $(\alpha, f)$  plane due to different carrier frequencies.

Next, we consider how the directional feature extraction can be used to reduce detection space in a multipath environment.

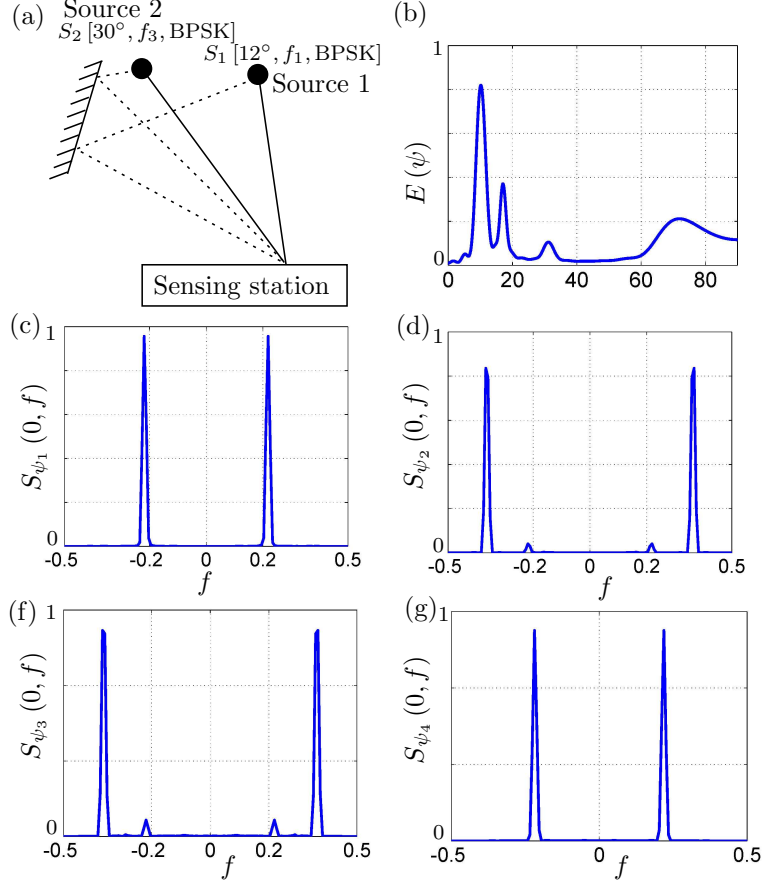


Figure 3.11: (a) Source distribution, (b) spatial energy distribution  $E(\psi)$  and (c)-(f) SCF at  $\alpha = 0$  corresponding to simulation scenario 2.

**Scenario 2:** As shown in Fig. 3.11(a), two sources  $S_1, S_2$  with same modulation and different carrier frequencies are considered, where one is a reflection of other. The energy distribution shown in Fig. 3.11(b) implies four DOAs, two of which are in fact due to reflections. With apriori knowledge on the number of sources within the domain of interest (in this case two), one can reduce the detection space by exploiting the SCF for each direction. However, additional parameters such as signal strength has to be employed to differentiate the direct and the reflected wave. Since both sources use the same modulation, frequency is the differentiation factor and can be

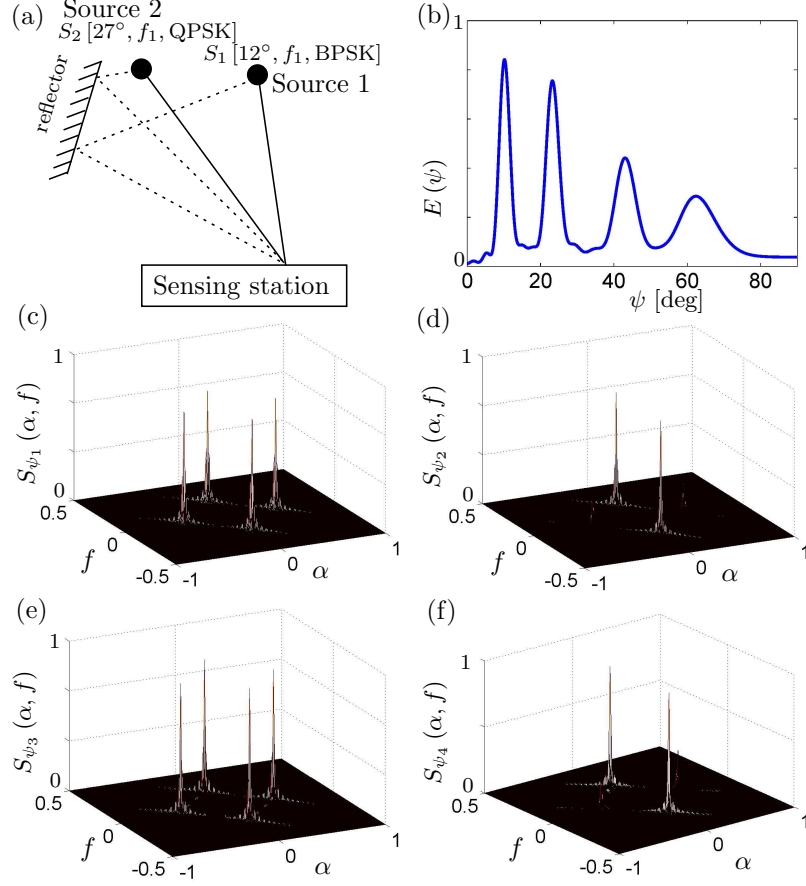


Figure 3.12: (a) Source distribution, (b) spatial energy distribution  $E(\psi)$  and (c)-(f) SCF for different DOAs corresponding to simulation scenario 3.

extracted by SCF when  $\alpha = 0$  ( $S_{\psi_i}(0, f)$ ) as shown in Fig. 3.11(c)-(g).  $S_{\psi_1}(0, f)$  and  $S_{\psi_4}(0, f)$  correspond to the same frequency and therefore we can assume that the two directions correspond to the direct and reflected paths of the same source.

**Scenario 3:** As shown in Fig. 3.12(a), two sources  $S_1$  and  $S_2$  with different modulations and same carrier frequency are considered. The energy distribution in Fig. 3.12(b) implies four source directions, where two of them are due to reflections. Fig. 3.12(c)-(f) show the SCF for the four directions. We obtain two pairs of identi-

cal peak profiles, from which the detection space can be halved when considering the identical SCFs to be corresponding to the source  $S_i$  and its reflection.

### 3.3 Conclusions

A combined approach of low complexity antenna array signal processing and cyclostationary feature extraction is proposed for spatio-temporal directional feature detection in a CR environment. An Archimedean spiral antenna operating in the frequency range 2-6 GHz is proposed and is used in a linear array configuration to spatially sample the radio waves. 2-D IIR digital beam filters are proposed for the directional radio wave enhancement. Simulated examples are discussed, where spatio-temporal features such as direction, frequency and modulation of radio sources are estimated, which in turn can be used to derive high level network protocols towards achieving enhanced access to radio spectrum.

## CHAPTER IV

### DIRECTION/LOCATION ESTIMATION AND MODULATION DETECTION FOR RF SOURCES USING STEERABLE 3-D IIR DIGITAL BEAM FILTERS

In this chapter, the application of rectangular antenna array based 3-D IIR beam filter to estimate the directional, location, and modulation information pertaining to radio sources in a CR environment is discussed. Consider a propagating far field radio wave denoted by  $w(x, y, z, ct)$ , where  $x, y, z$  represent the 3-D Cartesian space and  $ct$  is time  $t$  normalized by the wave propagation speed  $c$ . Conventional RF-to-bits direct conversion single antenna receivers lead to a 1-D temporal signal of the form  $w(n_{ct}) = w(0, 0, 0, c\Delta T n_{ct})$ , where  $\Delta T$  is the sampling period of the ADC, and subsequently performs 1-D sensing on  $w(n_{ct})$  in the time-frequency domain. However, receivers equipped with a planar array of antennas on the  $x - y$  plane can extract both spatial and temporal variations of the radio waves leading to a 3-D spatio-temporal signal of the form  $w(n_x, n_y, n_{ct}) = w_p(\Delta x n_x, \Delta y n_y, 0, c\Delta T n_{ct})$ , where  $\Delta x$  and  $\Delta y$  are the inter antenna spacing. Here,  $n_x, n_y$  are the antenna indexes and  $n_{ct}$  is the time sample index. Such 3-D spatio-temporal signals can be processed at the physical layer to extract additional information pertaining to radio sources such as direction, location, and modulation type which can potentially be exploited to

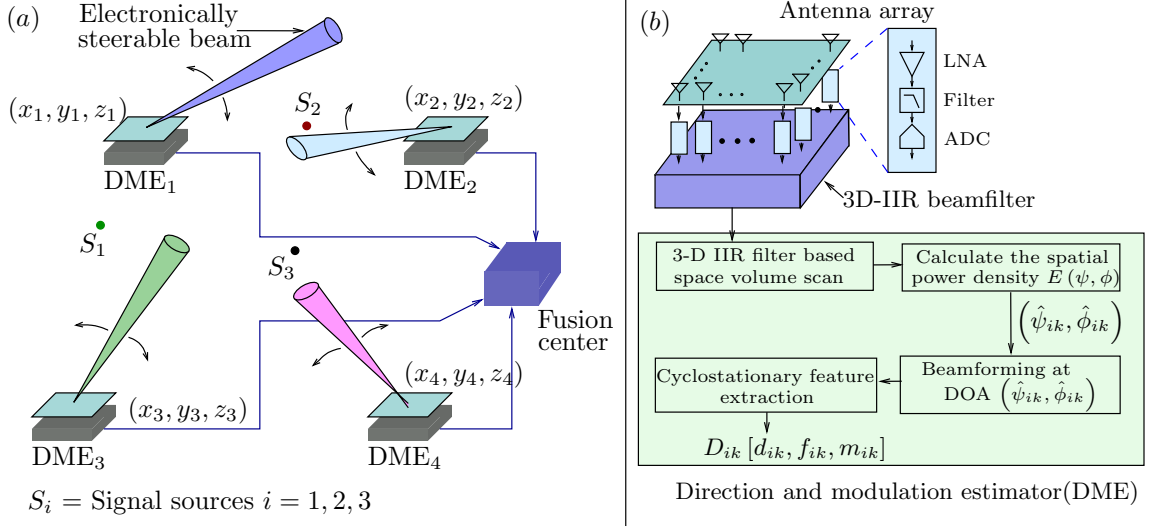


Figure 4.1: (a) Overview of the proposed 3-D IIR beam filter based feature detection scheme with multiple DMS stations. (b) Overview of a DME station which is realized using a planar antenna array and 3-D IIR digital filter.

optimize higher layer protocols that deal with signal routing and resource allocation in order to achieve better utilization of radio spectrum.

#### 4.1 Overview of the Proposed Architecture

Fig. 4.1 shows an overview of the proposed system that employs multiple direction and modulation estimator (DME) stations and a fusion center. Each DME station is equipped with a planar array of broadband antennas and an array processing module based on 3-D IIR digital beam filters. 3-D IIR filters are employed as a low complexity alternative to digital phased arrays to perform highly directional spatio-temporal filtering of radio waves (i.e. beamforming) [48, 49]. We assume an RF-to-bits type direct conversion at each DME station leading to a 3-D spatio-temporal sequence

$w(n_x, n_y, n_{ct})$ . Each DME station performs a highly directional volume scan of the CR environment using a 3-D IIR digital filter, which produces electronically steerable beams via closed-form design equations [34].

Directionally enhanced output of the 3-D IIR filter  $y_{(\psi\phi)}(n_{ct})$  is then integrated and averaged over time to obtain a spatial power distribution  $E(\psi, \phi)$ , where  $\psi$  is the azimuth angle and  $\phi$  is the elevation angle with respect to the array surface. Peaks in the power profile can be used to estimate the directions  $(\hat{\psi}_k, \hat{\phi}_k)$  of each signal sources  $S_k$ , where  $k = 1, 2, \dots$ . Following the direction estimation, the 3-D IIR filter is tuned to each source direction to obtain the beamformed output along each source direction, which is then employed to compute the SCF pertaining to each estimated source. SCF is the decision statistic of the cyclostationary feature extraction process, which in turn, provides the frequency and modulation information about the signal source. In the proposed architecture shown in Fig. 4.1, four DME stations  $DME_i$  are located at the coordinates  $(x_i, y_i, z_i)$ , where  $i = 1, 2, 3, 4$ . Output of each DME station is denoted by the data set  $D_{ik} [\hat{d}_{ik}, \hat{f}_{0ik}, \hat{m}_{ik}]$ , where  $\hat{d}_{ik}, \hat{f}_{0ik}, \hat{m}_{ik}$  denote direction, frequency, and modulation estimations, respectively. Here, the subscript  $i$  is the DME station number and  $k$  is the index of the sources detected at DME station  $i$ . The fusion center receives  $D_{ik} [\hat{d}_{ik}, \hat{f}_{0ik}, \hat{m}_{ik}]$  for  $i = 1, 2, 3, 4$  and  $k = 1, 2, \dots$  and analyses this information to estimate the location of each source.

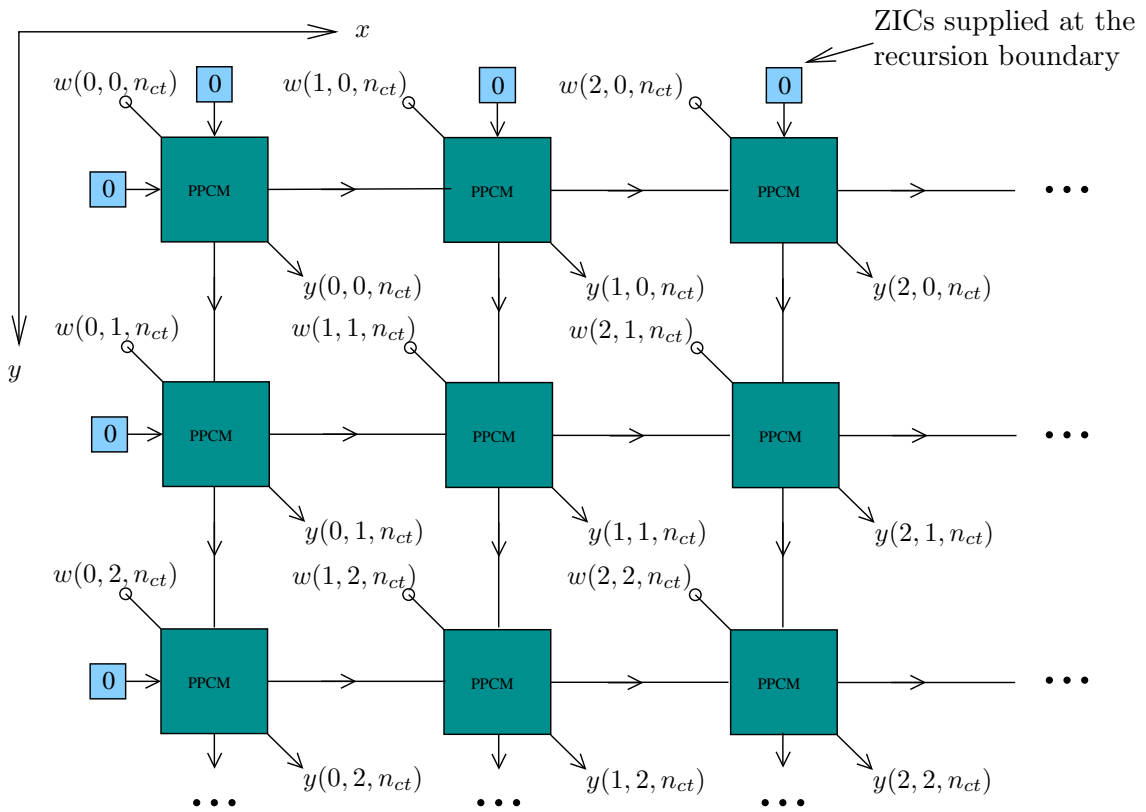
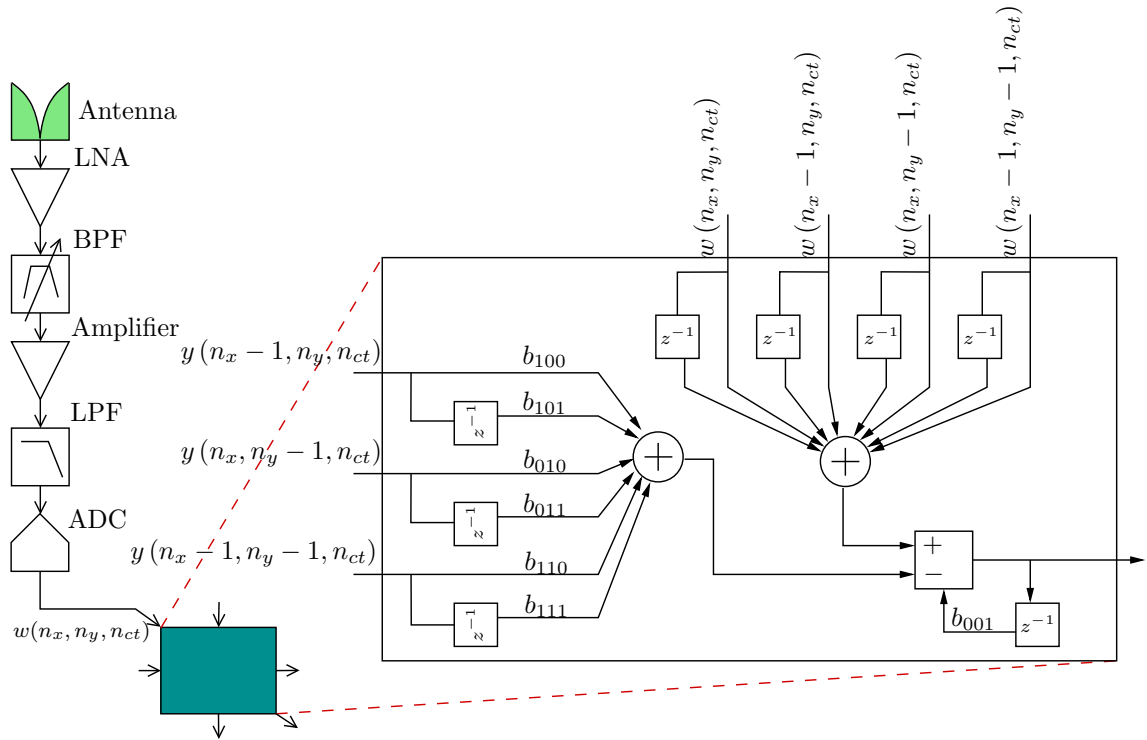


Figure 4.2: Signal Flow graph of the frequency planar filter correspond to  $\mathbf{z}$  domain transfer function  $H_m(z_x, z_y, z_{ct})$ .

#### 4.1.1 Direction Estimation Employing Electronically Steerable 3-D IIR Beam Filters

Recall from the Chapter 2 that 3-D IIR beam filters which are designed using the concept of multi-dimensional passive network resonance, have a beam shaped passband in  $\boldsymbol{\omega} \equiv (\omega_x, \omega_y, \omega_{ct})$  3-D frequency domain. Two frequency planar filters described by its  $\mathbf{z}$  domain transfer function  $H_m$

$$H_m(z_x, z_y, z_{ct}) = \frac{\sum_{i=0}^1 \sum_{j=0}^1 \sum_{k=0}^1 z_x^{-i} z_y^{-j} z_{ct}^{-k}}{\underbrace{\sum_{i=0}^1 \sum_{j=0}^1 \sum_{k=0}^1 b_{ijk} z_x^{-i} z_y^{-j} z_{ct}^{-k}}_{i+j+k \neq 0}}, \quad (4.1)$$

where  $m = 1, 2$  and filter coefficients  $b_{ijk} = \frac{R+(-1)^i L_x + (-1)^j L_y + L_{ct}(-1)^k}{R+L_x+L_y+L_{ct}}$ , can be cascaded to obtain the beam shaped passband. Angular orientation of the beam is controlled using the values  $L_x, L_y$  and  $L_{ct}$  while adjusting the passband through the value  $R$ . Since (4.1) does not depend on the antenna array size (number of antenna elements), the transfer function is applicable only if the array size is large enough to stabilize the impulse response of the beam filter or the array size is infinite. Closed form representation of the filter coefficients leads to steer the beam direction and can be obtained by following the algorithm presented in [34]. Multiple input multiple output relationship corresponds to (4.1) of the frequency planar filter is

$$y(n_x, n_y, n_{ct}) = \sum_{i=0}^1 \sum_{j=0}^1 \sum_{k=0}^1 w(n_x - i, n_y - j, n_{ct} - k) - \underbrace{\sum_{i=0}^1 \sum_{j=0}^1 \sum_{k=0}^1 b_{ijk} y(n_x - i, n_y - j, n_{ct} - k)}_{i+j+k \neq 0}. \quad (4.2)$$

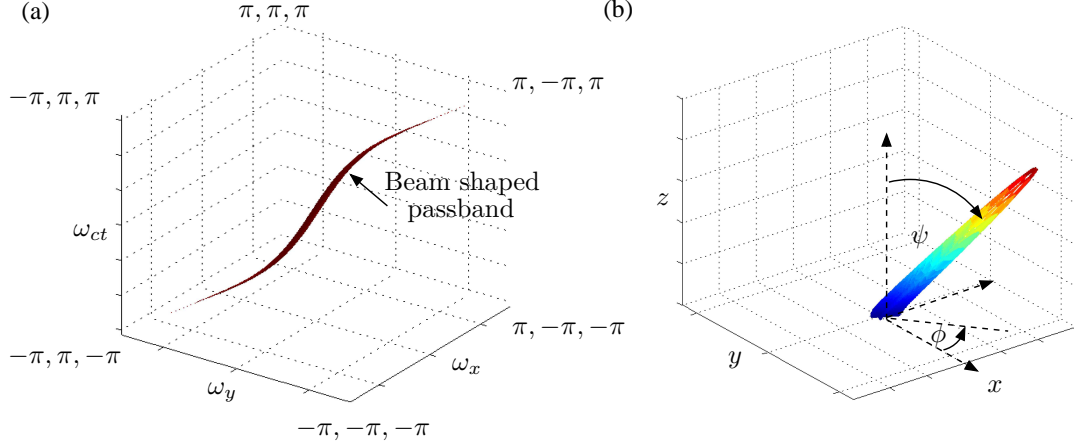


Figure 4.3: (a) Beam shaped passband, (b) array factor, of the 3-D filter for beam direction  $\psi = 30^\circ$  and  $\phi = 290^\circ$ .

Signal flow graph of the frequency planar filter is shown in Fig. 4.2 for a massively parallel systolic array architecture which can be realized in a digital signal processor. Fig. 4.3(a) exhibits the beam shaped passband in  $\omega$  for  $\psi = 30^\circ$  and  $\phi = 290^\circ$  which is obtained by cascading two such systems. The array factor produced by  $H_m(z_x, z_y, z_{ct})$  is obtained by evaluating the 3-D frequency response  $H(e^{j\omega_x}, e^{j\omega_y}, e^{j\omega_{ct}})$  at a given temporal frequency  $\omega_{ct0}$  as function of the elevation angle  $\psi$  and azimuth angle  $\phi$  by setting  $\omega_x = \omega_{ct0} \sin \psi \cos \phi$  and  $\omega_y = \omega_{ct0} \sin \psi \sin \phi$  where  $\sin \phi = \tan \theta$  [46]. The array factor is given by  $A_H(\psi, \phi, \omega_{ct0}) = |H(e^{j\omega_{ct0} \sin \psi \cos \phi}, e^{j\omega_{ct0} \sin \psi \sin \phi}, e^{j\omega_{ct0}})|$ . Fig. 4.3(b) shows the array factor corresponds to the beam response in Fig. 4.3(a) for a rectangular array with antenna elements. Note that the antenna array size has not been used for the calculation of the beam response or the array factor.

3-D frequency spectrum for three wideband signals from DOAs  $(30^\circ, 50^\circ)$ ,  $(40^\circ, 120^\circ)$ , and  $(20^\circ, 250^\circ)$  is shown in Fig. 4.3(a). 3-D IIR beam filter beam direction is designed to be at  $(40^\circ, 120^\circ)$ . Since the ROS of the plane wave coming from a DOA  $(\psi, \phi)$  is confined to straight line in the  $(\omega_x, \omega_y, \omega_{ct}) \in \mathbb{R}^3$  3-D frequency domain which is passing through the origin, has an angle  $\theta$  to the  $\omega_{ct}$  axis and an angle  $\phi$  to  $\omega_x$  axis, 3-D IIR beam filter can be designed such that its passband aligns with the desired spectrum. Fig. 4.3(b) and Fig. 4.3(c) show the frequency response of the filter and the spectrum at the output of the filter, respectively. Time domain input and output of the simulation are shown in Fig. 4.5(a-b) where interference from  $(30^\circ, 50^\circ)$  has been suppressed 33 dB and interference from  $(20^\circ, 250^\circ)$  has been suppressed 14 dB at the output of the 3-D IIR beam filter.

3-D IIR beam filter of the proposed method can be replaced using the FFT based STAP beamformer (consider 512-point FFT architecture), which is discussed in Chapter 2, while preserving the performance of the system. 512-point FFT based STAP beamformer requires  $\frac{3}{2}512 \log_2 512 = 6912$  real multipliers for the FFT calculations and  $512 \times 3$  real multipliers for the phase rotation where as 3-D IIR beam filter requires only 14 real multipliers per antenna.

Each DME station shown in Fig. 4.1(a) computes the average received signal power along the direction  $(\psi, \phi)$  using the directionally enhanced output of the 3-D IIR beam filter  $y_{\psi, \phi}(n_{ct})$ . By performing a volume scan (via electronic beam steering of the 3-D IIR beam filter) for  $0 \leq \psi \leq \pi/2$  and  $0 \leq \phi \leq 2\pi$ , a spatial power profile is obtained as  $E(\psi, \phi)$ . Local maxima of  $E(\psi, \phi)$  corresponds to the direction estimates

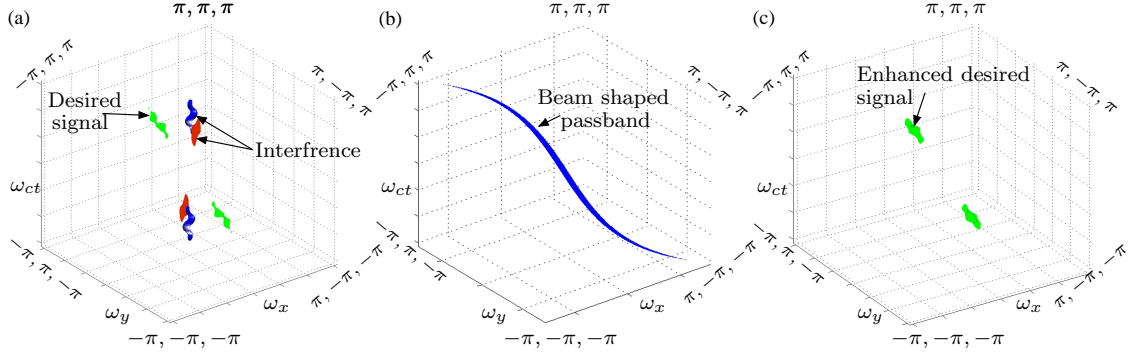


Figure 4.4: 3-D frequency spectrum of the input signal, (b) frequency response of the filter, (c) output frequency spectrum.

pertaining to the RF sources and their reflections. A peak detection algorithm is applied to  $E(\psi, \phi)$  at each DME station to obtain the DOA estimates  $(\hat{\psi}_k, \hat{\phi}_k)$  for  $k = 1, 2, \dots$ . In the proposed architecture, we employ four DME stations located at different points in space and each DME station for  $i = 1, 2, 3, 4$  outputs the estimated directions  $d_{ik} = (\hat{\psi}_{ik}, \hat{\phi}_{ik})$  of the RF sources, where  $k = 1, 2, \dots$  is the index of the RF source being estimated by the DME station  $i$ .

#### 4.1.2 Modulation Scheme Detection

Modulation type of the detected signal source  $S_{ik}$  is estimated by analyzing the cyclostationary features of directionally enhanced output  $y_{\psi_{ik}, \phi_{ik}}(n_{ct})$ . SCF shows unique signatures for different modulation techniques and for different orders of the same modulation technique as well. As an example, SCF for BPSK and QPSK provide different peak profiles in the SCF as discussed in the Chapter 3. Furthermore, it can be shown that the  $\alpha = 0$  line of the SCF corresponds to the PSD function of the received signal leads to locate the received signal carrier frequency.

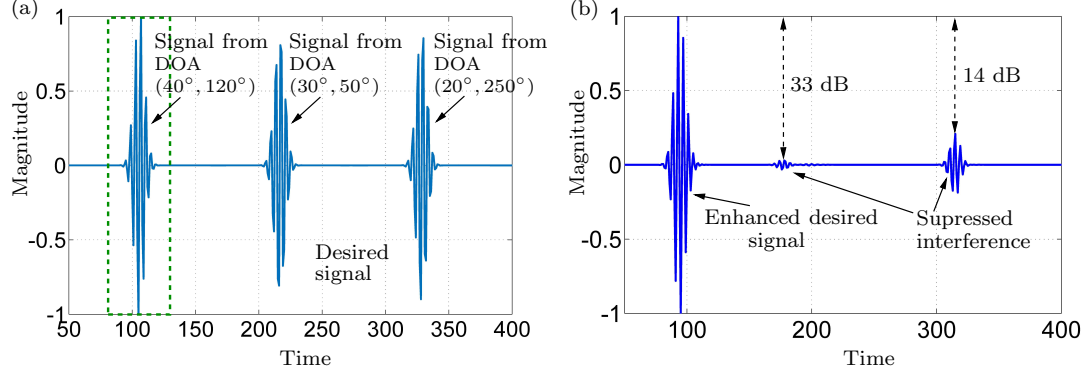


Figure 4.5: (a) Time domain representation of the three signals from DOAs  $(30^\circ, 50^\circ)$ ,  $(40^\circ, 120^\circ)$ , and  $(10^\circ, 270^\circ)$ . (b) Output at the beam filter which enhance the signal from  $30^\circ$ .

SCF of each detected signal sources are calculated at each  $DME_i$  and compared with predefined signature dictionary to identify the modulation type  $m_{ik}$ . Carrier frequency  $f_{ik}$  of each source is then estimated by evaluating the SCF at  $\alpha = 0$ . Output of the modulation type detection system would be the modulation scheme  $\hat{m}_{ik}$  and carrier frequency  $\hat{f}_{ik}$  corresponding to each signal source  $S_k$ . Each DME station provides the information set  $D_{ik} = [\hat{d}_{ik}, \hat{f}_{ik}, \hat{m}_{ik}]$  as shown in Fig. 4.1. Estimated information from the DME stations are then processed by the fusion center to estimate location of each signal source.

#### 4.1.3 RF Source Location Estimation

The fusion center can analyze received data from each  $DME_i$  where  $i \in \{1, 2, 3, 4\}$  and utilize their coordinates  $(x_i, y_i, z_i)$  to obtain the correct location of the sources  $S_k$ . If each  $DME_i$  detect only one signal source in the environment, fusion center can easily locate the source by solving trigonometric equations, without analyzing the

modulation type and carrier frequency information from the DMEs. Once we find the DOA of a particular source with respect to each DME station, we can write three independent equations as all of three lines should pass-through the same coordinates of the source  $S_k$  location,  $(x_k, y_k, z_k)$ ,

$$\frac{x_k - x_i}{\sin \psi_i \cos \phi_i} = \frac{y_k - y_i}{\sin \psi_i \sin \phi_i} = \frac{z_k}{\cos \psi_i} \quad (4.3)$$

Then the linear equation system can be solved to estimate the coordinates of the source  $S_k$ . Here we use a fourth station to resolve the ambiguities due to reflections and shadowing effects in a practical environment.

If the environment consists of more than one source, fusion center may use modulation type or carrier frequency information to differentiate the sources from each other. Fusion center can group the information sets as the same modulation type and carrier frequency before applying in to the equations. As an example, if the environment consists of two sources with two different modulation schemes (as shown in the simulations), fusion center can group the measurement sets according to the modulation type during the location estimation process. The complete location estimation process can be summarized by algorithm 2.

---

**Algorithm 2** Location, direction and modulation scheme detection

---

**Require:** 3-D spatio-temporal antenna array input signal  $w(n_x, n_y, n_{ct})$ .**Ensure:** Direction ( $\hat{d}_{ik}$ ), frequency ( $\hat{f}_{ik}$ ), modulation ( $\hat{m}_{ik}$ )

**Step 1:** Estimate the DOAs of signal sources using steerable 3-D IIR beam filter to obtain direction estimates  $(\psi_{ik}, \phi_{ik})$ ,  $i = 1, 2, \dots$  by analyzing the spatial power density function  $E(\psi, \phi)$ .

**Step 2:** For each estimated DOA  $(\psi_{ik}, \phi_{ik})$ , compute the directionally enhanced output  $y_{\psi_i, \phi_i}(n_{ct})$ .

**Step 3:** Compute the SCF  $S_{(\psi_{ik}, \phi_{ik})}(\alpha, f)$  using (3.8).

**Step 4:** Estimate the frequency  $f_{ik}$  in each direction using  $S_{(\psi_{ik}, \phi_{ik})}(0, f)$ .

**Step 5:** Examine unique signatures of  $S_{(\psi_{ik}, \phi_{ik})}(\alpha, f)$  to decide the modulation scheme in each direction  $(\psi_{ik}, \phi_{ik})$  for each  $DME_i$

**Step 6:** Send  $D_{ik} = [\hat{d}_{ik}, \hat{f}_{ik}, \hat{m}_{ik}]$  information to fusion center to obtain the location of each source.

---

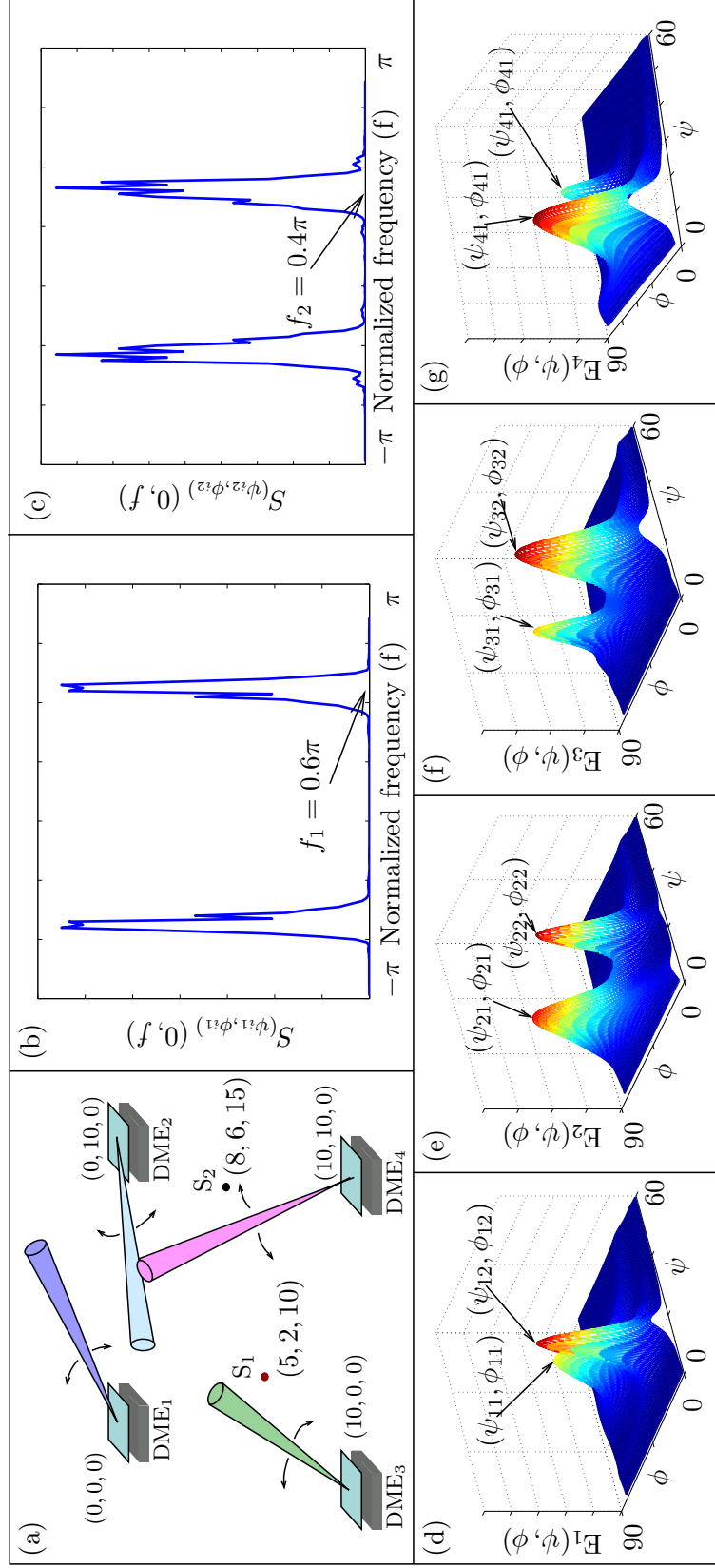


Figure 4.6: (a) Source distribution (b) SCF at  $\alpha = 0$ . (d-g) Spatial power distribution  $E(\theta, \phi)$  corresponding for the simulation 1

## 4.2 Simulated Localization and Directional Sensing Algorithm

In order to illustrate the detection procedure described by Algorithm 2, two simulation scenarios are presented. Simulation results show how the directional feature extraction can potentially be used to reduce detection space in the environment having multiple sources and reflections. Two signal sources with carrier frequencies 1.6 GHz and 2.4 GHz are considered. Each antenna array lies on the  $x - y$  plane with  $32 \times 32$  antenna elements. The DME stations are placed as shown in the Fig. 4.1(a). AWGN with a SNR of 6 dB is considered during the simulations.

***Simulation scenario 1:*** RF sources  $S_1$  and  $S_2$  with the carrier frequency  $f_{ct}$  1.6 GHz and 2.4 GHz are placed in the simulation environment as shown in Fig. 4.6(a). Same modulation type is assumed for both signal sources. Fig. 4.6 (d),(e),(f),(g) show the spatial power distribution  $E(\psi, \phi)$  of the four DME stations respectively, which are obtained by following step 1 in algorithm 2. Each  $E(\psi, \phi)$  shows two peaks which correspond to the two sources  $S_1$  and  $S_2$ . Local station estimates the sources  $S_i$ 's DOAs,  $(\psi_{ik}, \phi_{ik})$ , by calculating the coordinates of the local peaks in the power distribution. Spectral correlation functions  $S_{(\psi_i, \phi_i)}(\alpha, f)$  are then calculated for directionally enhanced signals along each estimated DOA. Since the modulation types are identical, same signatures in the SCF can be obtained. However, carrier frequency information can be exploited by evaluating the SCF on the  $\alpha = 0$  line,  $S_{(\psi_{ik}, \phi_{ik})}(0, f)$ , as shown in the figure 4.6 (b)-(c) and in turn can be used to differentiate the two sources at the fusion center.

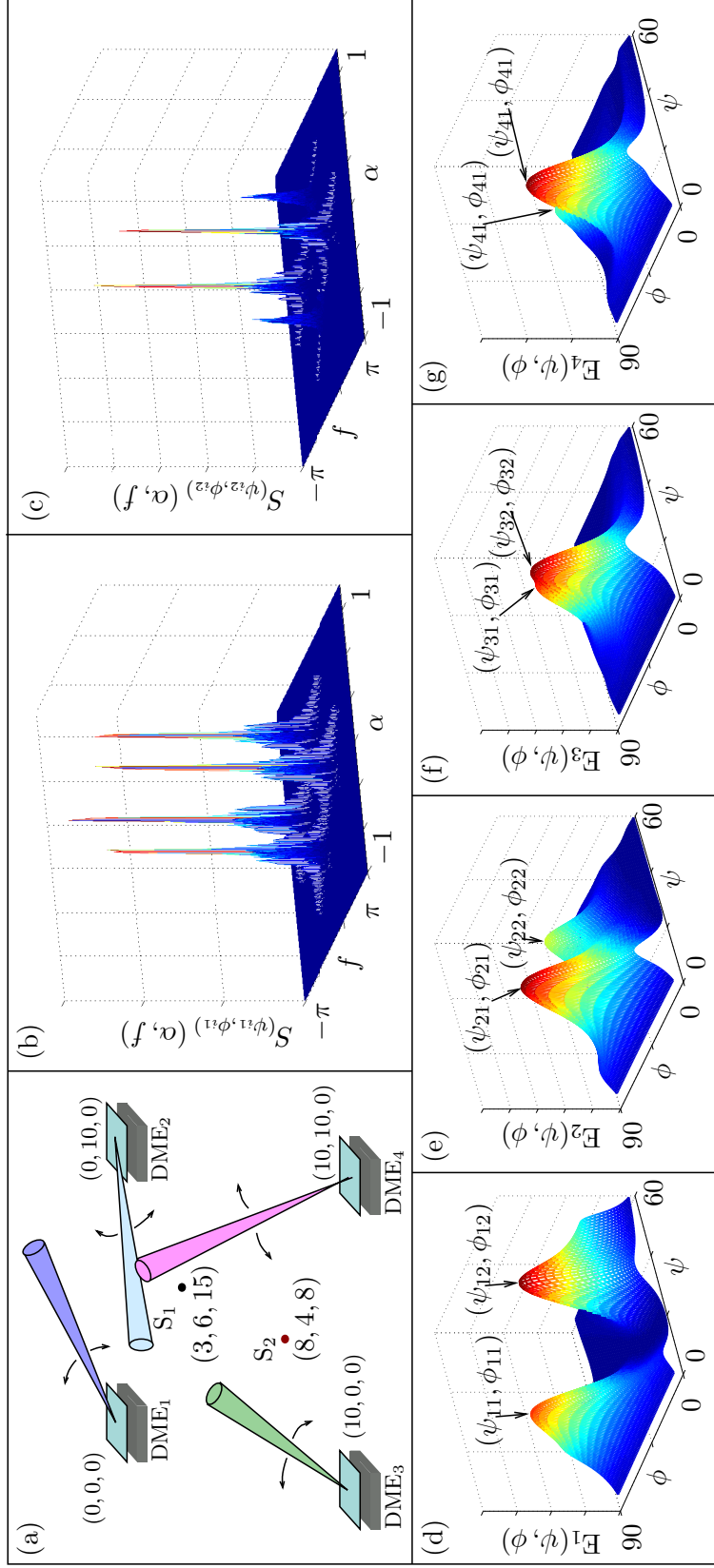


Figure 4.7: (a) Source distribution (b) Spectral correlation function (d-g) Spatial energy distribution  $E(\theta, \phi)$  corresponding for the simulation 2

*Simulation scenario 2:* This simulation consists of two sources  $S_1$  and  $S_2$  which have the same carrier frequency and two different modulation schemes BPSK and QPAM, respectively as shown in Fig. 4.7(a). Spatial power distribution for each DME station is shown in Fig. 4.7(d)-(g) which have two peaks corresponding to the two sources  $S_1$  and  $S_2$ . Fig. 4.7(b-c) show the SCF  $S_{(\psi_{ik}, \phi_{ik})}(\alpha, f)$  which can be obtained in each DME station for the two different sources. Fusion center can analyze eight SCFs and group according to the modulation type and then can be used to estimate the location of the sources by using (4.3).

### 4.3 Conclusions and Future Directions

The application of planar antenna arrays and low complexity array signal processing techniques to perform spatio-temporal signature detection in a cognitive radio environment is discussed. A number of receiver stations equipped with planar antenna arrays and 3-D IIR digital beam filters are employed to obtain direction estimations pertaining to radio sources. The 3-D IIR filters are used to perform highly selective electronically steerable directional filtering of radio waves. The directionally enhanced outputs are subjected to cyclostationary feature extraction to estimate the frequency and modulation information of the radio sources. Direction estimates from each receiver station are combined by a fusion center to estimate the position of each radio source.

CHAPTER V  
NETWORK-RESONANT PHASED-ARRAY (NRPA)-ENHANCED  
APPLEBAUM ADAPTIVE BEAMFORMER

Antenna array based digital adaptive beamformers enable electronically scanned directionally-agile RF beams required in a variety of applications ranging from radar, aerospace, RF sensing and tracking, and wireless communications[1, 7, 8, 9]. Applebaum beamformer is one of the commonly used adaptive phased array beamforming techniques, where the digitized antenna array signals are multiplied by an *adaptively optimized* set of array weights and combined (see Fig. 5.1(a)) [50] to achieve a main beam in the desired direction while nulling interference. The Applebaum beamformer is able to obtain the optimal beamforming performance in terms of SINR, with the knowledge of the desired DOA. New algorithms and circuits have been continuously explored to enhance the robustness of adaptive beamforming in order to further increase the performance in terms of accuracy and system complexity [51, 52, 53].

Spatial selectivity of an adaptive antenna array is reflected by the SINR improvement at the beamformed output, which is typically bounded by the array size [27]. For a given set of phased array weights, the digital beamforming back-end produces far-field array pattern having a desired beam direction and size together with side-

lobes defined by the amplitude distribution of the phased array weights (i.e., the spatial window of the antenna array aperture) and inter-antenna spacing. Side-lobes in the beamformer stop-band sets the noise and interference rejection. Side-lobe level of a phased array is reduced by optimizing the distribution of array weights and/or array element spacing at the cost of widening of the main beam (or increase in selected side-lobe amplitudes) [54, 55, 56]. For example, a real-coded generic algorithm

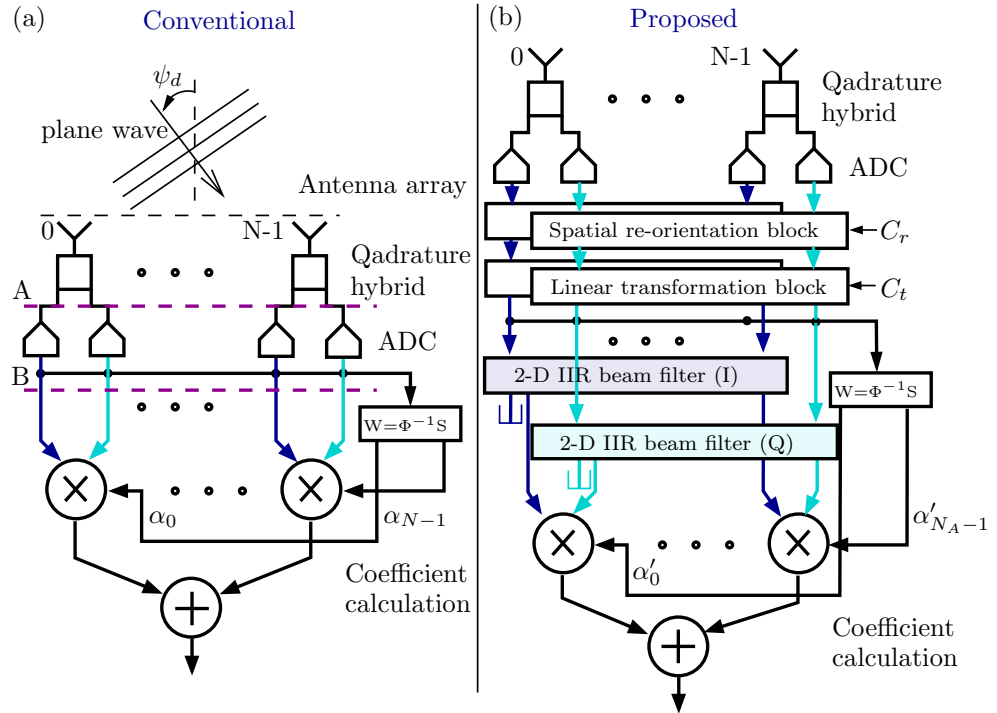


Figure 5.1: System architectures for (a) conventional Applebaum adaptive beamformers and (b) the proposed NRPA - enhanced Applebaum adaptive beamformers having increased spatial selectivity.

is employed in [55] to obtain optimum beamforming weights and element spacing.

Architectural modification to the Applebaum adaptive beamformer (see Fig. 5.1(a)) leading to a novel network resonant phased-array (NRPA) beamforming architecture

(2-D IIR beam filter that we discussed in Chapter 3) that allows further improvement to the established optimal Applebaum algorithm in terms of output SINR is proposed. That is, with the optimized phased array weights produced by the traditional Applebaum algorithm, proposed method aims to further improve the spatial selectivity via the introduction of hitherto unavailable degrees of freedom in the form of complex pole-manifolds in the array transfer function. Enhancement for the adaptive array is made possible because, for the first time in the literature to the best of our knowledge, we employ an adaptive array processing algorithm having both pole and zero manifolds in the transfer function. That is, the proposed NRPA system has zero-manifolds obtained using the optimal Applebaum adaptive array theory, and complex pole-manifolds (i.e. highly-directional denominator in the array transfer function) obtained using MD filter theory.

Fig. 5.1(b) shows the proposed NRPA for a ULA of antennas, which consists of two 2-D planar-resonant digital filters having infinite impulse response, operating on the in-phase (I) and quadrature (Q) input channels and subsequently feeding the I and Q inputs of the Applebaum array processor.

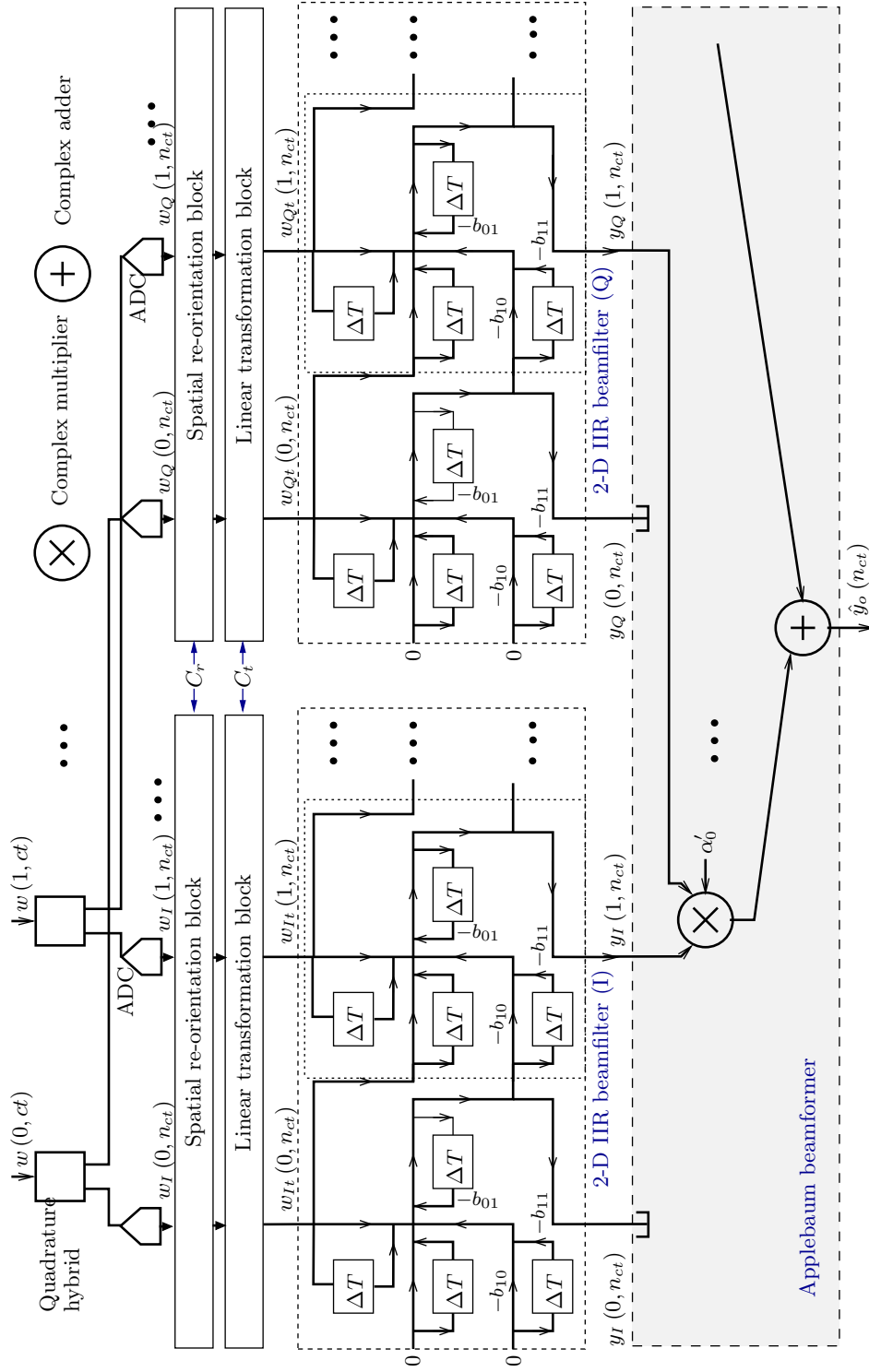


Figure 5.2: Signal flow graph of the proposed NRPA-enhanced Applebaum adaptive array architecture.

The proposed scheme transforms a weighted-sum Applebaum adaptive array into a weighted-IIR-filter-sum adaptive scheme, with trade-off of marginal increase in computational complexity. The inclusion of pole-manifolds via 2-D IIR digital filters leads to additional directivity in the array pattern that was not achievable from the traditional Applebaum phased-array structure. Furthermore, two pre-processing blocks as shown in Fig. 5.1(b), namely spatial re-orientation block and linear transformation block are proposed, to obtain maximum possible spatial selectivity while maintaining the p-BIBO stability of the entire system [32] for every angular direction. Operation and requirement of these blocks will be explained in detail in the subsequent sections.

This chapter unfolds as follows. Section 6.1 described the signal processing models for the NRPA system. Section 5.2 presents the system architecture including the operation of spatial re-orientation and linear transform blocks. The projected improvements in array selectivity are detailed in Section 6.3 with numerical simulations identifying SINR improvements for different test scenarios and operational modes. Section 5.4 concludes the chapter.

## 5.1 NRPA Beamforming Model

Consider the propagational scenario shown in Fig. 5.1(a), where a far-field plane-wave  $w_{pw}(x, ct)$  is received by a linear array of antennas uniformly placed along the  $x$  direction, where  $t$  is time and  $c$  is the speed of light. The spatially sampled plane-wave

is denoted by  $w(n_x, ct) = w_{pw}(n_x \Delta x, ct) + n(n_x, ct)$ , where  $n_x = 0, 1, 2, \dots, N - 1$  is the antenna index,  $\Delta x$  is the antenna spacing, and  $n(n_x, ct)$  denotes AWGN. To be consistent with the conventional Applebaum array setup, an RF front-end equipped with quadrature hybrids (QHs) and ADCs at each antenna is assumed, leading to a complex valued spatio-temporal discrete domain 2-D array signal  $\tilde{w}(n_x, n_{ct}) = w_I(n_x, n_{ct}) + jw_Q(n_x, n_{ct})$  (at B in Fig. 5.1(a)). Here,  $w_I(n_x, n_{ct})$  and  $w_Q(n_x, n_{ct})$  are orthogonal I and Q channels of the 2-D array signal, respectively, which will be processed independently by 2-D planar-resonant digital beam filters prior to Applebaum filtering. The detailed signal flow graph of the system is shown in Fig. 5.2.

### 5.1.1 Traditional Applebaum Adaptive Array Processing Model

Unlike the non-adaptive phased-arrays, Applebaum beamformer calculates the steering weights  $\alpha_i$  based on the information embedded in the received array signal (i.e. noise and interference) and the knowledge of the desired DOA  $\psi_d$ . Consider the input signal vector  $X$  at the output of the ADCs  $X = [\tilde{w}(1, n_{ct}), \tilde{w}(2, n_{ct}), \dots, \tilde{w}(N, n_{ct})]^T$ . The  $N \times N$  covariance matrix  $\Phi$ , which is the estimator of the received signals is obtained using the signal vector  $X$  as [50, 57]

$$\Phi = E(X^* X^T), \quad (5.1)$$

where  $E(\cdot)$  denotes expectation. Desired DOA  $\psi_d$  is used to obtain the steering vector  $S$  as [50, 57]

$$S = [e^{j\phi_d}, e^{j2\phi_d}, e^{j3\phi_d}, \dots, e^{jN\phi_d}]^T, \quad (5.2)$$

where  $\phi_d = \frac{2\pi\Delta x}{\lambda} \sin \psi_d$  and  $\lambda$  is the wavelength of the desired signal. The choice  $\lambda$  in the calculation of the steering weights results in an optimal adaptive *narrowband beamformer*, which leads beam-pointing errors for signals having frequencies  $f \neq c/\lambda$ . The optimum steering weight for the Applebaum beamformer is thus computed as [50, 57]

$$C = \Phi^{-1}S, \quad (5.3)$$

which contains information about the interference and noise, and the desired DOA. The optimum array weights given by (5.3) maximize the output SINR, which has a theoretical upper bound of  $10 \log_{10} N$  for AWGN [50, 52, 57]. Therefore, traditionally it is required to have more elements in the array (i.e. larger  $N$ ) to achieve better SINR improvement at increased computational and implementation cost. The beamformed output of the adaptive array  $\tilde{y}(n_{ct})$  can be obtained by evaluating the vector multiplication  $C^T X$  as shown in Fig 5.1(a). Applebaum beamformer with adaptive coefficients  $\alpha_i$ , can be modeled as a spatial FIR system having the  $\mathbf{z}$  domain transfer function

$$T_A(z_x) = \frac{1}{N} \sum_{i=0}^{N-1} \alpha_{N-i-1} z_x^{-i}. \quad (5.4)$$

Note that, (5.4) contains only zero-manifolds in the array transfer function. The selectivity of the transfer function increases with the number of antenna elements  $N$ , which correspond to the order of the spatial FIR filter. Thus, in the proposed architecture, we modify the transfer function in (5.4) by introducing complex pole-

manifolds from the 2-D IIR beamfilter, in turn improve the selectivity while slightly increasing the antenna array size.

### 5.1.2 Network-Resonant 2-D IIR Beamfilters

As shown in Fig. 5.2, we employ the I and Q signals for 2-D IIR pre-filtering stages to Applebaum adaptive array using planar-resonant digital beam filters. The 2-D IIR digital filters are designed by employing spatio-temporal resonant properties of MD passive prototype networks [18], in turn, leading to MD array transfer functions having complex pole-manifolds with prescribed passband shape, orientation, and directional selectivity [18]. For example, 2-D IIR digital plane-wave filters having beam-shaped passbands in the 2-D spatio-temporal frequency domain  $(\omega_x, \omega_{ct})$  can be used to selectively extract space-time spectra of 2-D array signals with a desired DOA while rejecting interference and noise spectra [58]. Such planar-resonant 2-D IIR filters are described by recursive spatio-temporal difference equations, which are p-BIBO stable and computable [20]. Importantly, the multi-input multi-output signal flow of the underlying 2-D difference equations allow us to employ such 2-D IIR digital filters as a pre-filtering stage to existing Applebaum adaptive arrays, which in turn leads to improved spatial selectivity [59].

Recall from Chapter 3 that the 2-D  $\mathbf{z}$  transform of the  $N$  element 2-D IIR beam filter can be obtained as

$$T(z_x, z_{ct}) = \frac{Y(z_x, z_{ct})}{W(z_x, z_{ct})} = P(z_{ct}) \left[ R(z_{ct}) \sum_{k=0}^{N-2} Q(z_{ct})^k z_x^{-(k+1)} + 1 \right]. \quad (5.5)$$

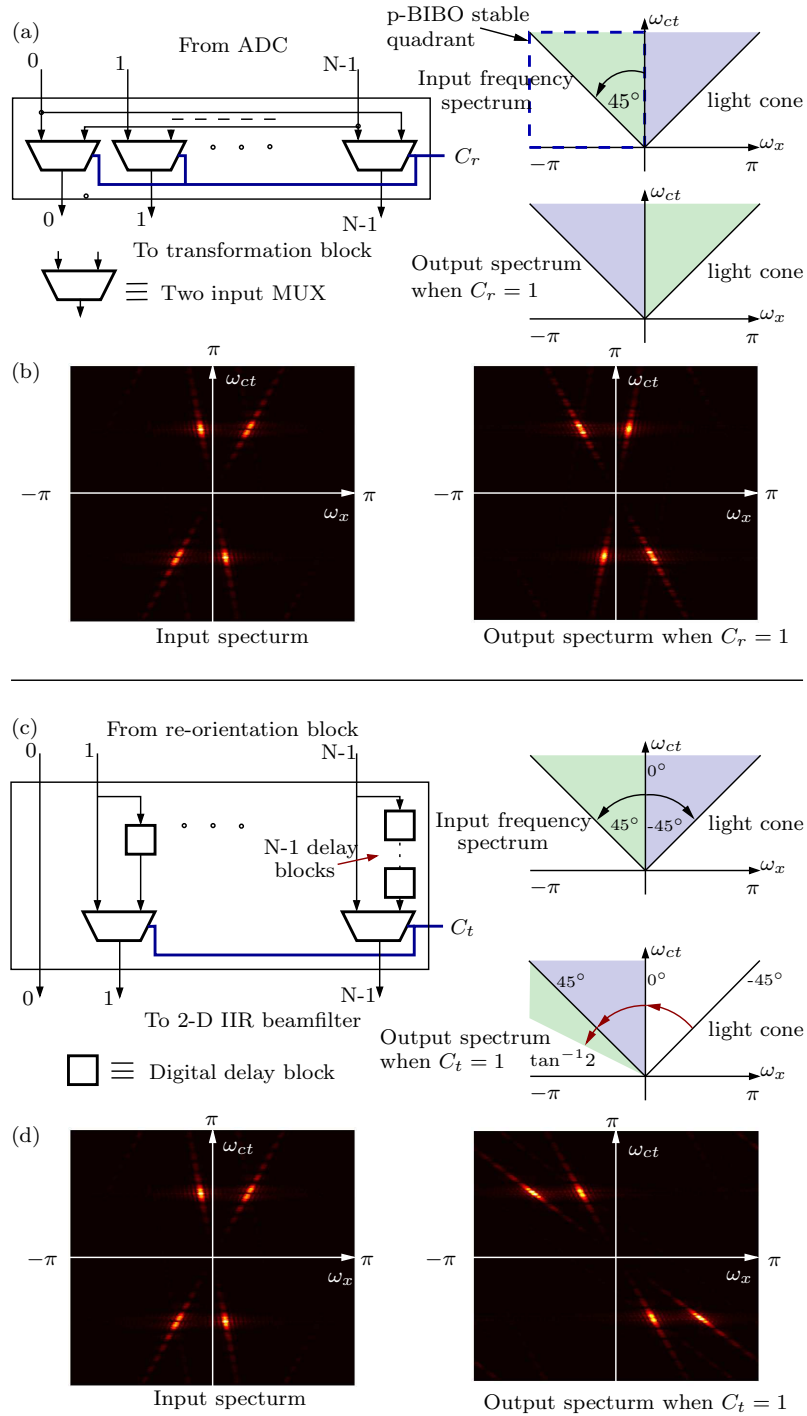


Figure 5.3: Digital implementation and 2-D frequency domain behavior of the (a-b) spatial re-orientation block (c-d) linear transformation block.

where  $P(z_{ct}) = \frac{1+z_{ct}^{-1}}{1+b_{01}z_{ct}^{-1}}$  and  $Q(z_{ct}) = \frac{-(b_{10}+b_{11}z_{ct}^{-1})}{1+b_{01}z_{ct}^{-1}}$ ,  $b_{ij} = \frac{R+(-1)^i L_x + (-1)^j L_{ct}}{R+L_x+L_{ct}}$ ,  $L_x = \cos \theta$  and  $L_{ct} = \sin \theta$ . Here  $\tan \theta = \sin \psi_d$ . In order to obtain the  $\mathbf{z}$  domain representations  $Y(z_x, z_{ct}) z_x^{-(N-1-n_x)}$  of each beam filter output  $y(n_x, n_{ct})$  ( $0 \leq n_x \leq N-1$ ), (5.5) can be expressed in the matrix form  $Y = AW$  where,

$$A = P(z_{ct}) = \begin{bmatrix}
1 & 0 & 0 & 0 & 0 & 0 & 0 & 0 \\
R(z_{ct}) & 1 & 0 & 0 & 0 & \cdot & 0 & 0 \\
Q(z_{ct})R(z_{ct}) & R(z_{ct}) & 1 & 0 & 0 & \cdot & 0 & 0 \\
Q(z_{ct})^2R(z_{ct}) & Q(z_{ct})R(z_{ct}) & R(z_{ct}) & 1 & 0 & \cdot & 0 & 0 \\
\cdot & \cdot \\
\cdot & \cdot \\
\cdot & \cdot \\
\cdot & \cdot \\
\cdot & \cdot \\
Q(z_{ct})^{N-2}R(z_{ct}) & Q(z_{ct})^{N-3}R(z_{ct}) & 0 & 0 & 0 & \cdot & R(z_{ct}) & 1
\end{bmatrix}, \tag{5.6}$$

$W$  is the 2-D  $\mathbf{z}$  domain representation

$$W = [z_x^{-(N-1)} \ z_x^{-(N-2)} \ z_x^{-(N-3)} \ \dots \ z_x^0]^T W(z_x, z_{ct}) \quad (5.7)$$

of the input signal vector  $W_a$

$$W_a = [w_a(0, n_{ct}) \ w_a(1, n_{ct}) \ w_a(2, n_{ct}) \ \dots \ w_a(N-1, n_{ct})], \quad (5.8)$$

and  $Y$  is  $\mathbf{z}$  domain representation of the outputs

$$Y = [z_x^{-(N-1)} \ z_x^{-(N-2)} \ z_x^{-(N-3)} \ \dots \ z_x^0] Y(z_x, z_{ct}). \quad (5.9)$$

## 5.2 NRPA-Enhanced Applebaum Adaptive Beamformer System Architecture

Fig. 5.2 shows the detailed system architecture of the proposed NRPA-enhanced Applebaum adaptive array consisting of four sub-systems: spatial re-orientation block; linear transform block; 2-D IIR digital beam filters; and Applebaum based-array. The spatial re-orientation block and the linear transform block are driven by the binary control signals  $C_r$  and  $C_t$ , respectively. If the numerator order of the 2-D IIR beam filter and the Applebaum beamformer are  $N_{2D}$  and  $N_A$ , respectively, the cascading of the beam filter with an adaptive array having  $N_A$  weights will necessitate a slightly larger array of  $N = N_{2D} + N_A$  elements. Typically,  $N_A \gg N_{2D}$  and in here,  $N_{2D} = 1$  and  $N = N_A + 1$ . In order to maintain the existing antenna array unchanged (with  $N$  antenna elements), number of elements in the Applebaum array  $N_A$  is selected as  $N_A = N - 1$ . That mean, the 2-D IIR beam filter evaluate its transfer function for total number of antenna elements in the array  $N$  and the last  $N_A = N - 1$  outputs,

ignoring the first  $N_{2D}$  to allow stabilization of the transient response of the numerator part of the 2-D beam filter, are used to feed the  $N_A$  inputs of the cascaded Applebaum array. Thus the proposed system requires  $N_A = N - 1$  number of coefficients for the Applebaum beamformer instead of  $N$  in the conventional system. New coefficients  $\alpha'_k$  ( $0 \leq k \leq N_A - 1$ ) are calculated based on the information at the output of the antenna array where last  $N_A$  outputs  $w(n_x, n_{ct})$ , where  $1 \leq n_x \leq N - 1$ , are utilized for the calculation. Thus, (5.4) and (5.5) lead to a combined transfer function  $T_C(z_x, s_{ct})$  of order  $N = (N_A + 1)$

$$T_C(z_x, s_{ct}) = \frac{1}{N} \sum_{l=0}^{N_A-1} \alpha'_l P(s_{ct}) \left[ R(s_{ct}) \sum_{k=0}^l Q(s_{ct})^k z_x^{-(k+1)} + 1 \right], \quad (5.10)$$

which contains both zero and pole manifolds in the 2-D complex transform domain  $(z_x, z_{ct}) \in \mathbb{C}^2$ , leading to enhanced spatial selectivity, where the Applebaum beamformer is a  $N_A = N - 1$ th order system. New weights vector of the  $N_A$ -input Applebaum array  $C_n = [\alpha'_0, \alpha'_1, \dots, \alpha'_{N_A-1}]^T$  can be used to obtain the equivalent matrix form of the transfer function  $T_C(z_x, s_{ct})$

$$T_C(z_x, s_{ct}) = C_n^T A W \quad (5.11)$$

where

$$A = P(z_{ct}) = \begin{bmatrix} R(z_{ct}) & 1 & 0 & 0 & 0 & \dots & 0 & 0 \\ Q(z_{ct})R(z_{ct}) & R(z_{ct}) & 1 & 0 & 0 & \dots & 0 & 0 \\ Q(z_{ct})^2 R(z_{ct}) & Q(z_{ct})R(z_{ct}) & R(z_{ct}) & 1 & 0 & \dots & 0 & 0 \\ \dots & \dots \\ \dots & \dots \\ \dots & \dots \\ \dots & \dots \\ Q(z_{ct})^{N-2} R(z_{ct}) & Q(z_{ct})^{N-3} R(z_{ct}) & 0 & 0 & 0 & \dots & R(z_{ct}) & 1 \end{bmatrix}, \tag{5.12}$$

is a  $N - 1 \times N$  matrix and  $W$  is the  $\mathbf{z}$  domain representation of the input vector, where  $N_A = N - 1$ . Here, the output is formed by a linear combination of IIR filtered input signals from each antenna (compare against the scaled-and-summed output of traditional phased-arrays) where each IIR filter is defined in closed form in terms of the original filter coefficients as well as the 2-D IIR beam filter coefficients.

The additional SINR gain obtained by the proposed system is a function of desired beam (main lobe) direction  $\psi_d$  which varies between  $-90^\circ$  and  $90^\circ$ . In order to obtain maximum possible SINR gain for different regions of the beam direction  $\psi_d$ , we define 4 modes of operation based on a critical angle  $\psi_c$ , which should be experimentally computed at the system calibration. The four operating modes are listed below. Note that angles ( $\psi_d$  and  $\psi_c$ ) measured counter clockwise from the array broadside direction are considered as positive.

- Mode 1:  $0 < \psi_c \leq \psi_d$ 
  - Desired DOA in  $-+$  quadrant in  $(x, y)$
  - $C_r = 0 \Rightarrow$  no spatial re-orientation
  - $C_t = 0 \Rightarrow$  no linear transformation
- Mode 2:  $0 \leq \psi_d < \psi_c$ 
  - Desired DOA in  $-+$  quadrant in  $(x, y)$
  - $C_r = 1 \Rightarrow$  spatial re-orientation required
  - $C_t = 1 \Rightarrow$  linear transformation required
- Mode 3:  $0 > \psi_d \geq -\psi_s$ 
  - Desired DOA in  $++$  quadrant in  $(x, y)$
  - $C_r = 0 \Rightarrow$  no spatial re-orientation
  - $C_t = 1 \Rightarrow$  linear transformation required
- Mode 4:  $0 > \psi_c > -\psi_d$ 
  - Desired DOA in  $++$  quadrant in  $(x, y)$
  - $C_r = 1 \Rightarrow$  spatial re-orientation required
  - $C_t = 0 \Rightarrow$  no linear transformation

Note that, the selection of these operating modes is defined by the critical angle  $\psi_c$  and beam direction  $\psi_d$ , which distinguishes between beamforming scenarios close to broadside and endfire directions of the array. Our motivation behind these operating modes is to obtain maximum possible SINR improvement and will be further explained in Section 6.3, which summarizes SINR gain obtained by each operating

mode for different beam directions. The significance of spatial re-orientation and linear transformation operations used in different operating modes will be discussed next.

### 5.2.1 Spatial Re-orientation

The spatial re-orientation block is required to maintain p-BIBO stability of the 2-D IIR digital filters. The 2-D IIR beam filter described by (5.5) can produce an electronically steerable beam-shaped passband in the  $-+$  quadrant in  $(\omega_x, \omega_{ct})$  while maintaining p-BIBO stability. That is, as long as the desired 2-D spectra (i.e. to be enhanced by the filter) lie within the  $-+$  quadrant in  $(\omega_x, \omega_{ct})$  plane, the 2-D IIR pre-filtering stage operates in its regular mode. However, for situations where the input 2-D spectra lie within the  $++$  quadrant in  $(\omega_x, \omega_{ct})$ , a spatial flipping of the input signal is required so that the input spectra is artificially flipped into the stable region of the 2-D IIR filter as shown in Fig. 5.3(a), thereby enabling stable computation of the underlying 2-D difference equation. Thus in the *typical operation*, if the desired spectra is already in the  $-+$  quadrant, re-orientation block passes the signal without any change by setting  $C_r = 0$ . If the desired spectra is in the  $++$  quadrant, the re-orientation buffer flips the array signal by setting  $C_r = 1$  [30, 29].

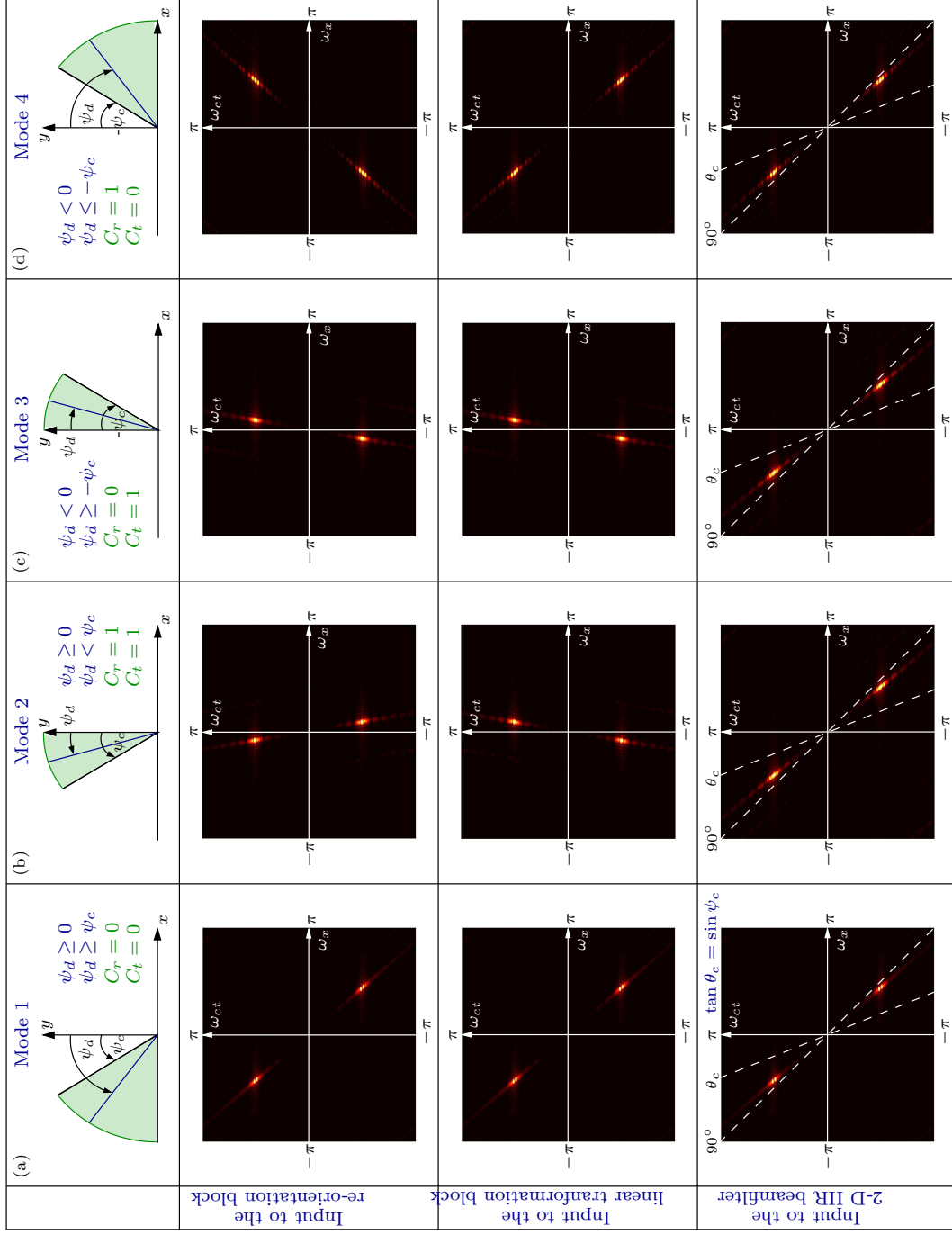


Figure 5.4: Behavior of the desired frequency spectrum at the input of each subsystem for each operational mode (a) Mode 1 ( $\psi_d \leq \psi_c$ ) (b) Mode 2 ( $\psi_c < \psi_d \leq 0$ ) (c) Mode 3 ( $0 \geq \psi_d > -\psi_c$ ) (d) Mode 4 ( $-\psi_c \geq \psi_d$ ).

However, in the proposed architecture *spatial re-orientation is employed even when the desired spectra is in the  $-+$  quadrant* of the 2-D frequency plane, especially near the broadside direction of the array (in operation mode 2). Furthermore, in near broadside direction of the  $++$  quadrant (in mode 3), *the proposed system ignores the use of spatial re-orientation by modifying its typical operation*. In such situations, a linear transform block is utilized to place the desired signal spectra into the p-BIBO quadrant in  $(\omega_x, \omega_{ct})$ . These functional modifications are introduced to obtain the maximum SINR performance from the proposed system. Operational conditions for the control signal  $C_r$  is

$$C_r = \begin{cases} 0 & \text{when } \psi_d \geq \psi_c > 0 \text{ or } 0 > \psi_d \geq -\psi_c \\ 1 & \text{when } 0 \leq \psi_d < \psi_c \text{ or } \psi_d \leq -\psi_c < 0 \end{cases} \quad (5.13)$$

where  $\psi_d$  is the desired DOA and  $\psi_c$  is the critical angle which is a constant defined between  $0^\circ$  and  $90^\circ$ . The DOA is transformed to  $\psi_r$  at the output of the spatial re-orientation where  $\psi_r$  become  $-\psi_d$  when  $C_r = 1$  and otherwise  $\psi_r = \psi_d$ . Fig. 5.3(b) shows the input and output frequency spectra (for  $C_r = 1$ ) for a input signal consisting of two planar waves with DOAs  $10^\circ$  and  $-30^\circ$ . The input signal DOAs  $10^\circ$  and  $-30^\circ$  are transformed to  $-10^\circ$  and  $30^\circ$ , respectively.

### 5.2.2 Linear Transformation

The SINR improvement of the proposed system is a function of the angular orientation of the desired signal spectra in the 2-D frequency domain. This will be reflected in the results presented in Section 6.3. The requirement of a linear transformation block

is to obtain higher SINR gain for beamforming scenarios near the array broadside direction. Therefore, for selected cases of the desired signal DOA (operation modes 2 and 3), a linear transform block is applied to transform the 2-D input spectra into a favorable region with high SINR gain, which would otherwise lead to lower SINR gain at beamformed output. The transformation block is implemented using a clocked delay lines and a multiplexer array as shown in Fig. 5.3(c), where digitized array signal at the  $i^{\text{th}}$  antenna is delayed by  $i$  time samples, for  $0 \leq i \leq N - 1$ . Thus, the linear transform modifies the spatio-temporal indexes  $n = [n_x \ n_{ct}]^T$  of the 2-D array signal as  $n^t = An$  where  $A = \begin{bmatrix} 1 & 0 \\ 1 & 1 \end{bmatrix}$  and transformed indexes  $n^t = [n_x^t \ n_{ct}^t]^T$ .

According to the multidimensional Fourier transform [31] the frequency variables are related by,

$$\begin{bmatrix} \omega_x^t \\ \omega_{ct}^t \end{bmatrix} = \begin{bmatrix} 1 & -1 \\ 0 & 1 \end{bmatrix} \begin{bmatrix} \omega_x \\ \omega_{ct} \end{bmatrix}. \quad (5.14)$$

where  $\omega_x^t$  and  $\omega_{ct}^t$  denote the frequency variables following the linear transform. The linear transformation maps the frequency spectra in the ++ quadrant into the -+ quadrant (which is the p-BIBO stable quadrant for 2-D IIR beam filter) of the  $(\omega_x, \omega_{ct})$  plane by relocating the spectrum in counterclockwise direction, where space-time angles  $-45^\circ$ ,  $0^\circ$ , and  $45^\circ$  are mapped to  $0^\circ$ ,  $45^\circ$  and  $\tan^{-1} 2$ , respectively (See Fig. 5.3(c)). Fig. 5.3(d) shows the frequency spectrum of the input and its transformed output for two plane-wave signals from  $10^\circ$  and  $-30^\circ$ . In order to maximize the SINR improve-

ment, the following conditions are defined for the control signal  $C_t$

$$C_t = \begin{cases} 0 & \text{when } \psi_d \leq -\psi_c \text{ and } \psi_d \geq \psi_c \\ 1 & \text{when } -\psi_c < \psi_d < \psi_c \end{cases} \quad (5.15)$$

Transformed DOA  $\psi_t$  at the output of the transformation block is obtained in terms of  $\psi_r$  and is expressed as

$$\psi_t = \sin^{-1}(\sin(\psi_r) + 1) \quad (5.16)$$

*Thus, for computation of the 2-D IIR beam filter coefficients and the optimal Applebaum weights,  $\psi_t$  is used as the design angle instead of the original DOA  $\psi_d$ .*

### 5.2.3 Spectral Characteristics of Different Operational Modes

Fig. 5.4 shows the orientation of the signal spectra in the 2-D frequency domain following spatial re-orientation and linear transformation in each operating mode. The primary objective of the re-orientation and transformation blocks is to bring the desired frequency spectrum into a region where the beamforming subsystem (2-D IIR beamfilter + Applebaum beamformer) is able to obtain maximum SINR improvement while preserving p-BIBO stability conditions of the 2-D IIR beam filter. Thus, following re-orientation and linear transform, the beamforming system requires that the desired 2-D spectra lie inside the  $-+$  quadrant of the 2-D light cone. This condition will also ensure to provide a design DOA  $\psi_t$  to calculate the filter parameters for the Applebaum algorithm and 2-D IIR beam filters. As verified by the numerical simulations in Section 6.3, the NRPA-enhanced Applebaum beamformer, without the linear transformation, performs well if the desired DOA is near the array end-

fire direction (i.e.  $\psi_d \geq \psi_c$ ). Therefore, the control signals  $C_r$  and  $C_t$  are defined in such a way that the desired signal spectrum appears near the endfire direction in the  $-+$  quadrant of light cone, prior to the 2-D IIR beam filter (see Fig. 5.4 last row).

When the desired beam direction is close to the positive endfire direction of the antenna array (i.e.  $\psi_d \geq \psi_c$ ), the proposed system operates in mode 1 (Fig. 5.4(a)), where re-orientation and transformation blocks pass their input signals without modifying them, thereby keeping the input frequency spectrum unchanged. For signals near the positive broadside direction (i.e.  $\psi_d < \psi_c$  and in  $-+$ quadrant of  $(\omega_x, \omega_{ct})$ ), we employ linear transformation to improve the SINR gain. However, the transformation will place the desired signal spectra outside the light cone. Thus, we require a spatial re-orientation prior to the linear transformation as shown in Fig. 5.4(b) (mode 2) to bring the desired spectra into the  $++$  quadrant before applying the transformation. Then the transformation brings back the signal spectra into the stable half of the light cone and near to the endfire direction, where the SINR improvement is maximum.

In mode 3 (see Fig. 5.4(c)), we only employ the linear transformation, which is sufficient to place the desired spectra in stable near endfire region where SINR gain is maximized. Fig. 5.4(d) describes mode 4, where only re-orientation is sufficient to bring the desired spectra into the maximum SINR gain region of the proposed 2-D filtering scheme. Note that in the last row in Fig. 5.4, it is clear that the proposed

architecture modifies the array input signal to appear in the stable near endfire direction at the input to the 2-D IIR beamfilter. Fig. 5.4 assumes  $\psi_c = 30^\circ$  and desired signals from  $60^\circ, 10^\circ, -10^\circ$  and  $-60^\circ$  for mode 1-4, respectively.

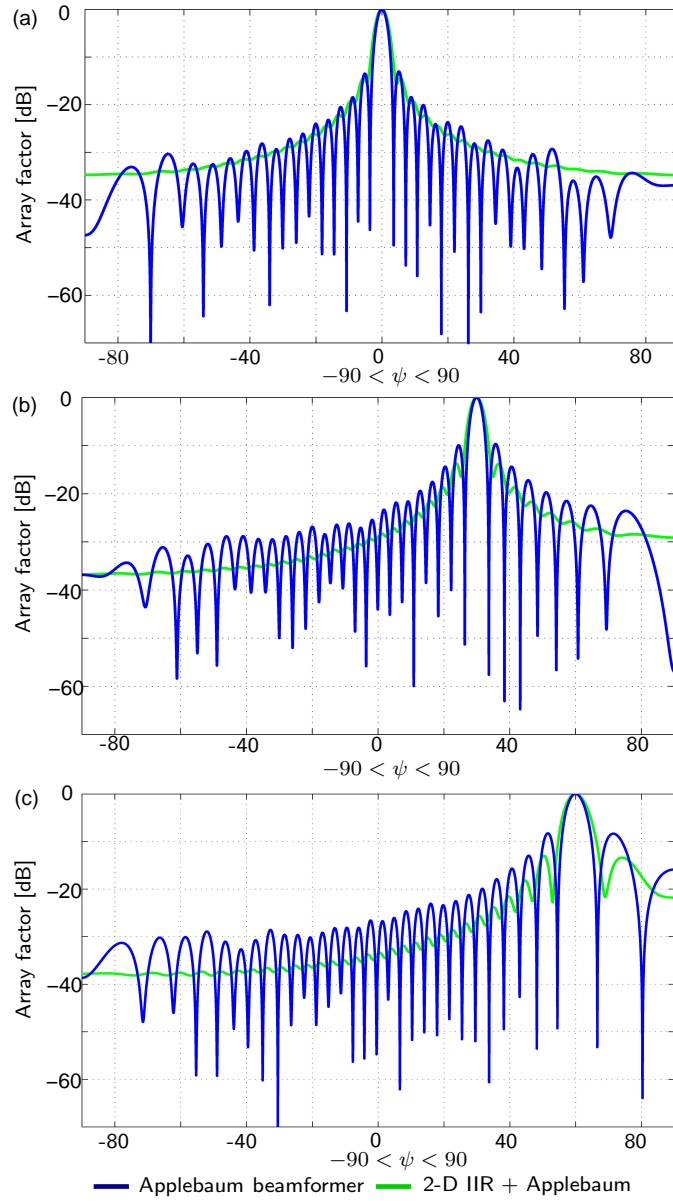


Figure 5.5: Expected directivity improvement of the proposed method in terms of the array factor of the beamformer.

#### 5.2.4 Beamforming Subsystem

Following re-orientation and linear transform according to the operating mode, the 2-D array signal is sent through two 2-D IIR beamfilters for I and Q channels, followed by the Applebaum beamformer having optimal weights  $C_n$ . Note that, the Applebaum weights are calculated using the last  $N - 1$  signals at the output of the linear transformation block  $\tilde{w}_t(n_x, n_{ct}) = w_{It}(n_x, n_{ct}) + jw_{Qt}(n_x, n_{ct}) \in \mathbb{C}$  and the apparent DOA  $\psi_t$  instead of the original DOA  $\psi_d$ . In the conventional method, information at the QH (at B in Fig. 5.1(a)) is employed with the desired DOA  $\psi_d$  for the adaptive coefficient calculation.

#### 5.2.5 Array Patterns Reflecting the SINR Improvement

Improved spatial selectivity can be compared in the array factors of the Applebaum adaptive array and the proposed NRPA enhanced Applebaum architectures. Applebaum array factor is computed by evaluating  $C^T X$  for each spatial angle  $-\frac{\pi}{2} < \psi < \frac{\pi}{2}$ , where  $X = [e^{j\phi}, e^{j2\phi}, e^{j3\phi}, \dots, e^{jN\phi}]^T$  and  $\phi = \frac{2\pi\Delta x}{\lambda} \sin \psi$ . Note that, when  $\psi = \psi_d$ , the array factor shows a maximum, leading to a beam pointing at the desired DOA  $\psi_d$  at the temporal frequency  $f = c/\lambda$ . For the 2-D IIR digital pre-filter, the array factor is computed by evaluating the frequency response at a given temporal frequency  $\omega_{ct0}$  as a function of the spatial angle  $\psi$  by setting  $z_x = e^{-j\omega_{ct0} \sin \psi}$  and  $z_{ct} = e^{j\omega_{ct0}}$  in (5.5). Array factor of the complete system is given by (5.10). BPSK modulated signals with  $0.5\pi$  normalized frequency and 1% fractional bandwidth ( $B_f$ ) are considered for the simulation. Fig. 5.5(a-c) shows the comparison of the array factors

between the Applebaum beamformer and the proposed system for  $\psi_d = 0^\circ, 20^\circ$  and  $40^\circ$ , for a ULA of 64 elements. Improved spatial selectivity in terms of reduced side-lobe levels (while preserving the main beam selectivity) is depicted in Fig. 5.5 where it shows a gradually increasing improvement when the beam direction moves towards the end-fire direction of the antenna array. No improvement can be seen for the broad side direction.

### 5.3 Enhanced Selectivity and SINR Improvement

In order to understand the significance of the four modes of operation, we analyze the SINR improvement at the beamformed output for two simulation models (SMs) defined as follows. In the SM1, only the spatial re-orientation block is considered prior to the beamforming subsystem to flip the desired frequency spectrum into  $-+$  quadrant. Control signal for spatial re-orientation is defined as  $C_r = 0$  and  $C_r = 1$  for positive ( $\psi_d \geq 0$ ) and negative ( $\psi_d < 0$ ) angles of the beam direction  $\psi_d$ , respectively. This system is identical to the case, where the control signal  $C_t = 0$  for every direction with the re-orientation block is in its typical operation. In the SM2 spatial transformation block is employed ( $C_t = 1$ ) following to the re-orientation block with the control signal  $C_r = 1$  for  $\psi_d \geq 0$  and  $C_r = 0$  for  $\psi_d < 0$ . Note that, the re-orientation block flips the array signal even when the desired beam direction is in the  $-+$  quadrant. Furthermore, when the desired beam direction is in the  $++$  quadrant, re-orientation block passes the input signal without flipping it. Thus the linear transformation block is responsible to bring the desired signal spectra into the

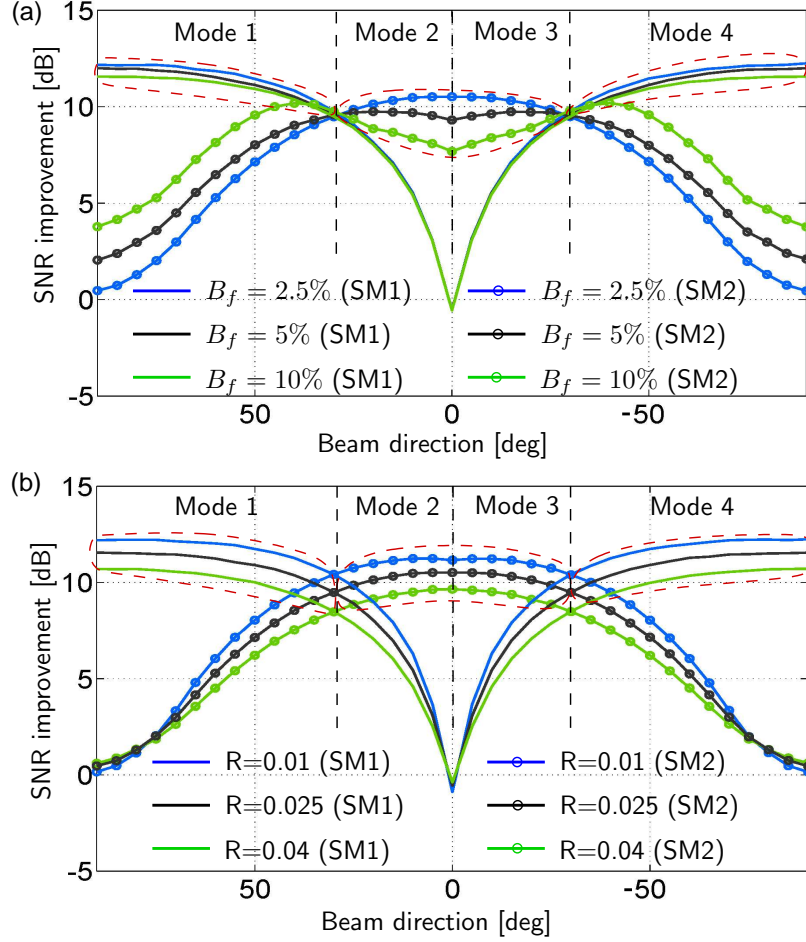


Figure 5.6: Comparison of the SNR improvement of the proposed NRPA enhanced Applebaum array for SM1 and SM2 with (a) varying fractional bandwidth ( $B_f$ ) of the input signal and (b) varying 2-D IIR beam filter parameter  $R$ .

stable  $-+$  quadrant, while obtaining maximum possible SINR improvement. SINR improvement of the proposed method, compared to the Applebaum beamformer, is evaluated separately for both simulation models and presented in different curves with respect to the desired beam direction  $\psi_d$  in Fig. 5.6 and Fig. 5.7.

Table 5.1: Selection of appropriate simulation model for each region of beam direction with the corresponding control bit selection.

Beam direction	SINR improvement of SM1	SINR improvement of SM2	Selected SM	$C_r, C_t$	Mode
$\psi_d \geq \psi_c$	high	low	SM1	0 0	Mode 1
$\psi_c < \psi_d \leq 0$	low	high	SM2	1 1	Mode 2
$0 > \psi_d \geq -\psi_c$	low	high	SM2	0 1	Mode 3
$-\psi_c > \psi_d$	high	low	SM1	1 0	Mode 4

The critical angle  $\psi_c$ , which decides the boundaries for each operation mode, is defined as the positive intersection angle of the two improvement curves (see Fig. 5.7). The most appropriate mode of operation and their control signals for a particular beam direction  $\psi_d$  are then determined based on the simulation model, which corresponds to the highest SINR improvement ( $\max\{\text{SM1}, \text{SM2}\}$ ).

First, we measured the SNR improvement of the proposed architecture with an input SNR of -10 dB and considering no interference. Fig. 5.6 shows the SNR improvement corresponding to the two SMs for different fractional bandwidths of the input signal. It is clear that the SNR improvement increases towards the endfire direction and reduces near the broadside direction for SM1. The SNR improvement for SM2 exhibits an opposite variation to the SM1, as expected. The introduction of the linear transformation block in SM2 leads to better system gain around the broadside direction. Thus we are able to use a combination of the two simulation models to obtain the maximum possible SNR improvement for different regions of the beam direction (selected SM curves are circled in red), provided that we select control signals  $C_t$  and  $C_r$  accordingly as discussed in Section 5.2.

Desired angular regions for each operating mode are marked in Figs. 5.6 and 5.7, where region boundaries are defined based on the critical angle  $\psi_c$  and the broadside direction. For example, in  $\psi_d \geq \psi_c$  region SM1 curve shows a higher improvement than SM2 and in  $\psi_c < \psi_d \leq 0$  region SM2 curve exhibits a higher improvement than

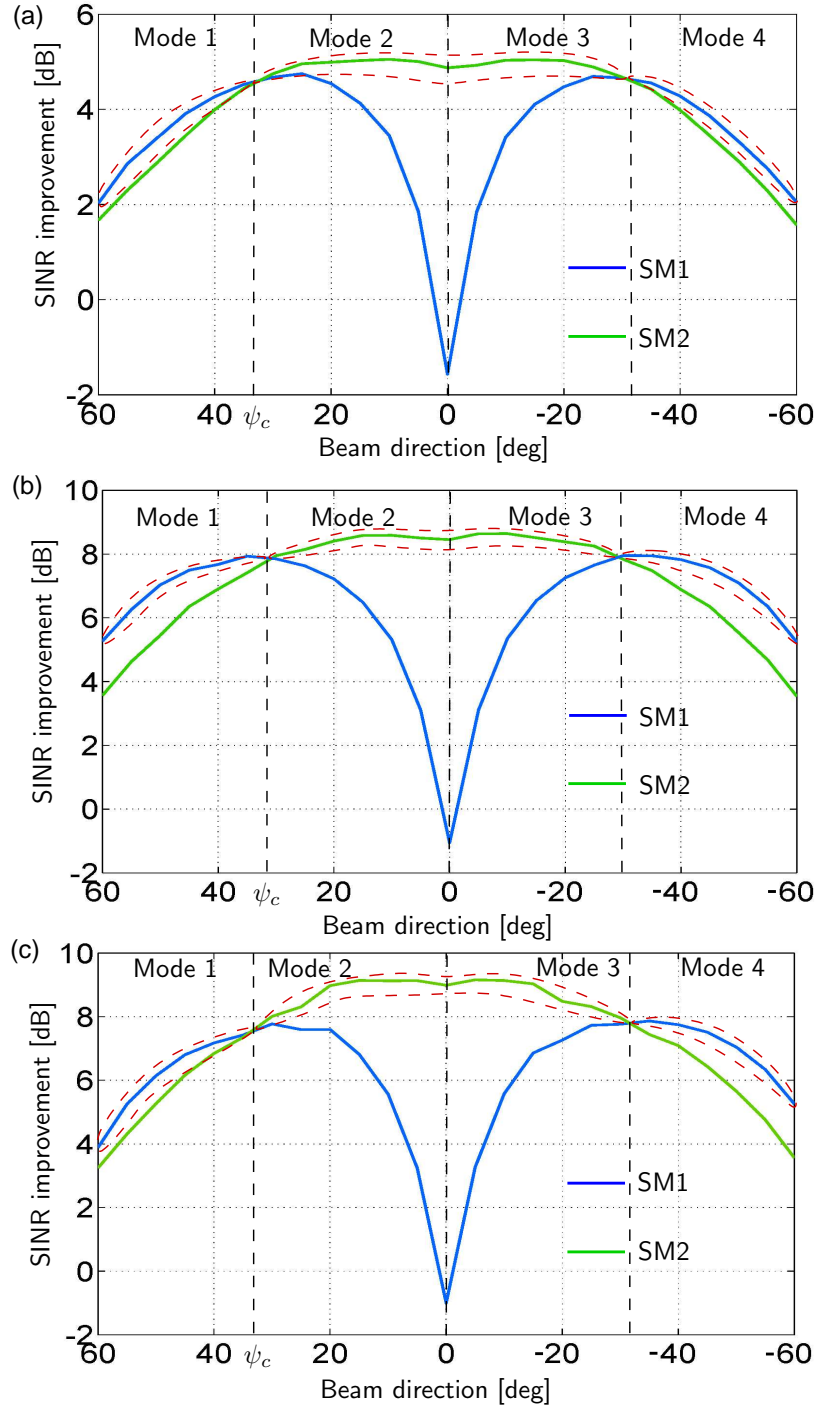


Figure 5.7: SINR improvement of SM1 and SM2 for different simulation scenarios. Variation with respect to the desired beam direction  $\psi_d$ , (a) with two interference in the directions  $\psi_d \pm 10$  (b) with two interference in the directions  $\psi_d \pm 20$  (c) four interference in  $\psi_d \pm 10$  and  $\psi_d \pm 20$ .

SM1. Thus the operation mode 1 and mode 2 are defined to select appropriate SMs to obtain the maximum possible improvement. Table 5.1 summarizes the selection of the appropriate SM for each region of the beam direction with their corresponding control signals for spatial re-orientation and linear transformation. Fig. 5.6(b) compares the SNR improvement variation with the 2-D IIR digital filter parameter  $R$ , which shows increased SNR improvement for lower values of  $R$  (i.e. increased sharpness of the 2-D IIR beam filter passband).

We then compute the improvement in the SINR obtained by the NRPA-enhanced Applebaum array, for different simulation scenarios with -6dB input SIR and -9dB input SNR values. Fig. 5.7(a) and (b) show the SINR improvement for the desired beam direction  $\psi_d$  ( $-60 \leq \psi_d \leq 60$ ) with two interference in the directions  $\psi_d \pm \alpha$ , where  $\alpha$  is selected as  $10^\circ$  and  $20^\circ$  respectively for the two graphs. For Fig. 5.7(c), we consider the desired signal from DOA  $\psi_d$  with four interference in  $\psi_d \pm \alpha$  and  $\psi_d \pm \beta$ , where  $\alpha = 10^\circ$  and  $\beta = 20^\circ$ . Based on the desired beam direction, the most appropriate operating mode is selected such that maximum SINR improvement is achieved. For each beam direction the proposed system confirms a better than 3 dB (upto 9 dB) improvement in terms of SINR.

#### 5.4 Conclusions

A novel array processing architecture is proposed to enhance the SINR improvement of the conventional Applebaum adaptive array beamformers. 2-D planar-resonant

digital beamfilters combined with a spatial re-orientation and linear transformation of the array signals are employed prior to the Applebaum beamformer to obtain improved spatial selectivity. Insertion of the 2-D IIR beamfilter change the zero-manifold only transfer function of the conventional beamformer by introducing complex manifolds from the recursive beamfilter architecture at guaranteed stability. Proposed beamforming architecture shows a significant improvement in SINR when the DOA of the desired signal is off-axis from the broad side direction. A linear transformation block is proposed to further improve the performance of the proposed method in terms of SINR improvement around the broadside direction of the antenna array. Combination of the 2-D IIR beamfilter and transformation is able to achieve between 3 dB to 9 dB SINR improvement along every beam direction.

CHAPTER VI  
NETWORK-RESONANCE APPLEBAUM ADAPTIVE ARRAYS FOR  
DIRECTIONAL SPECTRUM SENSING

Continuously expanding applications of wireless communications networks results in higher demands for RF spectrum, making it an increasingly scarce natural resource. PUs are licensed to occupy narrow chunks of spectrum through a spectral licensing process from authorities, such as the FCC in the United States, for example. In the presence of impending spectral scarcity, there is a need to maximize spectrum resources without affecting the licensed users (that is, the PUs) performance. CR attempts to reduce scarcity by utilizing licensed frequency bands that are temporarily left unused by their PUs. These transient spectral openings are known as white spaces. CRs create opportunistic communication links [60] for SUs who are not licensed by the authorities, in a manner such that the operation of the SUs have absolutely no impact on the performance and operation of the PUs. This requires a level of “intelligence”, i.e., cognitive abilities, in the SUs, leading to CR algorithms and the related process of discovering white spaces in the radio spectrum. The real-time detection of white spaces is called spectrum sensing. Spectrum sensing plays a major role in the CR implementation because the SUs can only operate when a white space is detected with very high reliability.

The precise real-time detection of frequency, modulation type, direction, and location information of PU radios is critically important for CRs. Directional spectrum sensing is challenging in situations with high levels of noise and interference, leading to false detection in spectral estimation and feature detection algorithms. PUs can be located far away from the SUs, which implies that the PU's signal strength can be small at the spectrum sensor. Thus spectrum sensing requires robust algorithms to work in situations with low SNR and high level of interference. Directional spectrum sensing and feature detection exploits DOA of radio sources, in addition to frequency and modulation type towards increasing the opportunistic spectral access [61]. An adaptive antenna array [50, 57] processing based on the Applebaum algorithm in conjunction with 2-D planar-resonant IIR beam filters and cyclostationary feature detection is proposed to perform directional spectrum sensing. The Applebaum adaptive array does not require a priori knowledge of the statistical properties of the desired signal. Nor does it require a reference copy of the expected wave-form. Because the Applebaum adaptive algorithm provides an optimal set of array weights when the direction of the main-beam is known, it is the algorithm of choice for directional scanning of the radio environment under control of algorithms that have the look-direction of the directional spectrum sensor as an independent variable. By selecting a desired direction for sensing, and finding the set of optimal array weights for that direction using the Applebaum algorithm, the optimal sensor obtains the best SINR for the received signal.

In an Applebaum adaptive phased-array directional spectrum sensor, directional information of sources are obtained employing antenna array beamformers as shown in Fig. 6.1(a). At a particular direction, the occupied frequencies are detected by analyzing the directionally enhanced output of the beamformer utilizing algorithms, such as energy detection, cyclostationary feature detection and waveform sensing [62]. The proposed directional spectrum sensor is shown in Fig. 6.1(b). Here, the conventional directional spectrum sensor is modified by introducing a 2-D IIR frequency-planar beam pre-filtering stage, which is shown to provide an improved spatial selectivity (as discussed in Chapter 5). The insertion of the 2-D IIR beamfilter modifies the zero-manifold-only transfer function of the Applebaum beamformer by introducing complex-pole manifolds at guaranteed practical-BIBO stability [32]. The inclusion of pole-manifolds leads to additional directivity from the array pattern that was not achievable from the traditional phased-array structure. The proposed method improves the spatial selectivity of the array (i.e., reduced side lobes), which in turn, improves SINR of the spectrum sensor. The improved SINR at the input to the cyclostationary detector enhances the performance (accuracy) of the feature detection by suppressing the detrimental effects of noise and directional interference to a degree that is not achievable by using only an Applebaum adaptive array.

## 6.1 Signal Processing Model

A propagating 2-D plane wave  $w_d(x, ct)$  received by a linear antenna array with inter-antenna spacing  $\Delta x$ , is denoted as  $w(n_x, ct) = w_d(n_x \Delta x, ct)$ , where  $n_x =$

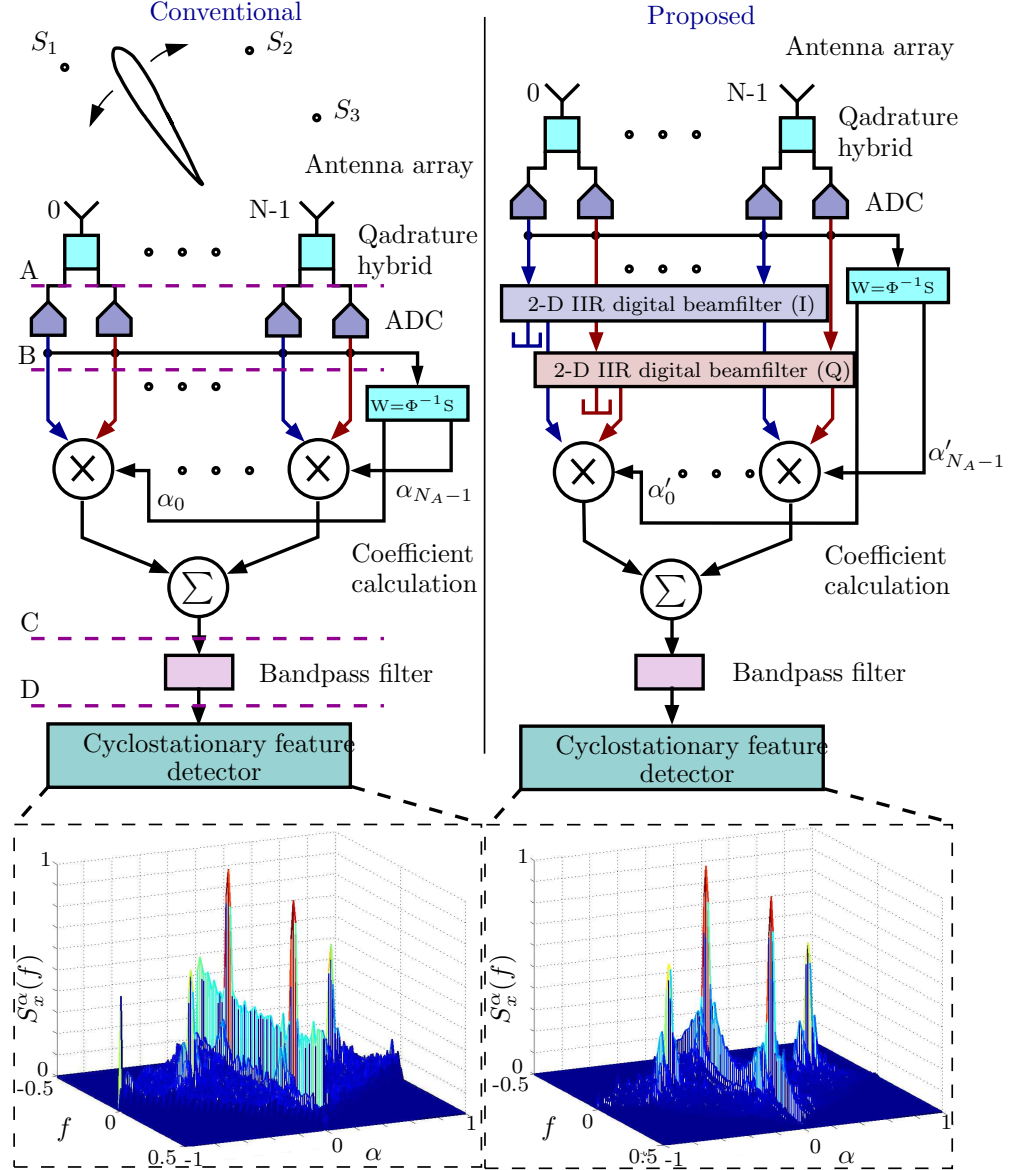


Figure 6.1: Directional spectrum sensing architectures using antenna array processing and Cyclostationary feature detection: (a) conventional approach with Applebaum adaptive beamformers and (b) proposed approach based on 2-D IIR filter based array processing with enhanced noise suppression capability.

$0, 2, 3, \dots, N - 1$  is the antenna index and  $ct$  is time  $t$  that has been normalized by the wave speed  $c$ . Digitized complex signal  $\tilde{x}(n_x, n_{ct}) = x_I(n_x, n_{ct}) + jx_Q(n_x, n_{ct})$  of  $x(n_x, ct)$  is obtained at the output of the analog-to-digital converters (at A in

Fig. 6.1(a)),  $I$  and  $Q$  correspond to in-phase and quadrature components, respectively.

### 6.1.1 Applebaum Adaptive Beamformer

According to the Chapter 5, Applebaum beamformer calculates the steering weights  $\alpha_i$  based on the information in the received signal and the knowledge of the desired DOA  $\psi_d$ . Consider the input signal vector  $X$  at the output of the ADCs  $X = [\tilde{w}(1, n_{ct}), \tilde{w}(2, n_{ct}), \dots, \tilde{w}(N, n_{ct})]^T$ . The  $N \times N$  complex covariance matrix  $\Phi$  is obtained using the signal vector  $X$  as  $\Phi = E(X^*X^T)$ . Here,  $E(\cdot)$  is the expectation operator. Desired DOA  $\psi_d$  is used to obtain the steering vector  $S = [e^{j\phi_d}, e^{j2\phi_d}, e^{j3\phi_d}, \dots, e^{jN\phi_d}]^T$ , where  $\phi_d = \frac{2\pi\Delta x}{\lambda} \sin \psi_d$  and  $\lambda$  is the wavelength of the desired signal. The optimum weight vector is calculated via the relation  $C = \Phi^{-1}S$ . The optimum weights  $W$  maximizes the SINR at the output of the Applebaum array, and has a theoretical maximum improvement of  $10 \log_{10} N$  for AWGN [50, 52, 57]. This emphasizes the requirement of increasing the number of antennas to obtain a higher SINR improvement at increased implementation cost.

### 6.1.2 Cyclostationary Feature Detection

Recall from Chapter 3 that the features embedded in cyclostationary signals [47, 63], including information about modulation scheme and the carrier frequency, can be extracted by analyzing cyclostationary estimator SCF, which is obtained from the CAF. SCF  $S_{\tilde{y}}(f, \alpha)$  of the beamformer output  $\tilde{y}(n_{ct})$  (at B in Fig. 6.1(a)) expressed as the Fourier transform of the CAF  $R_{\tilde{y}}^\alpha(k)$  [63].

$$S_{\tilde{y}}(f, \alpha) = \sum_{k=-\infty}^{\infty} R_{\tilde{y}}^{\alpha}(k) e^{-j2\pi f k} \quad (6.1)$$

where

$$R_{\tilde{y}}^{\alpha}(k) = \lim_{M \rightarrow \infty} \frac{1}{2M+1} \sum_{n=-M}^M \left[ \tilde{y}(n+k) e^{-j\pi\alpha(n+k)} \right] \left[ \tilde{y}(n) e^{j\pi\alpha n} \right]^*.$$

$f$  and  $\alpha$  are the temporal and cycle frequencies, respectively. The SCF provides different peak profiles for each modulation, which leads to classify the modulation scheme. Furthermore, the  $\alpha = 0$  line of the SCF [47] corresponds to the PSD of the received signal which can be used to detect the carrier frequency of the signal.

### 6.1.3 Network-Resonant 2-D IIR Beamfilter

The concept of multi-dimensional network resonance [18] has been employed to design p-BIBO stable [32] 2-D IIR digital filters for broadband beamforming applications [19]. Such 2-D IIR filters have beam shaped filter passbands in the 2-D spatio-temporal frequency domain  $(\omega_x, \omega_{ct})$ , where  $\omega_x$  and  $\omega_{ct}$  are the spatial and temporal frequency variables, respectively. A beam shaped 2-D filter passband is required to selectively encompass the spatio-temporal spectrum having a desired DOA  $\psi_d$  [19]. Recall from Chapter 3 that the 2-D  $\mathbf{z}$  transform of the  $N$  element 2-D IIR beam filter can be obtained as

$$T(z_x, z_{ct}) = \frac{Y(z_x, z_{ct})}{W(z_x, z_{ct})} = P(z_{ct}) \left[ R(z_{ct}) \sum_{k=0}^{N-2} Q(z_{ct})^k z_x^{-(k+1)} + 1 \right]. \quad (6.2)$$

where  $P(z_{ct}) = \frac{1+z_{ct}^{-1}}{1+b_{01}z_{ct}^{-1}}$ ,  $Q(z_{ct}) = \frac{-(b_{10}+b_{11}z_{ct}^{-1})}{1+b_{01}z_{ct}^{-1}}$ ,  $R(z_{ct}) = 1 + Q(z_{ct})$ ,

$b_{ij} = \frac{R+(-1)^i \cos \theta + \sin \theta (-1)^j}{R + \cos \theta + \sin \theta}$  with  $b_{00} = 0$  [19]. Here  $\theta = \tan^{-1}(\sin \psi_d)$  [18, 19]. The

multi-input-multi-output characteristic of the 2-D IIR beamfilter corresponds to the (6.2), allows us to employ  $T(z_x, z_{ct})$  as a pre-filter to existing Applebaum adaptive array (see Fig. 6.1(b)).

## 6.2 Proposed Directional Cyclostationary Feature Detector

Directional information pertaining to each signal source  $S_i$  (DOA  $\psi_i$ ) is obtained by scanning the CR environment by producing an electronically steerable beam from the beamforming front-end, and subsequently performing a peak energy detection. Feature detection is then applied to each detected DOA to estimate the carrier frequency and modulation scheme. In the proposed spectrum sensor, discrete domain I-Q signals  $x_I(n_x, n_{ct})$  and  $x_Q(n_x, n_{ct})$  are sent through two separate 2-D IIR beamfilters as shown in Fig. 6.1(b), followed by the Applebaum beamformer having optimal weights  $C_n$  (as described in Chapter 5), which are calculated utilizing the last  $N - 1$  signals at the output of the ADCs  $\tilde{x}(n_x, n_{ct})$ . Here, 2-D IIR beam filter accepts signals from each antenna in the  $N$ -element antenna array and the last  $N - 1$  beam filter outputs are fed into the Applebaum beamformer (see Chapter 5). Cyclostationary feature detector is then employed on the bandpass filtered Applebaum beamformer output. It is clear that the proposed method employs a 2-stage of array processing algorithms to increase the spatial selectivity, in turn, leading to improve SINR at the input to the feature detection algorithm. The SINR improvement obtained from the proposed architecture reflects as an improvement of the accuracy of the spectrum sensing and modulation detection algorithms.

### 6.2.1 FPGA Implementation of the Proposed Architecture

In order to analyze the hardware complexity required to gain the projected SINR improvement, proposed architecture is realized on Xilinx Virtex-6 XC6VSX475T 1FF1156 device for 64 element antenna array. Evaluation of hardware complexity and real time performance considered the following metrics: the number of used configurable logic blocks (CLB), flip-flop (FF) count, critical path delay ( $T_{cpd}$ ), and the maximum operating frequency ( $F_{max}$ ) in MHz. Results are shown in Table 6.1. In the Applebaum array, one complex multiplier (realized using Gauss multiplication algorithm which consumes three real multipliers and five adder/subtractors) is employed for each antenna to multiply the complex signal with the adaptive coefficient. Following the (6.2) proposed method require 6 real multipliers and 12 adder/subtractors per antenna (for both I and Q) to implement the 2-D IIR pre-filtering architecture.

### 6.2.2 Reduction of Side-lobe Levels and Main Beam Deviation

In the proposed approach, following the introduction of 2-D IIR beam filter, the complete system transfer function  $T_C(z_x, s_{ct})$  (from Chapter 5) is

$$T_C(z_x, s_{ct}) = \frac{1}{N} \sum_{l=0}^{N_A-1} \alpha'_l P(s_{ct}) \left[ R(s_{ct}) \sum_{k=0}^l Q(s_{ct})^k z_x^{-(k+1)} + 1 \right], \quad (6.3)$$

Insertion of the 2-D IIR beamfilter leads to a transfer function with both poles and zeros at guaranteed p-BIBO stability.

Improved spatial selectivity of the proposed array processing algorithm can be visualized by comparing the array factors. Array factor is calculated by assuming

Table 6.1: Hardware resource consumption using Xilinx Virtex-6 XC6VSX475T 1FF1156 device.

Architecture	CLB	FF	$T_{\text{cpd}}$ (ns)	$F_{\text{max}}$ (MHz)
Proposed	29136	105144	9.911	100.89

an array of 64 elements with input SINR of -10 dB. Fig. 6.2(b) shows the expected side-lobe level reduction capability where desired DOA  $\psi_d$  is  $30^\circ$  and Applebaum beamformer coefficients are calculated based on frequency 2.4 GHz. It is clear that the proposed 2-D IIR filter-based Applebaum adaptive arrays provide significant improvement in terms of side-lobe level reduction, which leads to a SINR improvement. Fig. 6.2 shows the deviation of the main beam due to the variation of the signal center frequency where Applebaum beamformer coefficients are calculated based on frequency 2.4 GHz. Reduced main beam deviation lead to alleviate the spectrum sensing over a wide range of frequencies around the pre-defined center frequency (which is used to calculate the coefficients). For the DOA  $30^\circ$ , proposed method shows a  $1^\circ$  deviation while the conventional method is  $1.5^\circ$ . It is clear the the proposed method exhibits a greater reduction in the beam direction deviation which is caused due to the wide-band nature of the introduced 2-D IIR beam filter.

### 6.2.3 Performance Evaluation of the Proposed Method

In order to measure the performance of the proposed directional spectrum sensing architecture, performance metric  $M$  is calculated utilizing two mean square error measurements  $M_A$  and  $M_P$ , which correspond to Applebaum-beamformer-only and

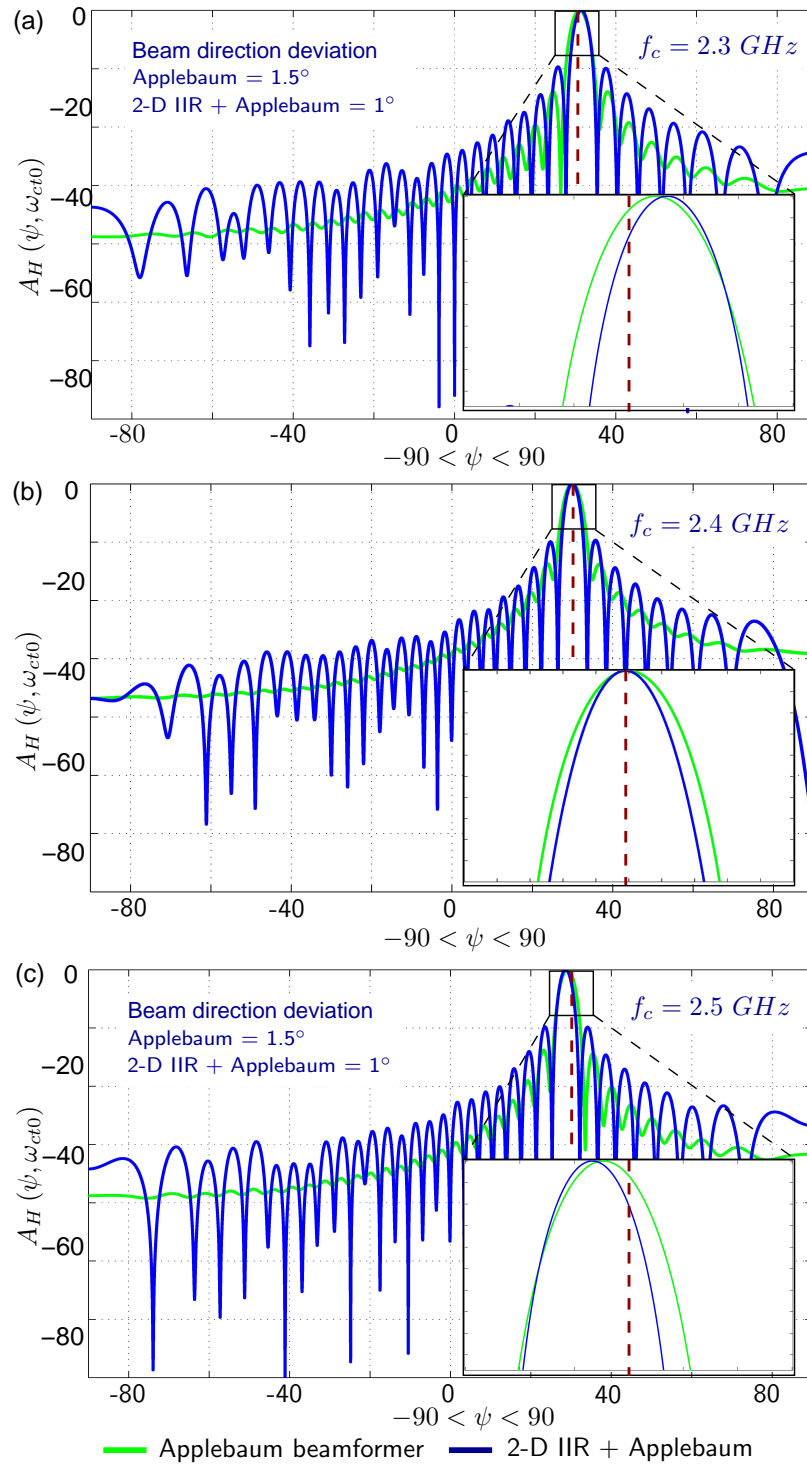


Figure 6.2: Deviation of the beam direction due to the variation of the center frequency (Applebaum coefficients are calculated for 2.4 GHz).

the proposed 2-D IIR filter based approach, respectively. Measurement  $M_A$  is the mean square error between the ideal SCF  $S_{y_I}^\alpha(f)$  of the signal with zero noise and the SCF  $S_{y_A}^\alpha(f)$  measured at the directionally enhanced output of the Applebaum beamformer (6.1(a)), where  $-0.5 \leq f \leq 0.5$  and  $-1 \leq \alpha \leq 1$ . It can be mathematically expressed as

$$M_A = \sum_{f=-0.5}^{0.5} \sum_{\alpha=-1}^1 |S_{y_I}^\alpha(f) - S_{y_A}^\alpha(f)|^2. \quad (6.4)$$

Note that  $M_A$  is a measure of how close the SCF calculated using Applebaum beamformer output to the ideal zero noise situation.  $M_A$  with smaller values are desired for accurate detection and sensing. Similarly,  $M_P$  can be expressed as the mean square error between the  $S_{y_I}^\alpha(f)$  and the SCF  $S_{y_P}^\alpha(f)$  measured at the beamformed output of the proposed beamforming architecture (6.1(b)).  $M_P$  is given by

$$M_P = \sum_{f=-0.5}^{0.5} \sum_{\alpha=-1}^1 |S_{y_I}^\alpha(f) - S_{y_P}^\alpha(f)|^2. \quad (6.5)$$

The performance metric  $M$  is then calculated as

$$M = 10 \log \left( \frac{M_A}{M_P} \right). \quad (6.6)$$

Since we are employing a bandpass filter prior to the cyclostationary feature detector in both architectures (Fig. 6.1(a) and (b)), performance metric  $M$  is a better measurement of the noise removing capability (in the interested frequency band) of proposed spectrum sensing architecture compared to the conventional method. Obtained improvement in terms of the performance metric  $M$  for different simulation scenarios is presented in section 6.3.

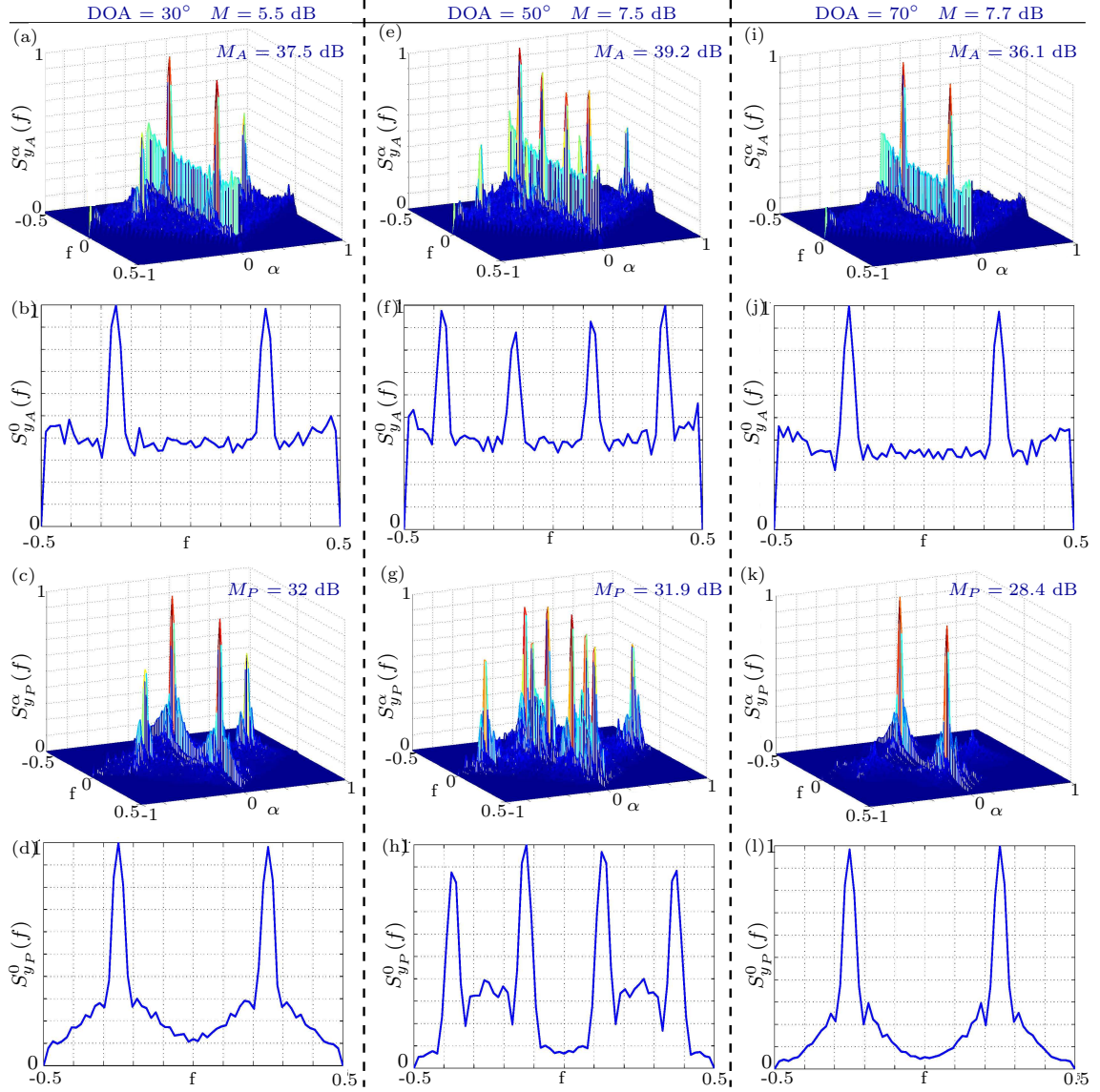


Figure 6.3: Obtained results for DOA  $20^\circ$  with  $-30$  dB SINR (a) SCF (b) PSD ( $\alpha = 0$  in the SCF) of the conventional method, (c) SCF (d) PSD of the proposed method. Results for DOA  $40^\circ$  with  $-30$  dB SINR (e) SCF (f) PSD of the conventional method, (g) SCF (h) PSD of the proposed method. Results for DOA  $60^\circ$  with  $-30$  dB SINR (i) SCF (j) PSD of the conventional method, (k) SCF (l) PSD of the proposed method.

### 6.3 Spectrum Sensing Simulations and Results

Numerical simulations are carried out to demonstrate the performance enhancement of the proposed directional spectrum sensing architecture, where frequency band in

between 2.3 GHz and 2.5 GHz is selected for spectrum sensing and 3 dB cutoff frequencies of the bandpass filter are selected accordingly. Apperbaum beamformer coefficients are calculated based on the center frequency 2.4 GHz. Three BPSK modulated signal sources with center frequencies 2.4 GHz, 2.3 GHz and 2.5 GHz are placed at DOA  $20^\circ$ ,  $40^\circ$  and  $40^\circ$ , respectively. QPSK modulated source is located at DOA  $60^\circ$ .

We assume that the source DOAs have already been estimated by employing a direction estimation algorithm. Obtained SCF  $S_{y_A}^\alpha(f)$  and PSD  $S_{y_A}^0(f)$  ( $\alpha = 0$  line of the SCF) for DOA  $20^\circ$  are shown in Fig. 6.3 (a) and (b) for conventional method and corresponding graphs for the proposed 2-D IIR filter based approach are shown in Fig. 6.3 (c) and (d). Similarly, calculated results for the DOA  $40^\circ$  and  $40^\circ$  are shown in Fig. 6.3 (e-h) and Fig. 6.3 (i-l) respectively. Noise reduction capability of the proposed method is clearly visualized in the obtained SCF and PSD and corresponding measurement values  $M_A$  and  $M_P$  also reflect the projected improvement in noise suppression. This unique feature of the proposed method will lead to enhance the accuracy and reliability of both spectrum sensing and modulation detection.

In order to evaluate the performance of the proposed spectrum sensing method in terms of the metric  $M$ , BPSK modulated signal with fractional bandwidth 1% and center frequency 2.4 GHz is assumed. Metrics  $M_A$  and  $M_P$  are obtained by varying the input SNR value and desired beam direction  $\psi_d$ . Fig. 6.4(a) shows the results for input SNR values -10 dB, -20 dB and -30 dB, where each graph is plotted with respect

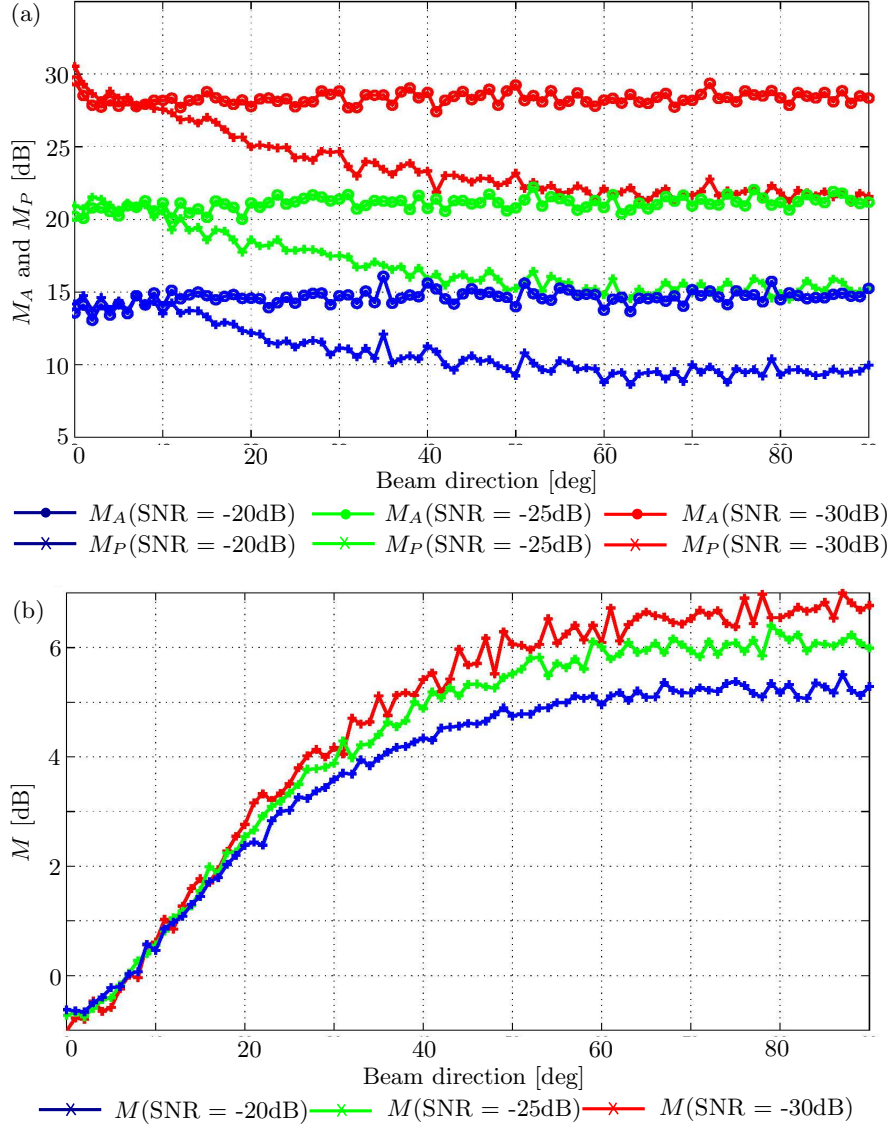


Figure 6.4: (a) Resulted  $M_A$  and  $M_P$  metric values for different SNR situations with respect to the desired beam direction. (b) Variation of the performance metric  $M$  with the input SNR.

to the beam direction  $0 \leq \psi \leq \pi/2$ . Fig. 6.4(b) shows the variation of the calculated performance metric  $M$  for each input SNR values. It shows that the performance improvement of the proposed method increases with the beam direction and decreases with input SNR value. These results show that the proposed method is desired for

spectrum sensing and modulation detection in very poor SINR environments. For example, spectrum sensing of a signal with 1% FB in a -30 dB SNR environment shows a 10 dB improvement compared to the conventional method. Resulted performance improvement is significant when compared to the implementation and operational complexity of the hardware required to obtain the same improvement.

#### 6.4 Conclusions

A novel array processing architecture is proposed for increasing the accuracy and reliability of directional spectrum sensing and modulation detection in cognitive radio networks. Proposed direction sensing and feature detection scheme employs a linear antenna array equipped with a conventional Applebaum adaptive beamformer and a recently proposed 2-D IIR planar-resonant beam filter to obtain improved spatial selectivity. Proposed beamforming architecture shows a significant improvement in SINR when the DOA of the desired signal is off-axis from the broad side direction. For example, when the desired signal is at  $40^\circ$  from broadside, the proposed system lead to an additional 8 dB improvement in the SINR compared to a similar system with a traditional Applebaum adaptive array which will lead to enhance the accuracy of the spectrum sensing operation. Performance metric which quantify the noise suppression capability of the cycostationay estimator, exhibits more than 3 dB improvement compared to the conventional architecture for very low SNR environments.

## CHAPTER VII

### BEAM-ENHANCEMENT OF RECTANGULAR APERTURE DIGITAL STAP BEAMFORMERS USING PARTIALLY-SEPARABLE 3-D IIR BEAM FILTERS

Applications of the rectangular aperture beamforming techniques can be found in many emerging areas ranging from wireless/mobile communication [27], radar [64], radio astronomy [65], and cognitive radio [66] for enhancement of the desired signal from a particular DOA while eliminating interferences and random noise. SIR improvement at the output of the beamformer (compared to the input) quantify the performance of the system where number of antenna elements in the array mainly determine the upper limit for the SIR improvement. In this chapter, a novel architecture to enhance the directivity of the FFT based STAP beamformer is proposed by introducing a 3-D IIR digital recursive filter architecture to the existing system as shown in Fig. 7.1. Proposed system modify the zero-manifold-only transfer function of the STAP beamformer by introducing complex-pole manifolds from the 3-D IIR beamfilter which will result a transfer function with both zeros and complex-poles manifolds. Manifold change in the proposed system reflect as a reduction in the side lobe levels which leads to an enhancement of the output SIR. Proposed architectural modification can be made without any significant change to the existing system and is able to implement with a marginal increase in the hardware complexity.

## 7.1 System Overview

Consider an uniform rectangular antenna array oriented in  $x - y$  plane with  $N_x \times N_y$  antenna elements (with same omnidirectional characteristics) as shown in Fig. 7.1, where inter antenna spacing are  $\Delta x$  and  $\Delta y$  for  $x$  and  $y$  directions, respectively. Output of each antenna element is sent through a low noise amplifier, bandpass filter prior to the ADC which samples the signal in every  $\Delta T$  seconds, where sampling frequency  $F_s = \frac{1}{\Delta T}$ . Plane wave  $w(x, y, ct) = w_s(\sin \psi \cos \phi x + \sin \psi \sin \phi y + ct)$  receiving from a DOA  $(\psi, \phi)$  is sampled at each antenna to obtain 3-D discrete signal  $w(n_x, n_y, n_{ct})$

$$w(n_x, n_y, n_{ct}) = w_s(\sin \psi \cos \phi \Delta x n_x + \sin \psi \sin \phi \Delta y n_y + c\Delta T n_{ct}), \quad (7.1)$$

where  $\psi$  is the elevation angle,  $\phi$  is the azimuth angle,  $ct$  is the time normalized by the speed of the wave  $c$ , and  $w_s(t)$  is the transmitted signal from the signal source. Recall from Chapter 2 that the ROS of the 3-D plane wave can be determined by taking the Fourier transform of  $w(n_x, n_y, n_{ct})$ . *MD signal processing theory proves that the ROS of the plane wave receiving from DOA  $(\psi, \phi)$  is confined to straight line in the  $(\omega_x, \omega_y, \omega_{ct}) \in \mathbb{R}^3$  3-D frequency domain which is passing through the origin, has an angle  $\theta$  to the  $\omega_{ct}$  axis and an angle  $\phi$  to  $\omega_x$  axis. Here  $\tan \theta = \sin \psi$  [18].* The equation of the ROS line is given by

$$\frac{\omega_x}{\sin \theta \cos \phi} + \frac{\omega_y}{\sin \theta \sin \phi} + \frac{\omega_{ct}}{\cos \theta} = 0. \quad (7.2)$$

Thus, wideband beamformer necessitates to have a line shaped passband described by Eq. 7.2 to selectively enhance plane waves from DOA  $(\psi, \phi)$ .

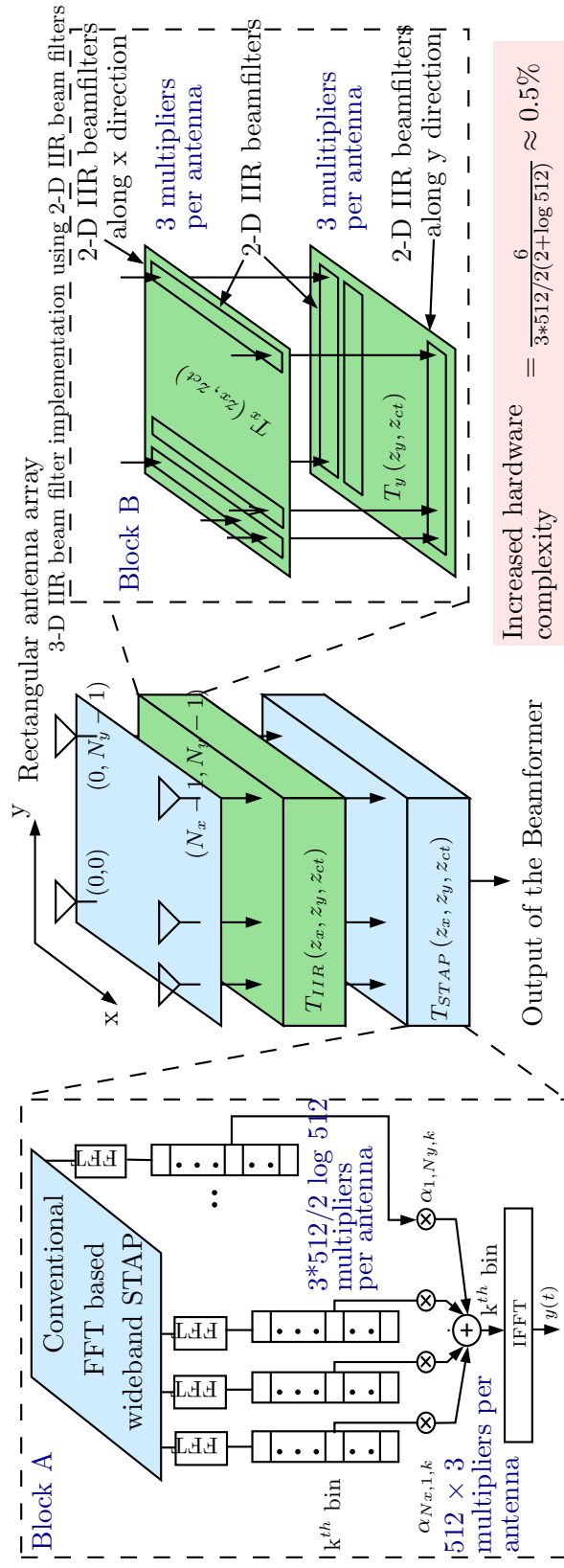


Figure 7.1: Overview of the proposed architecture to enhance the directivity of the rectangular aperture digital STAP beamformer.

### 7.1.1 FFT based Wideband STAP - Block A

$\mathbf{z}$  domain transfer function  $T_{PA_{3D}}(z_x, z_y, z_{ct})$  of the ST narrowband phased array operating at frequency  $\omega_{ct0}$  can be expressed as

$$T_{PA_{3D}}(z_x, z_y, z_{ct}) = \sum_{n_y=0}^{N_y-1} \sum_{n_x=0}^{N_x-1} \alpha_{N_x-n_x-1, N_y-n_y-1} z_x^{-n_x} z_y^{-n_y} \quad (7.3)$$

where  $\alpha_{n_x, n_y} = e^{-j\omega_{ct0}\Delta_{xy}T}$  and  $\Delta_{xy}T = \frac{1}{c}(\sin\psi \cos\phi\Delta x n_x + \sin\psi \sin\phi\Delta y n_y)$  is the time taken for plane wave to travel from origin of the  $x - y$  plane to any antenna position  $(n_x, n_y)$ . Note that the  $T_{PA_{3D}}$  has only zero manifolds in the transfer function.

The wideband FFT based STAP beamformer is a frequency domain beamforming technique [27, 26]. As shown in Fig. 7.1 block A, P-point FFT is employed at each of the inputs to obtain signals correspond to each frequency bin  $W(n_x, n_y, \omega_{ct_i})$ , where  $\omega_{ct_i} = \frac{2\pi}{P}i$ ,  $P/2 \leq i \leq P/2-1$ . Collectively, outputs correspond to the same frequency bin result a system similar to the narrowband phased array. Thus each frequency bin correspond to  $\omega_{ct_i}$  is multiplied using the complex phasor  $e^{-j\omega_{ct_i}c\Delta_{xy}T}$  (delay the signal with proper time). Phased rotated signals correspond to same frequency bin  $\omega_{ct_i}$  are then summed to feed into the IFFT block. Directionally enhanced output  $y(n_{ct})$  can be obtained at the output of the IFFT block. Note that the system has multiple inputs and a single output. Since the wideband FFT based STAP beamformer is an extension of the narrowband phased array beamformers described by Eq. 7.3, the complete system can be considered as FIR filter based beamformer which contains only zeros manifolds in the  $\mathbf{z}$ - domain transfer function  $H_{STAP}(z_x, z_y, z_{ct})$ .

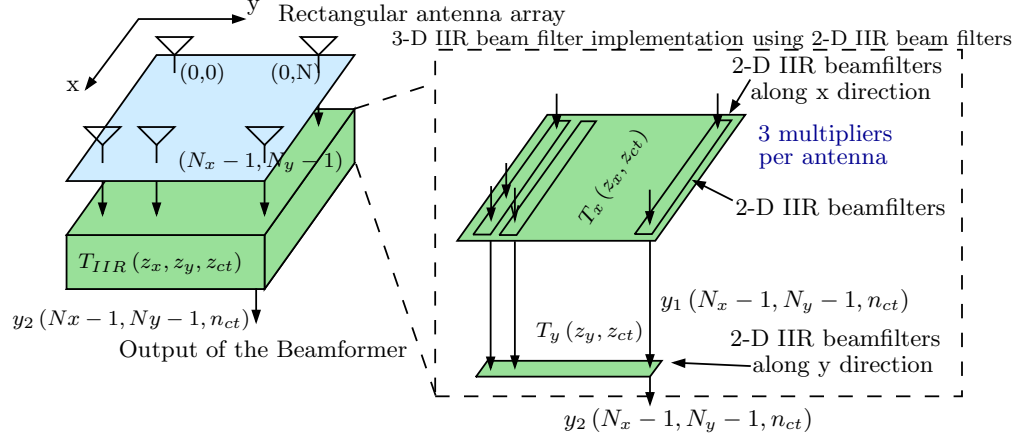


Figure 7.2: System architecture of the partially-separable 3-D IIR beam filter.

### 7.1.2 ST Network Resonant Partially-Separable 3-D IIR Beamfilter

Resistively terminated passive prototype networks also known as Ramamoorthy-Bruton networks (RBN) based on the concept of network resonance allows synthesis of low-complexity wideband beamformers which are IIR in nature [18]. 2-D beam filters have been proposed to enhance signals using an ULA where the beam filter exhibits a beam-shaped passband in the  $(\omega_x, \omega_{ct}) \in \mathbb{R}^2$  spatio-temporal frequency domain (antenna array is oriented at  $x$  direction). Prior to the introduction of the operation in Block B in the proposed system, the concept of the partially separable 3-D IIR beam filter which is realized using 2-D IIR beam filters is illustrated. Consider a  $\mathbf{z}$  domain transfer function of the first order 2-D IIR beam filter [18, 19]

$$T_x(z_x, z_{ct}) = \frac{(1 + z_x^{-1})(1 + z_{ct}^{-1})}{1 + b_{10_x} z_x^{-1} + b_{01_x} z_{ct}^{-1} + b_{11_x} z_x^{-1} z_{ct}^{-1}} \quad (7.4)$$

where coefficients  $b_{ij_x} = \frac{R + (-1)^i L_x + (-1)^j L_{ct_x}}{R + L_x + L_{ct_x}}$ .  $L_x, L_{ct_x}$  values and  $R$  value set the angular orientation and sharpness of the passband of the beam, respectively. Here  $z_x$  and  $z_{ct}$

variables correspond to spatial dimension  $x$  and time dimension  $ct$ . Note that 7.4 does not take into account the number of antennas in the array and is applicable only if the antenna array is infinite or the antenna array is sufficiently enough to stabilize its impulse response.

Since the rectangular aperture can be considered as an array of  $N_x$ -element ULAs oriented in  $x$  direction (has  $N_y$  such ULAs) as shown in Fig. 7.2, the underlining transfer function for each ULA can be evaluated using

$$L_x = -\cos[\tan^{-1}(\sin \psi \cos \phi)] \quad L_{ct_x} = \sin[\tan^{-1}(\sin \psi \cos \phi)], \quad (7.5)$$

which leads to a planar-shaped passband in  $(\omega_x, \omega_y, \omega_{ct}) \in \mathbb{R}^3$  as shown in Fig. 7.3(a).

Similarly, rectangular array can be considered as an array of  $N_y$ -element ULAs oriented in  $y$  direction (has  $N_x$  such ULAs) and the transfer function

$$T_y(z_y, z_{ct}) = \frac{(1 + z_y^{-1})(1 + z_{ct}^{-1})}{1 + b_{10_y}z_y^{-1} + b_{01_y}z_{ct}^{-1} + b_{11_y}z_y^{-1}z_{ct}^{-1}} \quad (7.6)$$

can be evaluated by calculating the coefficients  $b_{ij_y} = \frac{R+(-1)^i L_y + (-1)^j L_{ct_y}}{R+L_y+L_{ct_y}}$  using

$$L_y = -\cos[\tan^{-1}(\sin \psi \sin \phi)] \quad L_{ct_y} = \sin[\tan^{-1}(\sin \psi \sin \phi)]. \quad (7.7)$$

This leads to a planar-shaped passband as shown in Fig. 7.3(b). Beam shaped passband in  $(\omega_x, \omega_y, \omega_{ct})$  space-time frequency domain which is passing through the origin, has an angle  $\theta$  to the  $\omega_{ct}$  axis and has an angel  $\phi$  to  $\omega_x$  axis (as shown in Fig. 7.3(c)) can be obtained by cascading two systems, where  $\tan \theta = \sin \phi$ . Thus the combined transfer function can be expressed as

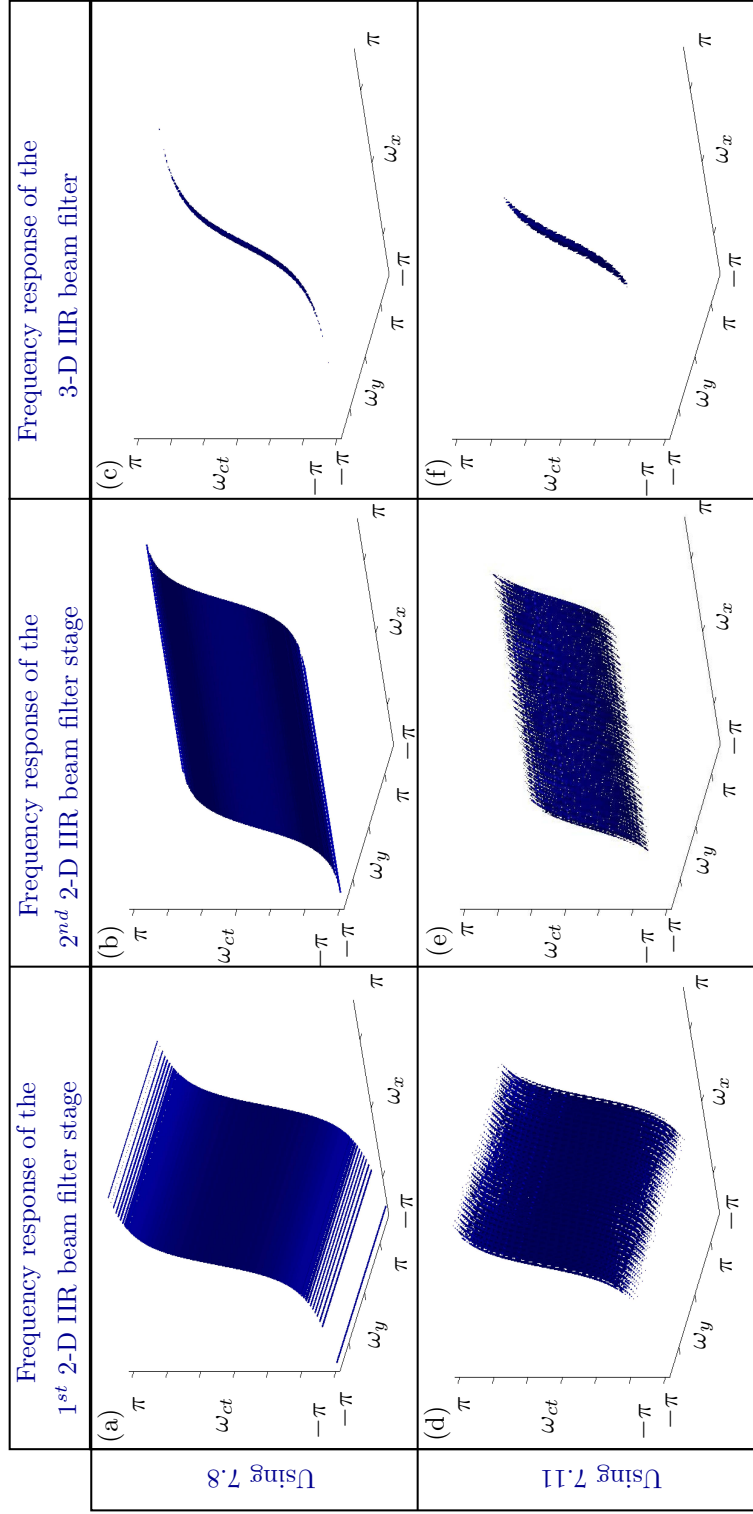


Figure 7.3: Frequency response of the array of 2-D IIR beam filters oriented in (a)  $x$  direction (b)  $y$  direction (c) Frequency response of the 3-D IIR beam filter [cascade two systems in (a) and (b)]. Here desired DOA is set to be  $(40^\circ, 45^\circ)$ .

$$T_{IIR}(z_x, z_y, z_{ct}) = \frac{(1 + z_x^{-1})(1 + z_{ct}^{-1})}{(1 + b_{10x}z_x^{-1} + b_{01x}z_{ct}^{-1} + b_{11x}z_x^{-1}z_{ct}^{-1})} \times \frac{(1 + z_y^{-1})(1 + z_{ct}^{-1})}{(1 + b_{10y}z_y^{-1} + b_{01y}z_{ct}^{-1} + b_{11y}z_y^{-1}z_{ct}^{-1})}. \quad (7.8)$$

However, note that (7.8) does not take into account the number of antenna elements in the array.

System architecture of the partially separable 3-D IIR beam filter is shown in Fig. 7.2 for a rectangular antenna array with  $N_x \times N_y$  antenna elements and digitized input signals  $w_a(n_x, n_y, n_{ct})$  where  $0 \leq n_x \leq N_x - 1$  and  $0 \leq n_y \leq N_y - 1$  are the antenna indexes in  $x$  and  $y$  directions, respectively. Recall from Chapter 3 that the array size dependent  $\mathbf{z}$  domain transfer functions  $T_x(z_x, z_y, z_{ct})$

$$T_x(z_x, z_y, z_{ct}) = P_x(z_{ct}) \left[ R_x(z_{ct}) \sum_{k=0}^{N_x-2} Q_x(z_{ct})^k z_x^{-(k+1)} + 1 \right] \quad (7.9)$$

and  $T_y(z_x, z_y, z_{ct})$

$$T_y(z_x, z_y, z_{ct}) = P_y(z_{ct}) \left[ R_y(z_{ct}) \sum_{k=0}^{N_y-2} Q_y(z_{ct})^k z_y^{-(k+1)} + 1 \right] \quad (7.10)$$

can be used to obtain the array size dependent transfer function for the 3-D IIR beam filter where  $P_x(z_{ct}) = \frac{1+z_{ct}^{-1}}{1+b_{01x}z_{ct}^{-1}}$ ,  $Q_x(z_{ct}) = \frac{-(b_{10x}+b_{11x}z_{ct}^{-1})}{1+b_{01x}z_{ct}^{-1}}$ ,  $R_x(z_{ct}) = 1 + Q_x(z_{ct})$ ,  $P_y(z_{ct}) = \frac{1+z_{ct}^{-1}}{1+b_{01y}z_{ct}^{-1}}$ ,  $Q_y(z_{ct}) = \frac{-(b_{10y}+b_{11y}z_{ct}^{-1})}{1+b_{01y}z_{ct}^{-1}}$  and  $R_y(z_{ct}) = 1 + Q_y(z_{ct})$ . During the actual implementaion, directionally enhanced outputs  $y_1(N_x - 1, n_y, n_{ct})$  (last output of the ULA) of each 2-D IIR beam filters in the first stage (2-D IIR beam filters are oriented in  $x$  direction), where  $0 \leq n_y \leq N_y - 1$ , are utilized to feed the final 2-D IIR beam filter oriented in  $y$  direction as shown in Fig. 7.2. All other outputs

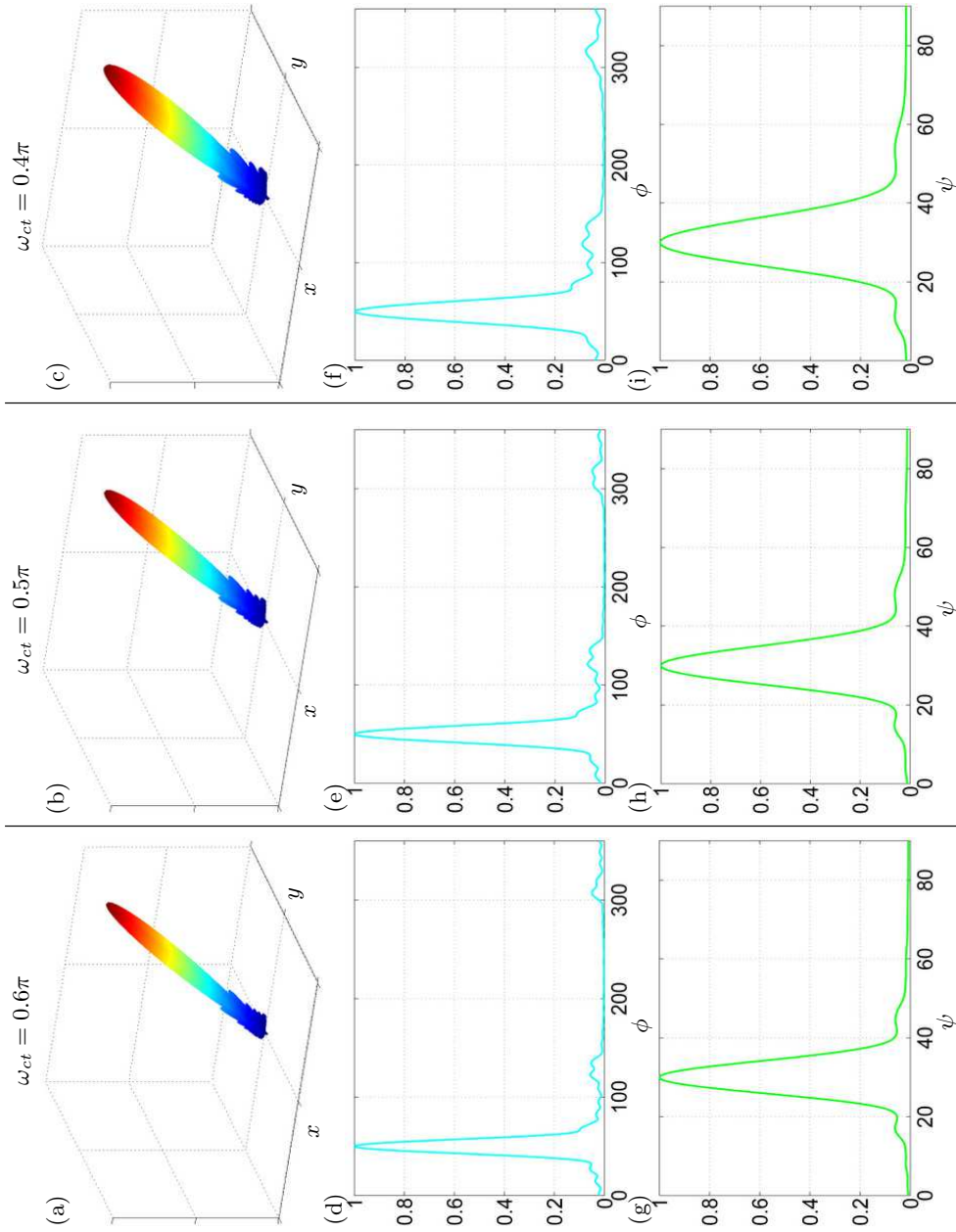


Figure 7.4: Array factor variation of the 3-D IIR beam filter with the normalized temporal frequencies (a)  $\omega_{ct0} = 0.6\pi$ , (b)  $\omega_{ct0} = 0.5\pi$  and (c)  $\omega_{ct0} = 0.4\pi$  (d-f) Array factor variation with respect to  $\psi$  while keeping the  $\phi$  unchanged. (g-i) Array factor variation with respect to  $\phi$  while keeping the  $\psi$  unchanged.

$y_1(n_x, n_y, n_{ct})$  are terminated, where  $0 \leq n_x \leq N_x - 2$  and  $0 \leq n_y \leq N_y - 1$ . Then the total transfer function can be expressed as

$$T_{IIR}(z_x, z_y, z_{ct}) = \frac{Y(z_x, z_y, z_{ct})}{W(z_x, z_y, z_{ct})} = P_x(z_{ct}) \left[ R_x(z_{ct}) \sum_{k=0}^{N_x-2} Q_x(z_{ct})^k z_x^{-(k+1)} + 1 \right] \\ \times P_y(z_{ct}) \left[ R_y(z_{ct}) \sum_{k=0}^{N_y-2} Q_y(z_{ct})^k z_y^{-(k+1)} + 1 \right]. \quad (7.11)$$

Directionally enhanced output can be obtained at  $y_2(N_x - 1, N_y - 1, n_{ct})$  and other outputs are terminated.

The array factor produced by  $T_{IIR}(z_x, z_y, z_{ct})$  is obtained by evaluating the 3-D frequency response  $T_{IIR}(e^{j\omega_x}, e^{j\omega_y}, e^{j\omega_{ct}})$  in (7.11) at a given temporal frequency  $\omega_{ct0}$  as function of the elevation angle  $\psi$  and azimuth angle  $\phi$  by setting  $\omega_x = \omega_{ct0} \sin \psi \cos \phi$  and  $\omega_y = \omega_{ct0} \sin \psi \sin \phi$  where  $\sin \phi = \tan \theta$  [46]. The array factor is given by  $A_{T_{IIR}}(\psi, \phi, \omega_{ct0}) = |T_{IIR}(e^{j\omega_{ct0} \sin \psi \cos \phi}, e^{j\omega_{ct0} \sin \psi \sin \phi}, e^{j\omega_{ct0}})|$ . Fig. 7.4(a-c) show the array factor variation of the 3-D IIR beam filter with the normalized temporal frequencies  $\omega_{ct0} = 0.6\pi$ ,  $\omega_{ct0} = 0.5\pi$  and  $\omega_{ct0} = 0.4\pi$  where desired beam direction is  $\phi = 50^\circ$  and  $\psi = 30^\circ$  and antenna array is  $32 \times 32$  element. Fig. 7.4 (d-f) and (g-i) show the array factor variation of  $\phi$  when  $\psi$  is fixed at  $30^\circ$  and variation of  $\psi$  when  $\phi$  is fixed at  $50^\circ$ .

When analyzing the hardware complexity of the proposed partially separable 3-D IIR wideband beamformer, 3 real multipliers and 6 adders/subtractors per antenna are required to evaluate the underlining 2-D difference equation for the beam

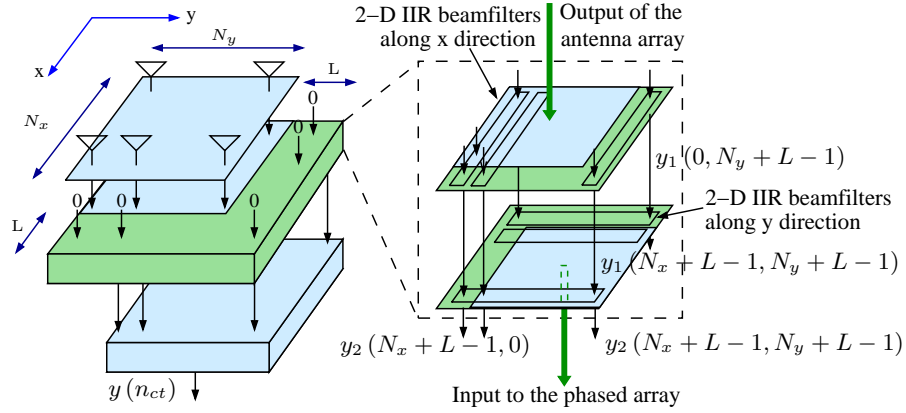


Figure 7.5: Modification of the beam filter to further enhance the directivity.

filters oriented in  $x$  direction. For the final beam filter (in  $y$  direction) requires  $3N_y$  multipliers and  $6N_y$  adders, in total, for the calculation. Thus the total system requires  $3N_y(N_x + 1)$  real multipliers and  $6N_y(N_x + 1)$  adders/subtractors for the digital realization.

## 7.2 Proposed Beam-Enhancement Architecture - Block B

Note that the 3-D IIR beam filter discussed the previous section accepts multiple inputs ( $N_x \times N_y$ ) and produces multiple outputs ( $N_x \times N_y$ ), unlike the conventional FFT based STAP, where it only produces a single output. In the proposed architecture, each output of the first filtering stage of the 3-D IIR beam filter (2-D IIR beam filters oriented in  $x$  direction) is used to feed the second filtering stage which has  $N_x N_y$ -element ULAs oriented in  $y$  direction as shown in Fig. 7.5. Thus in the proposed architecture,  $N_x \times N_y$  outputs produced by the 3-D IIR beam filter are fed into the

STAP beamformer. Here, 3-D IIR beam filter act as a pre-filter to the conventional STAP as shown in Fig. 7.1. Introduction of the 3-D IIR beam filter changes the zero-manifold-only transfer function of the STAP to a transfer function with both zero and complex-pole manifolds. This change leads to a directivity enhancement of the conventional FFT based STAP. In order to further improve the system performance, modification to the beam filtering architecture is proposed by exploiting the IIR nature of the beam filter which evaluate the transfer functions  $T_x(z_x, z_{ct})$  and  $T_y(z_y, z_{ct})$  for additional  $L$  steps (per each direction) where each of the extra inputs are fed with zeros as shown in Fig. 7.5.  $N_x \times N_y$  antenna outputs are fed into the uppermost inputs of the 3-D IIR beam filter and the last  $N_x \times N_y$  outputs are then fed into the FFT based STAP beamformer.

In order to obtain the array size dependent  $\mathbf{z}$  domain transfer function of the proposed architecture (in closed form), first consider an ULA oriented in  $x$  direction with  $N_x$  number of antennas and  $L$  additional inputs which are fed by zeros. The mixed domain expression of the 2-D IIR beam filter (see Chapter 3)

$$Y_m(n_x, z_{ct}) = P_x(z_{ct})W_m(n_x, z_{ct}) + P_x(z_{ct})W_m(n_x - 1, z_{ct}) + Q_x(z_{ct})Y_m(n_x - 1, z_{ct}), \quad (7.12)$$

with  $P_x(z_{ct}) = \frac{1+z_{ct}^{-1}}{1+b_{01_x}z_{ct}^{-1}}$ ,  $Q_x(z_{ct}) = \frac{-(b_{10_x}+b_{11_x}z_{ct}^{-1})}{1+b_{01_x}z_{ct}^{-1}}$  and  $R_x(z_{ct}) = 1 + Q_x(z_{ct})$  leads to

$$\begin{aligned}
Y_m(0, z_{ct}) &= P_x(z_{ct}) W_m(0, z_{ct}) \\
Y_m(1, z_{ct}) &= P_x(z_{ct}) [W_m(1, z_{ct}) + W_m(0, z_{ct}) R_x(z_{ct})] \\
Y_m(2, z_{ct}) &= P_x(z_{ct}) \left[ W_m(2, z_{ct}) + W_m(1, z_{ct}) R_x(z_{ct}) \right. \\
&\quad \left. + W_m(0, z_{ct}) Q_x(z_{ct}) R_x(z_{ct}) \right] \\
Y_m(3, z_{ct}) &= P_x(z_{ct}) \left[ W_m(3, z_{ct}) + W_m(2, z_{ct}) R_x(z_{ct}) \right. \\
&\quad \left. + W_m(1, z_{ct}) Q_x(z_{ct}) R_x(z_{ct}) + W_m(0, z_{ct}) Q_x(z_{ct})^2 R_x(z_{ct}) \right] \\
&\vdots \\
Y_m(N-1, z_{ct}) &= P_x(z_{ct}) \left[ W_m(N-1, z_{ct}) + W_m(N-2, z_{ct}) R_x(z_{ct}) \right. \\
&\quad \left. + W_m(N-2, z_{ct}) Q_x(z_{ct}) R_x(z_{ct}) + \dots \right. \\
&\quad \left. + W_m(0, z_{ct}) Q_x(z_{ct})^{N-2} R_x(z_{ct}) \right] \\
Y_m(N, z_{ct}) &= P_x(z_{ct}) R_x(z_{ct}) \left[ W_m(N-1, z_{ct}) + W_m(N-2, z_{ct}) Q_x(z_{ct}) \right. \\
&\quad \left. + W_m(N-3, z_{ct}) Q_x(z_{ct})^2 + \dots \right. \\
&\quad \left. + W_m(0, z_{ct}) Q_x(z_{ct})^{N-2} \right] \\
Y_m(N+1, z_{ct}) &= P_x(z_{ct}) Q_x(z_{ct}) R_x(z_{ct}) \left[ W_m(N-1, z_{ct}) + W_m(N-2, z_{ct}) \right. \\
&\quad \left. Q_x(z_{ct}) + W_m(N-3, z_{ct}) \right. \\
&\quad \left. Q_x(z_{ct})^2 + \dots + W_m(0, z_{ct}) Q_x(z_{ct})^{N-2} R_x(z_{ct}) \right] \\
&\vdots
\end{aligned}$$

$$Y_m(N+L-1, z_{ct}) = P_x(z_{ct}) Q_x(z_{ct})^{L-1} R_x(z_{ct}) \left[ W_m(N-1, z_{ct}) + W_m(N-2, z_{ct}) \right. \\ \left. Q_x(z_{ct}) + W_m(N-3, z_{ct}) \right. \\ \left. Q_x(z_{ct})^2 + \dots + W_m(0, z_{ct}) Q_x(z_{ct})^{N-2} R_x(z_{ct}) \right]$$

which represent the mixed domain expressions for each beam filter outputs  $y(n_x, n_{ct})$  where  $0 \leq n_x \leq N+L-1$ . Following the inverse Fourier transform,  $\mathbf{z}$  domain representations  $Y(z_x, z_{ct}) z_x^{-(N+L-1-n_x)}$  of each output  $y(n_x, n_{ct})$  ( $0 \leq n_x \leq N+L-1$ ) of the beam filter can be expressed in the matrix form  $Y = A_x W$  where,

$$A_x = P_x(z_{ct}) = \begin{bmatrix}
1 & 0 & 0 & 0 & 0 & 0 & 0 & 0 & 0 & 0 & 0 \\
R_x(z_{ct}) & 1 & 0 & 0 & 0 & 0 & 0 & 0 & 0 & 0 & 0 \\
Q_x(z_{ct})R_x(z_{ct}) & R_x(z_{ct}) & 1 & 0 & 0 & 0 & 0 & 0 & 0 & 0 & 0 \\
Q_x(z_{ct})^2R_x(z_{ct}) & Q_x(z_{ct})R_x(z_{ct}) & R_x(z_{ct}) & 1 & 0 & 0 & 0 & 0 & 0 & 0 & 0 \\
\cdot & \cdot \\
\cdot & \cdot \\
Q_x(z_{ct})^{N-2}R_x(z_{ct}) & Q_x(z_{ct})^{N-3}R_x(z_{ct}) & \cdot & \cdot & \cdot & R_x(z_{ct}) & 1 & 0 & 0 & 0 & 0 \\
Q_x(z_{ct})^{N-1}R_x(z_{ct}) & Q_x(z_{ct})^{N-2}R_x(z_{ct}) & \cdot & \cdot & \cdot & Q_x(z_{ct})R_x(z_{ct}) & R_x(z_{ct}) & 0 & 0 & 0 & 0 \\
Q_x(z_{ct})^NR_x(z_{ct}) & Q_x(z_{ct})^{N-1}R_x(z_{ct}) & \cdot & \cdot & \cdot & Q_x(z_{ct})^2R_x(z_{ct}) & Q_x(z_{ct})R_x(z_{ct}) & 0 & 0 & 0 & 0 \\
\cdot & 0 & 0 & 0 & 0 \\
\cdot & 0 & 0 & 0 & 0 \\
Q_x(z_{ct})^{N+L-2}R_x(z_{ct}) & Q_x(z_{ct})^{N+L-3}R_x(z_{ct}) & \cdot & \cdot & \cdot & Q_x(z_{ct})^{L-2}R_x(z_{ct}) & Q_x(z_{ct})^{L-1}R_x(z_{ct}) & 0 & 0 & 0 & 0
\end{bmatrix}, \tag{7.13}$$

$$Y = \left[ z_x^{-(N+L-1)} \ z_x^{-(N+L-2)} \ z_x^{-(N+L-3)} \ \dots \ z_x^{-1} \ z_x^0 \right]^T Y(z_x, z_{ct}) \quad (7.14)$$

is the  $\mathbf{z}$  domain representation of the outputs and

$$W = \left[ z_x^{-(N+L-1)} \ z_x^{-(N+L-2)} \ z_x^{-(N+L-3)} \ \dots \ z_x^{-1} \ z_x^0 \right]^T W(z_x, z_{ct}) \quad (7.15)$$

is the  $\mathbf{z}$  domain representation of the input vector  $W$ .

Now, consider an antenna array with  $N_x \times N_y$  elements and  $L$  additional inputs per each direction as shown in Fig. 7.5. The  $\mathbf{z}$  domain representation of the inputs can be expressed in the matrix form as

$$\begin{aligned}
W = & \left[ \begin{array}{cccccccc}
z_x^{-(N_x+L-1)} z_y^{-(N_y+L-1)} & z_x^{-(N_x+L-1)} z_y^{-(N_y+L-2)} & \dots & \dots & \dots & 0 & 0 & z_x^{-(N_x+L-1)} z_y^0 \\
z_x^{-(N_x+L-2)} z_y^{-(N_y+L-1)} & z_x^{-(N_x+L-2)} z_y^{-(N_y+L-2)} & \dots & \dots & \dots & 0 & 0 & z_x^{-(N_x+L-2)} z_y^0 \\
\cdot & \cdot & \dots & \dots & \dots & 0 & 0 & 0 \\
\cdot & \cdot & \dots & \dots & \dots & 0 & 0 & 0 \\
z_x^{-(N_x-1)} z_y^{-(N_y+L-1)} & z_x^{-(N_x-1)} z_y^{-(N_y+L-2)} & \dots & \dots & \dots & 0 & 0 & z_x^{-(N_x-1)} z_y^0 \\
\cdot & \cdot & \dots & \dots & \dots & 0 & 0 & 0 \\
\cdot & \cdot & \dots & \dots & \dots & 0 & 0 & 0 \\
\cdot & \cdot & \dots & \dots & \dots & 0 & 0 & 0 \\
\cdot & \cdot & \dots & \dots & \dots & 0 & 0 & 0 \\
\cdot & \cdot & \dots & \dots & \dots & 0 & 0 & 0 \\
z_x^0 z_y^{-(N_y+L-1)} & z_x^0 z_y^{-(N_y+L-2)} & \dots & \dots & \dots & z_x^0 z_y^{-(N_y+L-2)} & z_x^0 z_y^{-(N_y+L-1)} & z_x^0 z_y^0
\end{array} \right] W(z_x, z_{ct}).
\end{aligned}$$

where  $W$  is a  $(N_x + L) \times (N_y + L)$  matrix. Then the  $\mathbf{z}$  domain representation matrix  $Y_1$  of the outputs at the first stage of the 3-D IIR beam filter (2-D IIR beam filters oriented in  $x$  direction) can be obtained as a  $(N_x + L) \times (N_y + L)$  matrix

$$Y_1 = A_x W \quad (7.17)$$

According to Chapter 5, 2-D IIR beam filter requires  $N_{2D} = 1$  spatial steps to stabilize the transient response of the numerator part of the 2-D IIR beam filter where  $N_{2D}$  is the order of the numerator function of the 2-D IIR beam filter. Thus the outputs  $y_1(1, n_y, n_{ct})$  where  $0 \leq n_y \leq N_y + L - 1$ , are terminated and only remaining outputs are processed at the second filtering stage which consisting with 2-D IIR beam filters oriented in  $y$  direction. Let the corresponding  $(N_x + L - 1) \times (N_y + L)$  matrix as  $Y'_1$ . It can be shown that the  $\mathbf{z}$  domain representation matrix  $Y_2$  of the outputs at the 3-D IIR beam filter can be expressed as

$$Y_2 = (A_y Y_1'^T)^T \quad (7.18)$$

where

$$A_y = P_y(z_{ct}) \begin{bmatrix}
1 & 0 & 0 & 0 & 0 & 0 & 0 & 0 & 0 & 0 \\
R_y(z_{ct}) & 1 & 0 & 0 & 0 & 0 & 0 & 0 & 0 & 0 \\
Q_y(z_{ct}) R_y(z_{ct}) & R_y(z_{ct}) & 1 & 0 & 0 & 0 & 0 & 0 & 0 & 0 \\
Q_y(z_{ct})^2 R_y(z_{ct}) & Q_y(z_{ct}) R_y(z_{ct}) & R_y(z_{ct}) & 1 & 0 & 0 & 0 & 0 & 0 & 0 \\
\cdot & \cdot \\
\cdot & \cdot \\
Q_y(z_{ct})^{N-2} R_y(z_{ct}) & Q_y(z_{ct})^{N-3} R_y(z_{ct}) & \cdot & \cdot & \cdot & R_y(z_{ct}) & 1 & 0 & 0 & 0 \\
Q_y(z_{ct})^{N-1} R_y(z_{ct}) & Q_y(z_{ct})^{N-2} R_y(z_{ct}) & \cdot & \cdot & \cdot & Q_y(z_{ct}) R_y(z_{ct}) & R_y(z_{ct}) & 0 & 0 & 0 \\
Q_y(z_{ct})^N R_y(z_{ct}) & Q_y(z_{ct})^{N-1} R_y(z_{ct}) & \cdot & \cdot & \cdot & Q_y(z_{ct})^2 R_y(z_{ct}) & Q_y(z_{ct}) R_y(z_{ct}) & 0 & 0 & 0 \\
\cdot & 0 & 0 & 0 \\
\cdot & 0 & 0 & 0 \\
Q_y(z_{ct})^{N+L-2} R_y(z_{ct}) & Q_y(z_{ct})^{N+L-3} R_y(z_{ct}) & \cdot & \cdot & \cdot & Q_y(z_{ct})^{L-2} R_y(z_{ct}) & Q_y(z_{ct})^{L-1} R_y(z_{ct}) & 0 & 0 & 0
\end{bmatrix} \quad (7.19)$$

$A_y = P_y(z_{ct})$

$T$  represents the transpose operation and  $Y_2$  is a  $(N_x + L - 1) \times (N_y + L)$  matrix. Similar to the previous stage, outputs  $y_2(n_x, 1, n_{ct})$  where  $0 \leq n_x \leq N_x + L - 2$ , are terminated due to the stability requirement of the filter. Thus the corresponding output matrix  $Y_2'$  at the output of the 3-D IIR beam filter has dimensions  $(N_x + L - 1) \times (N_y + L - 1)$ . If  $L = 0$ ,  $(N_x - 1) \times (N_y - 1)$  outputs of the beam filter are sent to the STAP beamformer, otherwise if  $L \geq 1$ , last  $N_x \times N_y$  outputs  $y_2(n_x, n_y, n_{ct})$  where  $L \leq n_x \leq N_x + L - 1$  and  $L \leq n_y \leq N_y + L - 1$  are fed into the STAP beamformer. The final transfer function of the proposed system for  $L \geq 1$  can be expressed as

$$T(z_x, z_y, z_{ct}) = \sum_{n_x=0}^{N_x-1} \sum_{n_y=0}^{N_y-1} H_{n_x, n_y}(z_{ct}) Y_2'(n_x, n_y) \quad (7.20)$$

where  $H_{n_x, n_y}(z_{ct})$  is the filter transfer function corresponding to the antenna branch  $(n_x, n_y)$  of the STAP beamformer and  $Y_2'(n_x, n_y)$  is the matrix element at  $(n_x, n_y)$  index of the  $Y_2'$  matrix. For the narrowband case  $H_{n_x, n_y}(z_{ct}) = \alpha_{N_x - n_x - 1, N_y - n_y - 1}$  and

$$T(z_x, z_y, z_{ct}) = \sum_{n_x=0}^{N_x-1} \sum_{n_y=0}^{N_y-1} \alpha_{N_x - n_x - 1, N_y - n_y - 1} Y_2'(n_x, n_y) \quad (7.21)$$

where  $\alpha_{n_x, n_y} = e^{-j\omega_{ct}0\Delta_{xy}T}$  and  $\Delta_{xy}T = \frac{1}{c}(\sin\psi \cos\phi\Delta x n_x + \sin\psi \sin\phi\Delta y n_y)$ .

In order to compare the hardware complexity of the proposed system with the 512-point FFT based STAP beamformer, consider the complexity of a single antenna. FFT based STAP requires  $\frac{3}{2}512 \log_2 512 = 6912$  real multipliers for the FFT calculations and  $512 \times 3$  real multipliers for the phase rotation where as 3-D IIR beam filter requires 6 multipliers per antenna (3 multipliers per each beam filter). The

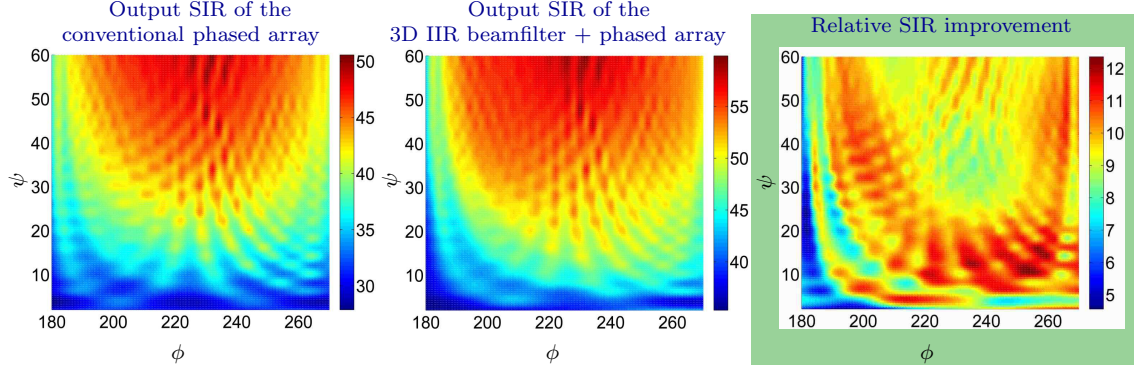


Figure 7.6: SIR improvement of the proposed architecture compared to the digital STAP beamformer.

proposed beam enhanced spate-time beam filter realization increases the hardware complexity only by 0.5%, compared to the existing system, to obtain reduced sidelobe levels for the same array size. In order to increase the array size, which is also an option to enhance the directivity, require at least 6912 additional real multiplier per each antenna (require hardware components for the RF front-end as well), which consumes much more hardware than the proposed method.

### 7.3 Simulated Directivity Improvement Results

Directivity enhancement of the proposed architecture has verified through time domain simulations and SIR measurements. Consider a  $64 \times 64$  rectangular antenna array oriented in  $x - y$  plane. Gaussian modulated cosine signals with 15% fractional bandwidth (wideband) and  $0.5\pi$  center frequency is utilized for the simulation where input SIR value is set to be -20 dB. Additional number of steps  $L$  of the 3-D IIR beamfiler is chosen as 8, since the particular selection provides the maximum improvement in terms of SIR.

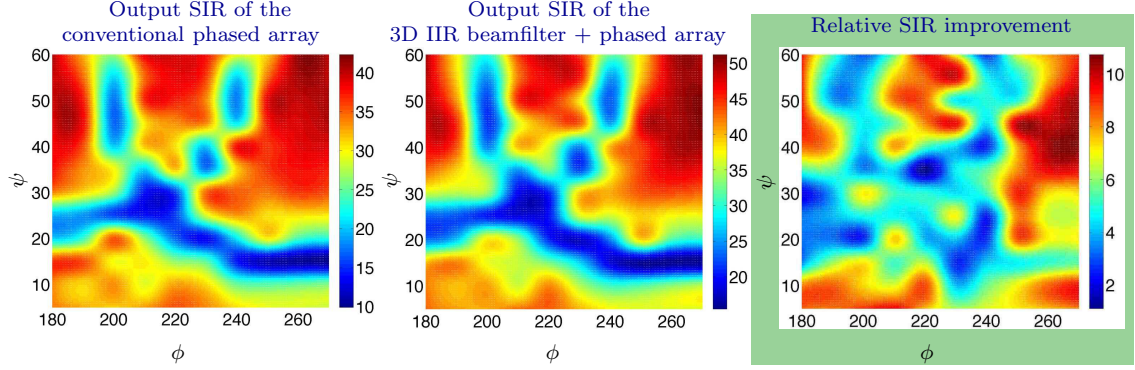


Figure 7.7: SIR improvement of the proposed architecture compared to the digital STAP beamformer.

Two simulation scenarios with different interference settings are presented to determine the projected SIR improvement of the proposed architecture. Fig. 7.6 (a-c) shows the SIR improvement of the STAP beamformer, proposed architecture, and relative improvement compared to the conventional STAP, respectively, where measurements are obtained for the region  $0^\circ \leq \psi < 60^\circ$  and  $180^\circ \leq \phi < 270^\circ$ . Two interferences are located at  $\psi = 20^\circ, \phi = 40^\circ$  and  $\psi = 80^\circ, \phi = 20^\circ$ . Simulated results show a maximum improvement of 12.1 dB, minimum improvement of 4.6 dB, and average SIR improvement of 9.4 dB. Fig. 7.7 (a-c) depict the similar results for a situation where interferences are located at  $\psi = 50^\circ, \phi = 120^\circ$  and  $\psi = 30^\circ, \phi = 300^\circ$ . Obtained results shows maximum improvement of 10.6 dB, minimum improvement of 2 dB and average improvement of 6.4 dB. Proposed beam enhancement rectangular array architecture provides a significant SIR improvements for the same array size with a marginal increase in the hardware complexity.

## 7.4 Conclusion

Architectural modification to the existing rectangular array STAP beamformer is proposed to enhance the directivity (SIR improvement). Network resonant ST 3-D IIR beam filter is employed as a pre-filter to the STAP beamformer. Partially separable architecture of the 3-D IIR beam filter is realized to minimize the hardware complexity. Introduction of the beam filter change the zero-manifold-only transfer function of the conventional beamformer to a transfer function with both zero and pole manifolds. Side lobe level rejection capability of the proposed architecture is shown in terms of the frequency response. Simulation results show better than 6 dB average SIR improvement along every direction for an environment with -20 dB input SIR. Realization of the proposed beam enhanced beamforming architecture marginally increase the hardware complexity ( $< 0.5\%$ ) while providing significant improvement in terms of SIR.

CHAPTER VIII  
ELECTRONICALLY STEERABLE DIRECTED ENERGY USING  
SPACE-TIME NETWORK RESONANT DIGITAL SYSTEMS

Antenna array transmit beamforming allows directed energy for radar, communications and target illumination. Directionality enhances the SNR at the receiver and enables interference rejection via spatial filtering. Applications of transmit beamforming includes array radar [67, 68] and mobile communications. Traditionally, wideband transmit beamforming arrays are realized using phased/timed arrays. In digital implementation, transmit arrays employ high-order FIR filters as phasing networks [69]. A transformative, novel alternative low-complexity approach that can realize wideband transmit arrays is proposed using MD network resonant filters. The proposed system achieves *an order of magnitude lower digital processing complexity* while supporting a wide range of frequencies (ideally from DC to Nyquist in the digital domain) by exploiting recursive spatial-temporal signal flow graphs (SFGs) of MD IIR filters. ULA examples for both single beam and multi-beam transmit beamforming are presented to illustrate the concept. Simulations demonstrate the space-time domain and 2-D frequency domain behavior of the transmit beamformer for example input signals.

## 8.1 Proposed Transmit Beamformer Model

MD network resonance enables synthesis of discrete domain transfer functions having directive frequency responses in the spatio-temporal frequency domain [18]. MD transfer functions having specific passband shapes in the frequency domain have been exploited to design p-BIBO stable receive beamformers [32]. For example, a 2-D IIR digital filter having a beam shaped passband in the 2-D frequency domain  $(\omega_x, \omega_{ct})$  can be used for electronically steerable beamforming [70]. Here,  $\omega_x$  and  $\omega_{ct}$  are the normalized frequency variables along spatial and temporal dimensions, respectively.

Following the reciprocity properties of MD passive networks, *we propose, for the first time in the literature, to employ 2-D planar-resonant filters in transmit-mode for RF directed energy aperture arrays.*

Fig. 8.1(a) depicts the overview of the transmit array for a ULAs based on a 2-D IIR space-time digital filter. The proposed 2-D IIR digital filter comprising of interconnected digital processing modules (see Fig. 8.1(a)) has the 2-D  $\mathbf{z}$ -transform domain transfer function

$$T(z_x, z_{ct}) = \frac{(1 + z_x^{-1})(1 + z_{ct}^{-1})}{1 + b_{10}z_x^{-1} + b_{01}z_{ct}^{-1} + b_{11}z_x^{-1}z_{ct}^{-1}} \quad (8.1)$$

where  $z_x$  and  $z_{ct}$  are the  $\mathbf{z}$ -transform variables along spatial and temporal dimensions, respectively. Here,  $z_x^{-1}$  implies a spatial delay (i.e. neighboring antenna) whereas  $z_{ct}^{-1}$  implies a temporal delay realized using clocked registers within the digital processing modules. Furthermore, the coefficients  $b_{ij} = \frac{R+(-1)^i \cos \theta + \sin \theta (-1)^j}{R + \cos \theta + \sin \theta}$  with

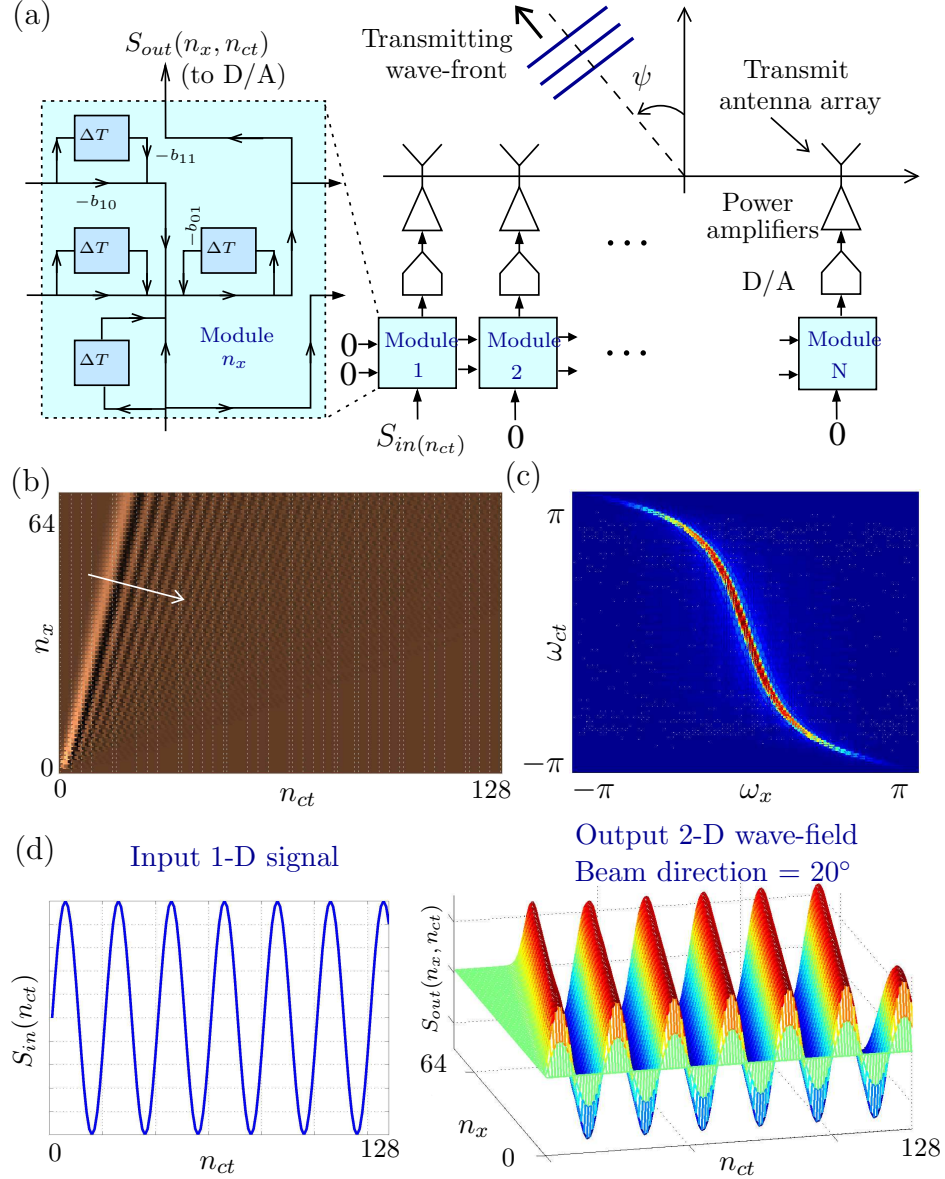


Figure 8.1: (a) Proposed 2-D IIR digital filter based transmit array. Spatio-temporal 2-D (b) impulse response and (c) frequency response of transmit array digital filter showing the directional response in the 2-D space-time domain. (d) Example 1-D sinusoidal input signal and output 2-D wave-field .

$b_{00} = 0$  [70] set the beam direction  $\psi$ , where  $\theta = \tan^{-1}(\sin \psi)$ . Free parameter  $R$  should approximately equal to zero to maintain high Q-factor. Transfer function (8.1) corresponds to the 2-D difference equation  $y(n_x, n_{ct}) = \sum_{p=0}^1 \sum_{q=0}^1 w(n_x - p, n_{ct} - q) -$

$\sum_{p=0}^1 \sum_{q=0}^1 b_{pq} y(n_x - p, n_{ct} - q)$ , leading to an interconnected array processing SFG shown in Fig. 8.1(a), where  $w(n_x, n_{ct})$  and  $y(n_x, n_{ct})$  are the 2-D discrete domain input and output, respectively.

To explain transmit mode beamforming, consider the 2-D impulse response of the filter obtained by setting  $w(n_x, n_{ct}) = \delta(n_x, n_{ct})$  in the difference equation, where  $\delta(n_x, n_{ct})$  is the 2-D dirac delta function. As shown in Fig. 8.1(b), the 2-D impulse response indicates the emission of a directed wave from the output of the 2-D IIR filter, where the direction of the wave-front is set by the coefficients  $b_{ij}$  in (8.1). Corresponding frequency domain output is shown in Fig. 8.1(c) which shows the directional response of the 2-D filter. Because any 1-D signal can be represented as a linear combination of weighted and delayed unit impulse signals, and (8.1) is a linear shift-invariant system, by exciting the first module in the array processor with a temporal intensity function  $S_{in}(n_{ct})$  a corresponding directed out-going wave-front can be obtained at the output of the 2-D IIR beam filter (see Fig. 8.1(a)).

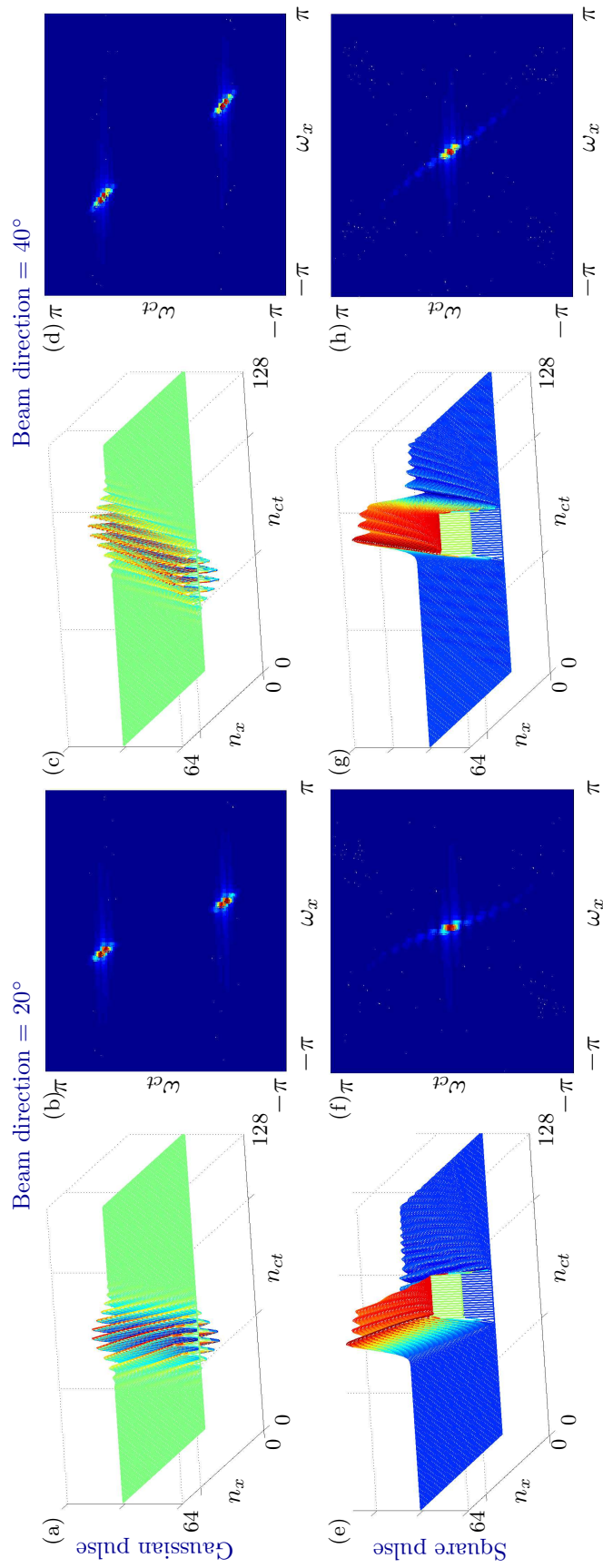


Figure 8.2: (a) 2-D output and (b) frequency response for a Gaussian modulated cosine input for  $20^\circ$ . (c) and (d) for  $40^\circ$ . (e) 2-D output and (f) frequency response for a square pulse input for  $20^\circ$ . (g) and (h) for  $40^\circ$ .

That is, we set  $w(1, n_{ct}) = S_{in}(n_{ct})$  and  $w(2 \leq n_x \leq N, n_{ct}) = 0$  and the resulting 2-D IIR filter output  $y(n_x, n_{ct})$  is sent through digital to analog converters (D/A) feeding power amplifiers (PAs). Fig. 8.1(d) shows sinusoidal excitation and the resulting directed RF waves for direction  $\psi = 20^\circ$ .

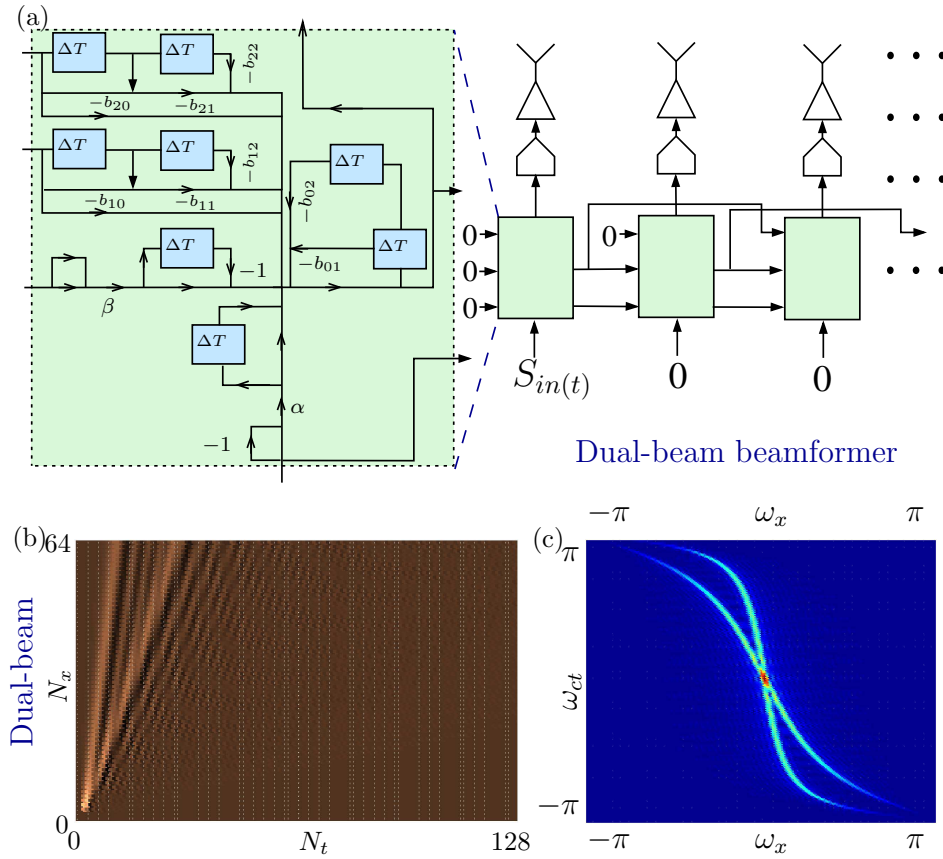


Figure 8.3: (a) Architecture for the dual-beam transmit beamformer (b) 2-D impulse response and (c) frequency response of the 2-beam transmit beamformer.

Another important capability of the proposed network resonant beamforming architecture is the ability of obtaining multiple beams without duplicating the single-beam system. For the dual beam case, a 2-D IIR digital transmit beamformer

architecture has the  $\mathbf{z}$ -transform domain transfer function [71]

$$H_B(z_x, z_{ct}) = \frac{\sum_{i=0}^2 \sum_{j=0}^2 a_{ij} z_x^{-i} z_{ct}^{-j}}{\sum_{p=0}^2 \sum_{q=0}^2 b_{pq} z_x^{-p} z_{ct}^{-q}} \quad (8.2)$$

where  $a_{ij}$  and  $b_{pq}$  are proposed in [71] with  $b_{00} = 0$ . Signal flow graph of the dual beam transmit beamformer, its space-time and frequency responses (beam directions are  $10^\circ$  and  $30^\circ$ ) are shown in Fig. 8.3(a) and 8.3(b-c) respectively.

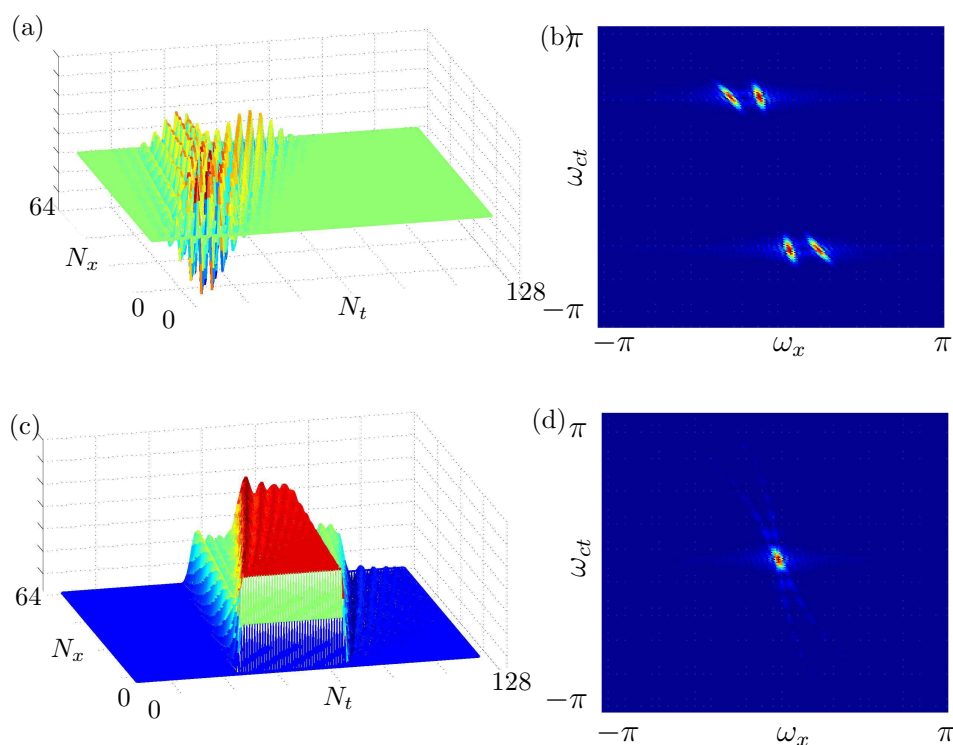


Figure 8.4: (a) 2-D output and (b) frequency response for a Gaussian modulated cosine input (c) 2-D output and (d) frequency response for a square pulse input for the dual-beam architecture.

## 8.2 Simulation Example

Fig.8.2 shows 2-D space-time domain and 2-D frequency domain transmit beamformer outputs for two choices of the temporal intensity function (i.e. input data)  $S_{in}(n_{ct})$  and two different beam directions. We consider a ULA of 64 elements and  $R$  is 0.001. Space-time response of a Gaussian-modulated cosine signal for beam directions  $20^\circ$  and  $40^\circ$  are shown in Fig. 8.2(a),(c) with their frequency responses in Fig. 8.2 (b) and (d). Corresponding results for a square pulse is shown in Fig. 8.2(e-h). Dual-beam space-time response for a Gaussian modulated signal and a square pulse are shown in Fig. 8.4(a),(c) with their frequency responses in Fig. 8.4 (b) and (d). Assuming 32-tap FIR filters in a typical digital transmit aperture, the proposed method reduces digital hardware to just 3 multipliers per antenna, leading to about 90.6% reduction in digital multiplier circuit complexity compared to traditional methods.

## 8.3 Conclusion

An electronically steerable digital wideband transmit-beamforming method based on space-time networkresonant infinite impulse response discrete systems is proposed for directed energy applications. The method leads to order of magnitude lower digital multiplier count compared to the FIR filter based transmit arrays. Both single- and dual-beam architectures are introduced. Simulation results demonstrate the space-time domain and 2-D frequency domain behavior of the proposed wideband transmit beamformer for different input signals.

## CHAPTER IX

### ADDITIONAL RESEARCH: TUNABLE MULTIBAND RF CMOS ACTIVE FILTER ARRAYS

The advent of cognitive radio and reconfigurable radar necessitates wideband RF receivers to support multiple standards. Microwave integrated-circuit (IC) realizations are important for such radio platforms that require multiple, precisely-defined passbands. There is an interest in reconfigurable filter arrays via “FPGAs” [72, 73], which may enable arbitrary RF filters with agile passband characteristics. However, the design of reconfigurable circuits that allow complete tunability in terms of number of passbands, their relative locations and quality factors, is challenging at microwave frequencies. With the growing demand for multi-band, portable RF devices, fully reconfigurable filters in an IC form factor are highly desirable. Traditionally, such tunable microwave filters have been realized using passive microwave circuits[74] and RF-microelectromechanical system (MEMS)[75].

This need for reconfigurable filters has been recognized by off-the-shelf component manufacturers [76] and by researchers [77, 78, 79]. A common approach to implementing an on-chip tunable filter is to tune inductors and/or capacitors of L-C networks [77]. The tuning of passive components is often accomplished by employing varactors: however inductor tuning can also be used[80] by using varactors or switches.

Recently, a new tunable bandpass filter architecture has been introduced, which explores the impedance-transformation property of passive mixing [78]. This approach is promising because it shifts the RF filter design challenges to the base-band circuits. However, the design complexity of the tunable multi-phase oscillator increases with this design.

In this chapter, an all-pass filter based-synthesis method for the RF-IC realization of multi-band analog bandpass filters is proposed. Proposed filters operate in small-signal mode and support independently tunable passbands (both center frequency and bandwidth) under digital control. The tunable analog filters use first-order all-pass networks  $\Phi(s) = \frac{1-sT/2}{1+sT/2}$  as a building block, that approximates an ideal delay of duration  $T$ . All-pass filter-based synthesis allows highly flexible tuning of center frequency and bandwidth of each passband, using a small number of control variables.

Fig. 9 shows the overview of the proposed bandpass filter, which employs scaling, summing, and all-pass filtering as building blocks. The filter requires the adjustment of a gain parameter  $k_1$  to tune the center frequency. Similarly, the bandwidths are tuned by adjusting another gain  $k_2$ . The synthesis starts from an available digital IIR bandpass filter prototype  $H_{bp}(z)$  that uses the tunable second-order all-pass filter  $A(z) = \frac{k_2+k_1(1+k_2)z^{-1}+z^{-2}}{1+k_1(1+k_2)z^{-1}+k_2z^{-2}}$  proposed by Vaidyanathan, Mitra and Regalia [81]. The digital prototype  $H_{bp}(z)$  [81] is reviewed here as  $H_{bp}(z) = 0.5(1 - A(z))$ , where  $k_1 = -\cos\omega_0$  (sets the center frequency) and  $k_2 = \frac{1-\tan(\Omega/2)}{1+\tan(\Omega/2)}$  (sets the bandwidth). The realization of a similar filter, albeit in the analog domain, requires the replace-

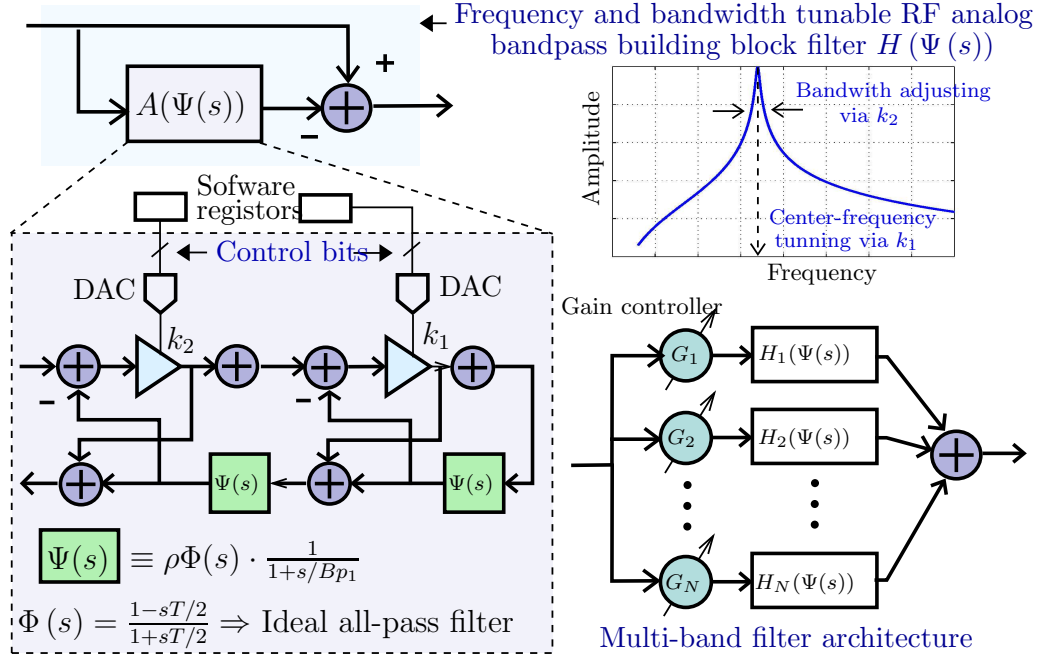


Figure 9.1: Overview of the proposed frequency-tunable bandwidth-adjustable RF analog bandpass filter, including a multi-band filter realization, to support multiple bands with different center frequencies and bandwidths.

ment of a sampled delay  $z^{-1}$  with a corresponding analog delay  $T$ , having a Laplace domain representation  $e^{-sT}$ . This *ideal* behavior is difficult, if not impossible, to achieve in practice – over GHz of bandwidth – using available RF-IC realization methods.

In this chapter, a first-order all-pass network,  $\Phi(s)$ , is employed in place of an ideal delay, with appropriate modifications to original digital prototype filter parameters,  $k_1$  and  $k_2$ , thereby allowing a close approximation to the desired response with a practical complementary metal-oxide semiconductor (CMOS) RF-IC implementation. Fig. 9 shows the SFG of the proposed analog bandpass filter derived using  $H_{bp}(z)$ . All-pass

filters ease the implementation of the SFG by employing variable gain current mirrors, which combine the required adders and variables  $k_1, k_2$  into one analog circuit cell. Digital reconfigurability may be achieved via control bit streams interfaced through digital to analog converters.

## 9.1 Tunable Analog RF Bandpass Filter Synthesis

### 9.1.1 Synthesis using Ideal All-Pass Filters

First, the synthesis of a single analog bandpass filter (for the  $k^{th}$  sub-band) is discussed in the multi-band configuration shown in Fig. 9. For the given center frequency  $\omega_c$  and bandwidth  $\Omega_c$  specifications, we consider the digital IIR prototype  $H_{bp}(z)$ , and subsequently replace  $z^{-1}$  terms with the ideal first-order all-pass transfer function  $\Phi(s)$  leading to

$$H_k^{ideal}(s) = 0.5 \left( 1 - \frac{k_2 + k_1(1 + k_2)\Phi(s) + [\Phi(s)]^2}{\underbrace{1 + k_1(1 + k_2)\Phi(s) + k_2[\Phi(s)]^2}_{A(\Phi(s))}} \right), \quad (9.1)$$

where  $k_1$  and  $k_2$  are the filter coefficients from the original digital prototype [81]. Due to the change of basis from a polynomial of  $z$  to a polynomial of  $\Phi(s)$ ,  $H_k^{ideal}(s)$  undergoes frequency warping (i.e. inverse bi-linear warping), which in turn, changes the center frequency and bandwidth from the original design specifications. Fig. 9.3(a) shows the magnitude frequency response of the digital prototype  $|H_{bp}(e^{j\omega})|$  for design specifications of center frequency  $f_c = 2.5$  GHz ( $\omega_c = 2\pi f_c$ ) and bandwidth  $B_c = 30$  MHz ( $\Omega_c = 2\pi B_c$ ), and  $|H_k^{ideal}(j\omega)|$  corresponding to (9.1) showing the cen-

ter frequency and bandwidth deviations due to all-pass delay approximation. The modification of the coefficients,  $k_1$  and  $k_2$ , is proposed to obtain  $k_{1c}$  and  $k_{2c}$ , respectively, given by

$$k_{1c} = \frac{(\omega_c T/2)^2 - 1}{(\omega_c T/2)^2 + 1} \quad (9.2)$$

$$k_{2c} = \frac{2((\omega_c T/2)^2 + 1) - \Omega_c T}{2((\omega_c T/2)^2 + 1) + \Omega_c T} \quad (9.3)$$

in order to compensate for the center frequency shift and bandwidth variation due to all-pass approximation  $\Phi(s)$  in (9.1). As shown in Fig. 9.3(b), with the new coefficients,  $k_{1c}$  and  $k_{2c}$ , the proposed  $H_k^{ideal}(s)$  provides exact center frequency and bandwidth as the original design specifications.

### 9.1.2 The Effect of Parasitic Low-Pass Poles

Despite the ideal all-pass behavior of  $\Phi(s)$ , practical realizations will be unavoidably subject to the effects of parasitic capacitance, which causes higher-order low-pass poles in the all-pass transfer function  $\Phi(s)$ . To accommodate such non-ideal effects in CMOS RF-ICs, each all-pass network is modeled as  $\Psi(s) = \rho\Phi(s) \cdot \frac{1}{1+s/B_{p1}}$ , where  $B_{p1}$  is a dominant low-pass pole and  $\rho$  is a non-ideal all-pass gain parameter (ideally  $\rho = 1$ ). For the  $k^{th}$  band in the multi-band configuration, the modified transfer function is obtained as

$$H_k(s) = 0.5 \left( 1 - \frac{k_{2c} + k_{1c}(1 + k_{2c})\Psi(s) + [\Psi(s)]^2}{\underbrace{1 + k_{1c}(1 + k_{2c})\Psi(s) + k_{2c}[\Psi(s)]^2}_{A(\Psi(s))}} \right), \quad (9.4)$$

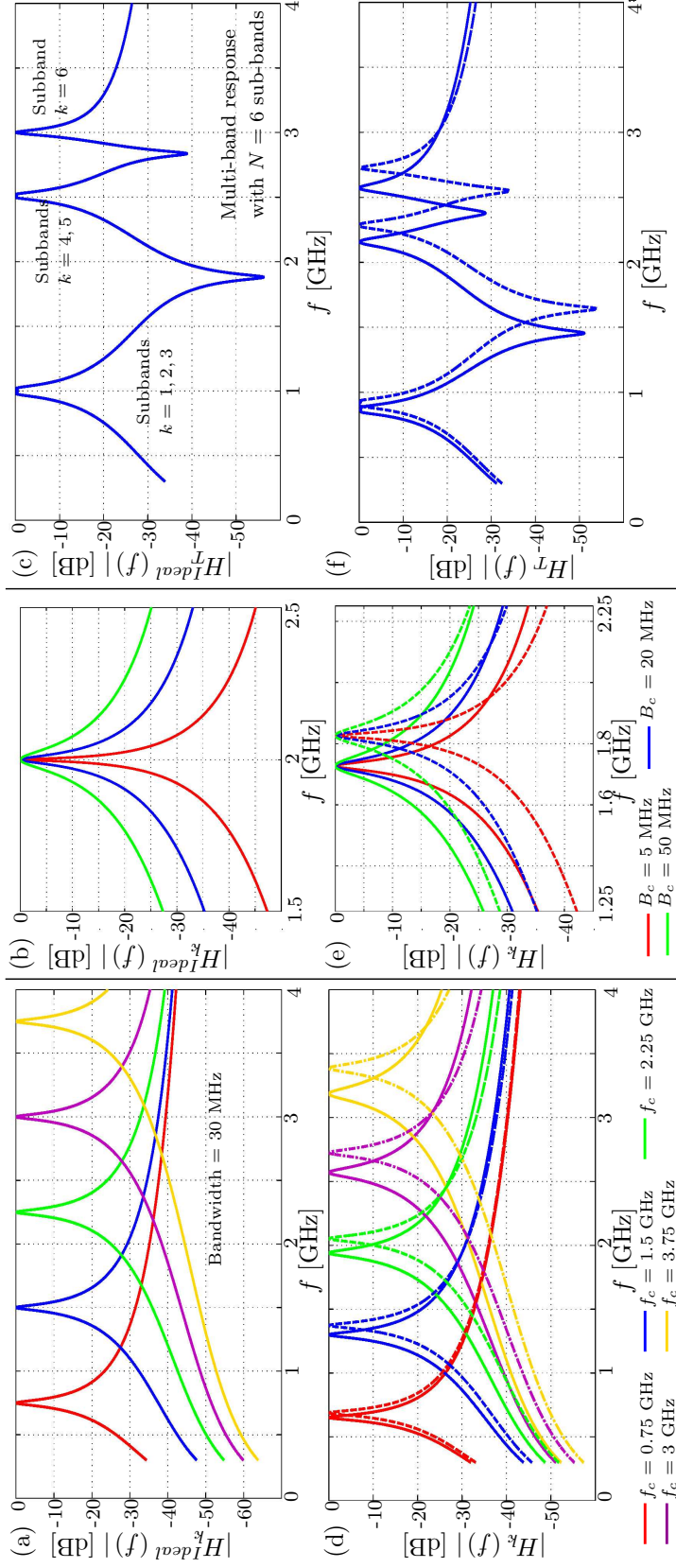


Figure 9.2: Magnitude frequency response  $|H_k^{ideal}(j\omega)|$  for (a) different center frequencies and (b) different bandwidths showing the frequency and bandwidth tunability. (c) Multi-band filter response from ideal all-pass model  $H_k^{ideal}(s)$  for  $N = 6$  bands. (d) frequency tunability, (e) bandwidth tunability, and (f) multi-band response, including the effect of low-pass parasitic pole at 27 GHz and 45 GHz (dashed).

which corresponds to the SFG shown in Fig. 9. Due to parasitic effects, frequency response,  $H_k(j\omega)$ , corresponding to (9.4) undergoes slight changes in the center frequency and bandwidth. The coefficients,  $k_{1c,2c}$ , in (9.3) can be modified to include the effect of the low-pass pole to compensate for such deviations, and it is reserved for future work.

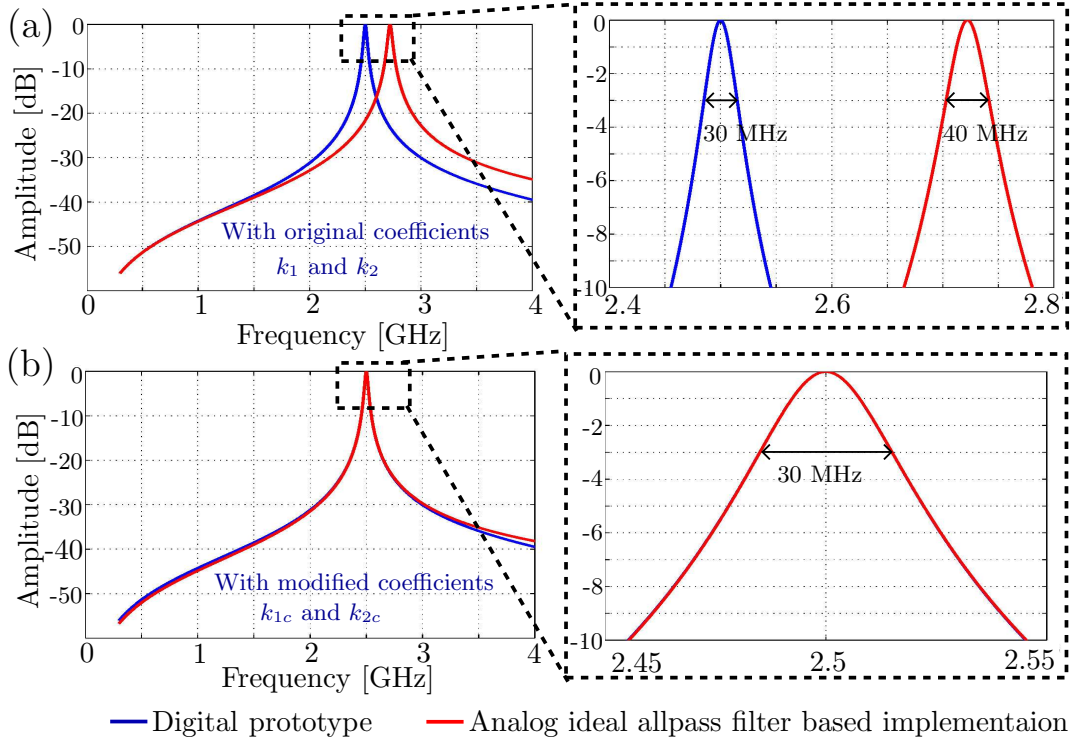


Figure 9.3: Magnitude frequency responses  $|H_{bp}(e^{j\omega})|$  and  $|H_k^{ideal}(j\omega)|$  with (a) original coefficients,  $k_{1,2}$ , in the digital prototype and (b) modified coefficients,  $k_{c1,c2}$ , which compensate the inverse bi-linear warping effect.

The realization of  $\Psi(s)$  using both current- and voltage-mode CMOS RF-IC implementations have been successfully completed [82, 83]. The availability of a current-mode CMOS all-pass filter  $\Psi(s)$  with  $T \approx 40$  ps and  $B_{p1} = 27$  GHz is

assumed. The 130-nm CMOS all-pass filter has been designed [82], fabricated and measured with aid of an RF probe station and vector network analyzer.

### 9.1.3 Multi-Band Filter Topology

As shown in Fig. 9, a filterbank configuration of  $H_k(s)$  for  $k = 1, 2, \dots, N$  is employed to produce a multi-band RF analog bandpass filter having the transfer function

$$H_T(s) = \sum_{i=k}^N G_k H_k(\Psi(s)), \quad (9.5)$$

where the gain controllers,  $G_k$ , in each sub-band are employed to maintain a constant gain in each of the passbands at the output of the filter bank. Note that each band,  $H_k(\Psi(s))$  of  $H_T(s)$ , is independently tunable for center frequency and bandwidth via the coefficients,  $k_{1c,2c}$ , leading to highly-agile multi-passband RF analog filter architecture. This property will become important for emerging radio front-ends and RF-FPGA fabrics, which are expected to work with different communication standards simultaneously.

## 9.2 Closed-Form Filter Response

Transfer functions  $H_k^{ideal}(j\omega)$ ,  $H_k(j\omega)$ , and  $H_T(j\omega)$  are examined using all-pass group delay  $T \approx 40$  ps and two choices for the low-pass pole at 27 GHz and 45 GHz. These parameters were selected based on the available current-mode CMOS all-pass filter.

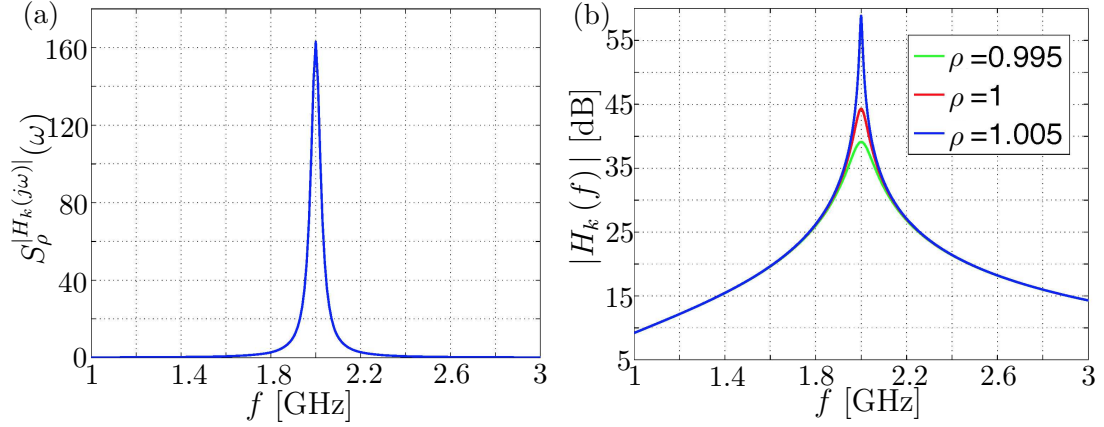


Figure 9.4: First order sensitivity function  $S_p^{|H_k(j\omega)|}(\omega)$  for a center frequency of 2 GHz. (b) Bandpass filter response with non-ideal all-pass gain  $\rho$ .

### 9.2.1 Frequency and Bandwidth Tunability

Achieving a wide range of tunability in both center frequency and bandwidth is the key expectation of the proposed scheme. Fig. 9.2(a) and (b) show the magnitude frequency response of the ideal realization  $|H_k^{ideal}(j\omega)|$  for different center frequencies in the range of 0-4 GHz and different bandwidths, respectively. Fig. 9.2(c) shows the multi-band response for 6 sub-bands using  $H_k^{ideal}(s)$ , where the sub-bands  $k = 1, 2, 3$  are centered around 1 GHz,  $k = 4, 5$  are centered around 2.5 GHz, and  $k = 6$  is centered at 3 GHz, with equal 30 MHz bandwidth. As an alternative approach to bandwidth tuning, one can employ a set of equally selective sub-band filters with closely located center frequencies to produce highly selective tunable passbands over a frequency range with a sharp pass-to-stop band transition. This is illustrated in Fig. 9.2(c) for  $k = 1, 2, 3$  sub-bands. Fig. 9.2(d) shows the magnitude response  $|H_k(j\omega)|$  depicting the center frequency tunability for low-pass pole located at 27 GHz

and 45 GHz. Similarly, for a given center frequency, bandwidth tunability via  $k_{2c}$  is shown in Fig. 9.2(e). The multi-band filter response  $|H_T(j\omega)|$ , including the effect of low-pass parasitic pole, is shown in Fig. 9.2(f).

## 9.2.2 Transfer Function Sensitivity to All-Pass Gain

Due to the parasitic effects, the magnitude response of the all-pass network  $\Psi(s)$  deviates from its ideal unity gain response as a function of frequency. Therefore, in a multi-band configuration, the sub-band filters,  $H_k(s)$ , require gain controllers,  $G_k$ , to adjust for the non-ideal gain fluctuations. With respect to the non-ideal all-pass gain  $\rho$ , the first order sensitivity function  $S_\rho^{|H_k(j\omega)|}(\omega) = \text{Re} \left[ \frac{\partial H_k(j\omega)}{\partial \rho} \frac{\rho}{H_k(j\omega)} \right]$  quantifies the gain variation of the bandpass filter as a function of frequency [84]. Fig. 9.4(a) shows  $S_\rho^{|H_k(j\omega)|}(\omega)$  for center frequency of 2 GHz. Fig. 9.4(b) shows the bandpass filter gain variation for varying  $\rho$ . High sensitivity allows fast tuning with small control voltages, but also requires precise calibration, and perhaps a feedback mechanism to maintain operating points.

## 9.3 Response with CMOS All-Pass Simulation

### 9.3.1 First-Order Current-Mode CMOS All-Pass Filter

The current-mode all-pass filter, used in this work, was first described in [82]. The targeted pole/zero frequency of the filter was 10 GHz, and therefore, only a few number of active components were allowed to reduce the number of parasitic poles.

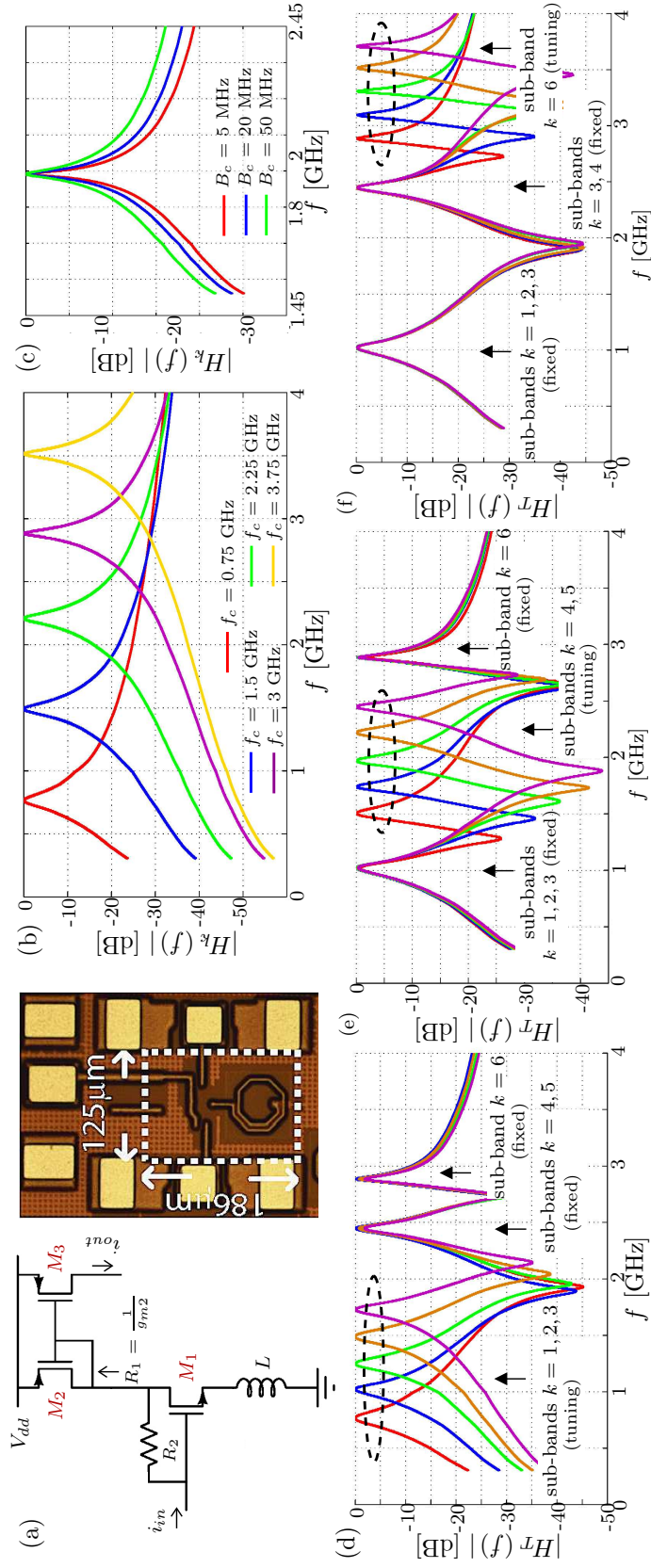


Figure 9.5: (a) Schematic and layout of the current-mode CMOS all-pass filter. (b) center frequency and (c) bandwidth tunability of the bandpass filter computed using CMOS all-pass response. (d)-(f) N=6 multi-band filter response computed using CMOS response, which shows the independent tunability of each sub-band.

With this constraint, an inductive source-degenerated topology was adopted (see Fig. 9.5(a)). The output current is taken with a current mirror ( $M_2$ - $M_3$ ), which presents resistance,  $R_1$ , at the metal-oxide-semiconductor field-effect transistor drain node. The current-mirror allows cascading of the filter.  $R_2$  provides gate biasing, which extends the all-pass frequency response to DC, and permits the cascading of multiple stages without the need of level shifters.

### 9.3.2 Frequency Response Simulations

Measured frequency response of the 130-nm CMOS current-mode all-pass filter shown in Fig. 9.5(a) is used to compute the frequency response of the proposed bandpass filter,  $H_k(s)$ , and the multi-band configuration,  $H_T(s)$ , for  $N=6$  bands. Figs. 9.5(b) and (c) show the single band response  $|H_k(j\omega)|$  for tunable center frequency and bandwidth, respectively, computed by replacing  $\Psi(s = j\omega)$  in (9.4) with measured data from the all-pass RF-IC circuit. Figs. 9.5(d)-(f) show the multi-band filter response, showing the ability of independent tuning of each sub-band. For example, Fig. 9.5(d) shows a scenario where sub-bands  $k = 5, 4$  are fixed around 2.5 GHz, sub-band  $k = 6$  is fixed around 3 GHz while sub-bands  $k = 1, 2, 3$  are tuned for five different center frequencies. Similarly Figs. 9.5(e) and (f) show independent tuning of sub-bands  $k = 4, 5$  and  $k = 6$ , respectively, for five different center frequencies.

## 9.4 Conclusions

Frequency and bandwidth agile, multi-passband analog filter array is proposed towards potential applications in emerging “RF-FPGA” type reconfigurable radio front-ends. The proposed analog filter is based on a novel transfer function synthesis technique employing first-order all-pass filters. Independent tunability of center frequency and bandwidth are achieved via two closed-form filter coefficients that compensate for inverse bi-linear frequency warping effect caused by all-pass filter synthesis. The frequency response and tunability of the proposed multi-band filter is verified up to 4 GHz using available measured data from a 130-nm current-mode CMOS all-pass filter. Future work includes modification of filter coefficients to include parasitic low-pass effects, investigation of transfer function sensitivity to filter coefficients, and CMOS RF-IC circuit design of the proposed analog SFG.

## CHAPTER X

### CONCLUSION AND FUTURE WORK

#### 10.1 Conclusion

The research presented in this thesis explores the characteristics of network-resonant beam digital filters, such as low hardware and computational complexity, wideband nature, MIMO handling capability, electronic steerability and inherent ST recursive structure towards enhancing the performance of the existing beamforming techniques and applications.

**Chapter 3** Cognitive radio relies on accurate spectrum sensing for increasing the spectral efficiency of wireless networks. A novel array processing scheme is proposed based on a ULA of circularly-polarized spiral antennas having a frequency range 2-6 GHz, which is used in conjunction with digital beam filters having 2-D IIR transfer functions for accurately and efficiently placing radio sources in a wireless environment. Algorithms, such as cyclostationary feature extraction, are employed at the beamformer to measure energy and realize feature/modulation detection, which, in turn, allows classification of a wireless environment. Simulation examples are provided for demonstrating the low-complexity directional feature detector with applications towards enhancing access to the radio spectrum. Examples showing the

classification of sources by direction, frequency channels and modulation type in the 2-4 GHz band at SNR=6 dB are given.

**Chapter 4** A planar antenna array-based feature detection scheme is proposed to estimate the directional, location and modulation information pertaining to radio sources in a cognitive radio environment. The proposed system employs multiple direction estimation stations and a fusion station. Planar antenna arrays and 3-D IIR digital filters are employed to perform volume scanning of the radio environment, leading to a spatial power profile, which is subjected to peak detection in order to estimate the direction of arrival corresponding to each source. Cyclostationary feature detection is then performed along each direction to estimate the frequency and modulation information. Two simulation examples are provided to verify the feasibility of the proposed approach.

**Chapter 5** An architectural modification to conventional Applebaum adaptive array beamformers is proposed to achieve significant improvements in SINR. Applebaum adaptive arrays optimize the beamformer weights in real time to achieve optimum output SINR. Conventional Applebaum array transfer function is modified by introducing pre-processing digital filters based on 2-D planar-resonant beam filters. The proposed architectural modification introduces complex pole manifolds into the Applebaum array transfer function at guaranteed stability, which in turn leads to better selectivity (i.e. reduced side lobe levels) reflected by SINR improvement. A spatial linear transform of the input 2-D array signal is employed to increase the SINR gain near the broadside direction. Compared to Applebaum adaptive arrays,

the proposed system can provide better than 3 dB (upto 9 dB) additional gain in terms of SINR at the beamformed output at a marginal increase in system complexity of 6 multipliers per antenna for both in-phase (I) and quadrature (Q) channels. For example, 8 dB and 5 dB SINR improvements are reported for desired beam directions of  $(\psi_d)$   $20^\circ$  and  $60^\circ$ ; respectively, where interference is located at  $\psi_d \pm 20^\circ$  (input SIR of -6 dB) for a 64-element uniform linear array.

**Chapter 6** CR depends on the accurate detection of frequency, modulation, and direction pertaining to radio sources, in turn, leading to spatio-temporal directional spectrum sensing. False detections due to high levels of noise and interference may adversely impact the CR's performance. To address this problem, a novel system architecture that increases the accuracy of directional spectrum sensing in situations with low SNR is proposed. This work combines adaptive arrays, multidimensional filter theory and cyclostationary feature detection. A linear array Applebaum beamformer is employed in conjunction with a 2-D planar-resonant beam filter to perform highly directional receive mode wideband beamforming with improved spatial selectivity. A Xilinx Virtex-6 based FPGA prototype of the improved beamforming front-end verifies a clock frequency of 100.9 MHz. The proposed network-resonant Applebaum array provides 6 dB, 5.5 dB and 5 dB noise suppression capability reflected in the spectral correlation function for input SNRs of -20 dB, -25 dB, and -30 dB, respectively, for an RF beam direction  $50^\circ$  degrees from array broadside.

**Chapter 7** Directivity enhancement of rectangular aperture digital STAP beamformer is proposed by employing a 3-D IIR beam filter as a pre-filter to the conventional beamformer. The multiple input multiple output nature of the 3-D IIR beam filter enables the placement of a beam filter in between the antenna array and the STAP beamformer. The proposed 3-D IIR beam filter is realized as a partially separable architecture where a 2-D IIR beamfilter is utilized as the elementary unit. Insertion of the beam filter introduces complex-pole manifolds to the zero-manifold-only array transfer function of the STAP beamformer, which leads to a significant side lobe level reduction. Directivity improvement is determined by analyzing the array factor, the frequency response of the STAP beamformer and the proposed architecture. The proposed architecture shows a better than 6 dB average SIR improvement compared to the conventional beamformer for a less than 0.5% increase in the hardware complexity.

**Chapter 8** The ability to electronically steer a RF beam to “illuminate” a target is fundamental to radar. Transmit beamformers are also needed in wireless communications. Wideband systems, based on direct bits-to-RF apertures, where digital streams are converted to RF using high-bandwidth data converters, that, in turn, drive power amplifiers at each array element, is important for emerging wideband, multi-frequency, multi-waveform applications. An electronically steerable transmit-beamformer based on space-time network-resonant infinite impulse response discrete systems is proposed for wideband directed energy applications. The proposed method leads to an order-of-magnitude lower digital multiplier count compared to the FIR

filter-based transmit arrays. Single-beam architectures are introduced. Simulations demonstrate the space-time domain and 2-D frequency domain behavior of the transmit beamformer for example input signals.

**Chapter 9** RF-FPGAs and field-programmable filter arrays require tunable analog filters that can be digitally reconfigured in real-time to have several user-selected passbands and stopband notches. Such reconfigurable analog filters must operate in the microwave frequencies up to several GHz in order to meet the needs of emerging cognitive radio and reconfigurable radar front-ends. Tunable passive filters based on RF-MEMS, surface acoustic wave- and planar-technologies have been explored in the recent past to achieve this goal. In this chapter, a novel RF-IC approach to design microwave filterbanks having multiple bands, each having independently tunable center frequency and quality factors, is proposed. The proposed technique is based on transfer function synthesis using first-order all-pass filters as building blocks. Using measured data from a current-mode 130-nm CMOS all-pass filter implementation, the feasibility of multi-band, tunable filter arrays is simulated with a tuning range of 4 GHz.

## 10.2 Future Work

Potential future extensions related to the work presented in this thesis, could be highlighted as follows:

1. We could analyze the array factor performance of the 3-D IIR beam filter and the beam enhancement architecture proposed in Chapter 7 through closed form expressions.
2. The 2-D/3-D IIR beam filters that we discussed in this thesis can be realized in hardware architectures, such as “reconfigurable open architecture computing hardware (ROACH)”, along with the aperture arrays and RF front ends to verify the results in Chapter 3 and 4 for directional spectrum sensing and feature detection algorithms.
3. The beam enhancement results that we obtained in Chapters 5, 6 and 7 can be verified using the actual implementation of the proposed architectures in the ROACH platform.
4. The 2-D network resonant transmit beamformer proposed in Chapter 8 could be extended to 3-D space using the theory of 3-D IIR beam filters.
5. The filter coefficients of the bandpass filter proposed in Chapter 9 can be modified to compensate for parasitic low-pass effects. CMOS RF-IC circuit could be designed for the proposed analog SFG.

## BIBLIOGRAPHY

- [1] John Litva and Titus K. Lo. *Digital Beamforming in Wireless Communications*. Artech House, Inc., Norwood, MA, USA, 1st edition, 1996.
- [2] Darren S Goshi, Yuanxun Wang, and Tatsuo Itoh. A compact digital beamforming smart antenna for mobile communications. *IEEE Transactions on Microwave Theory and Techniques*, 52(12):2732–2738, 2004.
- [3] Lal C Godara. Application of antenna arrays to mobile communications. ii. beam-forming and direction-of-arrival considerations. *Proceedings of the IEEE*, 85(8):1195–1245, 1997.
- [4] Salvatore Bellofiore, Constantine A Balanis, Jeffrey Foutz, and Andreas S Spanopoulos. Smart-antenna systems for mobile communication networks. part 1. overview and antenna design. *Antennas and propagation magazine, IEEE*, 44(3):145–154, 2002.
- [5] George V Tsoulos. Smart antennas for mobile communication systems: benefits and challenges. *Electronics & Communication engineering journal*, 11(2):84–94, 1999.
- [6] Isamu Chiba, Ryu Miura, Toyohisa Tanaka, and Yoshio Karasawa. Digital beam forming (dbf) antenna system for mobile communications. *Aerospace and Electronic Systems Magazine, IEEE*, 12(9):31–41, 1997.
- [7] P. Barton. Digital beam forming for radar. *IEE Proceedings of Communications, Radar and Signal Processing*, 127(4):266–277, August 1980.
- [8] G. Krieger, N. Gebert, M. Younis, and A. Moreira. Advanced synthetic aperture radar based on digital beamforming and waveform diversity. In *IEEE Radar Conference, 2008. RADAR '08*, pages 1–6, May 2008.
- [9] B. Cantrell, J. de Graaf, L. Leibowitz, F. Willwerth, G. Meurer, C. Parris, and R. Stapleton. Development of a digital array radar (DAR). In *Proceedings of the 2001 IEEE Radar Conference, 2001*, pages 157–162, 2001.

- [10] Simon Haykin. Cognitive radio: brain-empowered wireless communications. *IEEE Journal on Selected Areas in Communications*, 23(2):201–220, 2005.
- [11] Hüseyin Arslan. *Cognitive radio, software defined radio, and adaptive wireless systems*, volume 10. Springer, 2007.
- [12] Wing Lo and Jue Chang. Digital beamforming in a satellite communication system, January 18 2000. US Patent 6,016,124.
- [13] Thomas Gebauer and Heinz G Gökler. Channel-individual adaptive beamforming for mobile satellite communications. *IEEE Journal on Selected Areas in Communications*, 13(2):439–448, 1995.
- [14] Rafaat Khan, Brian Gamberg, Desmond Power, John Walsh, Barry Dawe, Wayne Pearson, and Dave Millan. Target detection and tracking with a high frequency ground wave radar. *Oceanic Engineering, IEEE Journal of*, 19(4):540–548, 1994.
- [15] Ajay Kr Singh, Pradeep Kumar, Tapas Chakravarty, Ghanshyam Singh, and Sunil Bhooshan. A novel digital beamformer with low angle resolution for vehicle tracking radar. *Progress In Electromagnetics Research*, 66:229–237, 2006.
- [16] Arnold van Ardenne, Bart Smolders, and Grant Hampson. Active adaptive antennas for radio astronomy: results from the r&d program on the square kilometer array. In *Astronomical Telescopes and Instrumentation*, pages 420–433. International Society for Optics and Photonics, 2000.
- [17] Steven W Ellingson, Grant Hampson, et al. A subspace-tracking approach to interference nulling for phased array-based radio telescopes. *IEEE Transactions on Antennas and Propagation*, 50(1):25–30, 2002.
- [18] L. Bruton and N. Bartley. Three-dimensional image processing using the concept of network resonance. *IEEE Transactions on Circuits and Systems*, 32(7):664–672, July 1985.
- [19] H.L.P.A. Madanayake and L.T. Bruton. A speed-optimized systolic array processor architecture for spatio-temporal 2-D IIR broadband beam filters. *IEEE Transactions on Circuits and Systems I: Regular Papers*, 55(7):1953–1966, Aug 2008.
- [20] A. Madanayake and L. Bruton. A fully multiplexed first-order frequency-planar module for fan, beam, and cone plane-wave filters. *IEEE Transactions on Circuits and Systems II: Express Briefs*, 53(8):697–701, Aug 2006.

- [21] C. Wijenayake, A. Madanayake, and L. Bruton. Broadband multiple cone-beam 3-D IIR digital filters applied to planar dense aperture arrays. *IEEE Transactions on Antennas and Propagation*, 60(11):5136–5146, Nov 2012.
- [22] Leslie H Gesell and Richard E Feinleib. True time delay beamforming. Technical report, DTIC Document, 1994.
- [23] M. Tur. True time delay photonic beamforming: A review. In *IEEE International Conference on Microwaves, Communications, Antennas and Electronics Systems, 2009. COMCAS 2009.*, pages 1–2, Nov 2009.
- [24] PS Hall and SJ Vetterlein. Review of radio frequency beamforming techniques for scanned and multiple beam antennas. In *IEE Proceedings H (Microwaves, Antennas and Propagation)*, volume 137, pages 293–303. IET, 1990.
- [25] B.D. Van Veen and K.M. Buckley. Beamforming: a versatile approach to spatial filtering. *ASSP Magazine, IEEE*, 5(2):4–24, April 1988.
- [26] Wei Liu and Stephan Weiss. *Wideband beamforming: concepts and techniques*, volume 17. John Wiley & Sons, 2010.
- [27] Harry L. Van Trees. *Detection, Estimation, and Modulation Theory, Optimum Array Processing*. Number 978-0-471-46383-2. John Wiley & Sons, April 2004.
- [28] A. Madanayake and L. Bruton. A speed-optimized systolic-array processor architecture for spatio-temporal 2D IIR broadband beam filters. *IEEE Transactions on Circuits and Systems-I: Regular Papers*, 55:1953–1966, 2008.
- [29] C. Wijenayake, A. Madanayake, J. Kota, and L. Bruton. Space-time spectral white spaces in cognitive radio: Theory, algorithms, and circuits. *IEEE Journal on Emerging and Selected Topics in Circuits and Systems*, 3(4):640–653, Dec 2013.
- [30] C. Wijenayake, A. Madanayake, L.T. Bruton, and V. Devabhaktuni. Doa-estimation and source-localization in cr-networks using steerable 2-d iir beam filters. In *2013 IEEE International Symposium on Circuits and Systems (IS-CAS)*, pages 65–68, May 2013.
- [31] Dan E. Dudgeon and Russell M. Mersereau. *Multidimensional Digital Signal Processing*. Number 0136049591. Prentice-Hall Signal Processing Series, 1983.

- [32] P. Agathoklis and L. T. Bruton. Practical-BIBO stability of N-dimensional discrete systems. *IEEE Proceedings of Electronic Circuits and Systems*, 130(6):236–242, december 1983.
- [33] A. Madanayake and L. T. Bruton. A Systolic-array Architecture for First-order 3-D IIR Frequency-planar Filters. *IEEE Trans. on Circuits and Systems I: Regular Papers*, 55(6):1546–1559, 2008.
- [34] C. Wijenayake, A. Madanayake, J. Kota, and L. Bruton. Space-time spectral white spaces in cognitive radio: Theory, algorithms, and circuits. *Emerging and Selected Topics in Circuits and Systems, IEEE Journal on*, 3(4):640–653, Dec 2013.
- [35] Final Report, Workshop on Enhancing Access to the Radio Spectrum (EARS), NSF, Arlington, Virginia, Aug. 2010.
- [36] Tevfik Yucek and Huseyin Arslan. A survey of spectrum sensing algorithms for cognitive radio applications. *IEEE Communications Surveys and Tutorials*, 11:116–130, October 2009.
- [37] Ghurumuruhan Ganesan, Ye Li, Benny Bing, and Shaoqian Li. Spatiotemporal sensing in cognitive radio networks. *IEEE Journal on Selected Areas in Communications*, 26(1):5–12, January 2008.
- [38] Matthias Wellens, Janne Riihijarvi, and Petri Mahonen. Spatial statistics and models of spectrum use. *Elsevier Computer Communications*, 32(18):1998–2011, December 2009.
- [39] R.O. Schmidt. Multiple emitter location and signal parameter estimation. *Antennas and Propagation, IEEE Transactions on*, 34(3):276–280, Mar 1986.
- [40] T.S. Dhope and D. Simunic. On the performance of doa estimation algorithms in cognitive radio networks: -a new approach in spectrum sensing. In *Information Communication Technology Electronics Microelectronics (MIPRO), 2013 36th International Convention on*, pages 507–512, May 2013.
- [41] Jingjing Xie, Zhizhong Fu, and Haiying Xian. Spectrum sensing based on estimation of direction of arrival. In *Computational Problem-Solving (ICCP), 2010 International Conference on*, pages 39–42, Dec 2010.

- [42] A. Mahram, M.G. Shayesteh, and S.B. Kordan. A novel wideband spectrum sensing algorithm for cognitive radio networks based on doa estimation model. In *Telecommunications (IST), 2012 Sixth International Symposium on*, pages 359–362, Nov 2012.
- [43] D. Cabric and M. Eric. Spatio-temporal spectrum sensing using distributed antenna systems and direct localization methods. In *Antennas and Propagation Society International Symposium (APSURSI), 2012 IEEE*, pages 1–2, July 2012.
- [44] R. Bawer and J. J. Wolfe. A printed circuit balun for use with spiral antennas. *IRE Trans. on Microw. Theory Tech.*, MTT-8:319325, 1960.
- [45] P. C. Werntz and W. L. Stutzman. Design, analysis and construction of an archimedean spiral antenna and feed structure. in *Proc. IEEE Energy Inf. Technol. Southeast*, 1:308313, 1989.
- [46] C. Wijenayake, A. Madanayake, L. T. Bruton, and V. Devabhaktuni. DOA-estimation and source-localization in CR-networks using steerable 2-D IIR beam filters. In *IEEE International Symposium on Circuits and Systems (ISCAS)*, 2013.
- [47] E. L. D. Costa. Detection and identification of cyclostationary signals. Master’s thesis, 1996.
- [48] C. Wijenayake, A. Madanayake, and L. Bruton. Broadband multiple cone-beam 3-D IIR digital filters applied to planar dense aperture arrays. *IEEE Transactions on Antennas and Propagation*, 60:5136–5146, 2012.
- [49] L. T. Bruton. Three-dimensional cone filter banks. *IEEE Transactions on Circuits and Systems I: Fundamental Theory and Applications*, 50(2):208–216, Feb. 2003.
- [50] S. Applebaum. Adaptive arrays. *IEEE Transactions on Antennas and Propagation*, 24(5):585–598, Sep 1976.
- [51] B. Widrow. A review of adaptive antennas. In *IEEE International Conference on Acoustics, Speech, and Signal Processing*, volume 4, pages 273–278, Apr 1979.
- [52] Hema Singh and Rakesh Mohan Jha. Trends in adaptive array processing. *International Journal of Antennas and Propagation*, vol. 2012:Article ID 361768, 20 pages, 2012.

- [53] Kyu-Man Lee, Dong-Seong Han, and Myeong-Je Cho. Adaptive AGC applebaum array. In *IEEE Military Communications Conference Proceedings, 1999. MILCOM 1999*, volume 1, pages 661–665 vol.1, 1999.
- [54] M.R. Sarker, M.M. Islam, M.T. Alam, and M. Hossam-E-Haider. Side lobe level reduction in antenna array using weighting function. In *2014 International Conference on Electrical Engineering and Information Communication Technology (ICEEICT)*, pages 1–5, April 2014.
- [55] B. Goswami and D. Mandal. Introducing deeper nulls and reduction of side lobe levels in a symmetric linear antenna array using genetic algorithm. In *2012 1st International Conference on Recent Advances in Information Technology (RAIT)*, pages 404–409, March 2012.
- [56] E. Matzner, H.; Levine. Sidelobe reduction in antenna arrays with different element. In *2012 IEEE 27th Convention of Electrical & Electronics Engineers in Israel (IEEEI)*, pages pp.1,3, Nov 2012.
- [57] R. T. Compton. *Adaptive Antennas: Concepts and Performance*. Number 978-0130041517. Prentice Hall, Jan 1988.
- [58] S.V. Hum, H.L.P.A. Madanayake, and L.T. Bruton. Uwb beamforming using 2-d beam digital filters. *IEEE Transactions on Antennas and Propagation*, 57(3):804–807, March 2009.
- [59] A. Madanayake, C. Wijenayake, S. Wijayarathna, R. Acosta, and S.I. Hariharan. 2-D-IIR time-delay-sum linear aperture arrays. *IEEE Antennas and Wireless Propagation Letters*, 13:591–594, 2014.
- [60] J. Mitola and Jr. Maguire, G.Q. Cognitive radio: making software radios more personal. *IEEE Personal Communications*, 6(4):13–18, Aug 1999.
- [61] A. Madanayake, C. Wijenayake, N. Tran, T. Cooklev, S.V. Hum, and L.T. Bruton. Directional spectrum sensing using tunable multi-d space-time discrete filters. In *IEEE International Symposium on a World of Wireless, Mobile and Multimedia Networks (WoWMoM), 2012*, pages 1–6, June 2012.
- [62] T. Yucek and H. Arslan. A survey of spectrum sensing algorithms for cognitive radio applications. *IEEE Communications Surveys Tutorials*, 11(1):116–130, First 2009.
- [63] W. Brown and H.H. Loomis. Digital implementations of spectral correlation analyzers. *IEEE Transactions on Signal Processing*, 41(2):703–720, Feb 1993.

- [64] P. Barton. Digital beam forming for radar. *IEE Proceedings of Communications, Radar and Signal Processing*, 127(4):266–277, August 1980.
- [65] A.B. Smolders and G.W. Kant. Thousand element array (thea). In *IEEE Antennas and Propagation Society International Symposium, 2000.*, volume 1, pages 162–165 vol.1, July 2000.
- [66] Zahed Hossain, Ummy Habiba, and Mohammad Abdul Matin. Efficient beamforming technique for cognitive radio networks. *Journal of Advances in Information Technology*, 4(3):111–115, 2013.
- [67] Longyang Huang, Bin Shen, Mengxing Li, and Zemin Liu. An efficient subband method for wideband adaptive beamforming. In *10th International Conference on Advanced Communication Technology, 2008. ICACT 2008.*, volume 3, pages 1489–1492, Feb 2008.
- [68] C. Fulton and W. Chappell. Low-cost, panelized digital array radar antennas. In *Microwaves, Communications, Antennas and Electronic Systems, 2008. COM-CAS 2008. IEEE International Conference on*, pages 1–10, May 2008.
- [69] Ashok K. Agrawal and E.L. Holzman. Beamformer architectures for active phased-array radar antennas. *Antennas and Propagation, IEEE Transactions on*, 47(3):432–442, Mar 1999.
- [70] S. V. Hum, A. Madanayake, and L. T. Bruton. UWB beamforming using 2D beam digital filters. *IEEE Transactions on Antennas and Propagation*, 55(3):804–807, March 2009.
- [71] C. Wijenayake, A. Madanayake, and L. T. Bruton. Systolic-array architecture for 2d iir wideband dual-beam space-time plane-wave filters. In *53rd IEEE International Midwest Symposium on Circuits and Systems (MWSCAS), 2010*, pages 229–232, Aug 2010.
- [72] J. Becker, F. Henrici, S. Trendelenburg, M. Ortmanns, and Y. Manoli. A field-programmable analog array of 55 digitally tunable OTAs in a hexagonal lattice. *IEEE Journal of Solid-State Circuits*, 43:2759–2768, 2008.
- [73] Radio Frequency-Field Programmable Gate Arrays (RF-FPGA), 2011. under the grant category science and technology DARPA microsystems technology office.
- [74] A. Anand, J. Small, D. Peroulis, and Xiaoguang Liu. Theory and design of octave tunable filters with lumped tuning elements. *IEEE Trans. on Microwave Theory and Techniques*, 61:4353–4364, 2013.

- [75] K. Entesari and G.M. Rebeiz. A differential 4-bit 6.5-10-GHz RF MEMS tunable filter. *IEEE Trans. on Microwave Theory and Techniques*, 53:1103–1110, 2005.
- [76] Hittite Microwave Corporation. *Ultra Compact Tunable MMIC Filters for RF & mWave Systems*, May 2010.
- [77] C. Barth, I.R. Linscott, and U.S. Inan. An image frequency rejection filter for SAW-less GPS receivers. *IEEE Trans on Circuits and Systems I: Regular Papers*, 59:1085–1092, 2012.
- [78] A. Ghaffari, E.A.M. Klumperink, and B. Nauta. Tunable N-path notch filters for blocker suppression: modeling and verification. *IEEE Journal of Solid-State Circuits*, 48:1370–1382, 2013.
- [79] Yixiao Wang, Le Ye, Huailin Liao, and Ru Huang. Cost-efficient CMOS RF tunable bandpass filter with active inductor-less biquads. In *IEEE International Symposium on Circuits and Systems, 2012*, pages 2139–2142, May 2012.
- [80] J.L. Brown and N.M. Neihart. An analytical study of a magnetically tuned matching network. In *IEEE International Symposium on Circuits and Systems*, pages 1979–1982, Seoul, 20-23 May 2012.
- [81] P.A. Regalia, S.K. Mitra, and P.P. Vaidyanathan. The digital all-pass filter: a versatile signal processing building block. *Proceedings of the IEEE*, 76:19–37, 1988.
- [82] P. Ahmadi, M.H. Taghavi, L. Belostotski, and A. Madanayake. 10 GHz current-mode 1st and 2nd-order allpass filters on 130nm CMOS. In *IEEE International Midwest Symposium on Circuits and Systems*, pages 1–4, Columbus, 5-7 August 2013.
- [83] Peyman Ahmadi, M.Hossein Taghavi, Leonid Belostotski, and Arjuna Madanayake. 6-GHz all-pass-filter-based delay-and-sum beamformer in 130nm CMOS. In *IEEE 57th International Midwest Symposium on Circuits and Systems (MWS-CAS), 2014*, pages 837–840, Aug 2014.
- [84] Leonard T. Bruton. *RC-Active Circuits Theory and Design*. Prentice-Hall, Englewood Cliffs, N.J. 07632, 1980, ISBN:0137534671.